

DOCTORAL THESIS

Rational Design of Carbonaceous MOF-based Materials for Chemo- and Electrocatalytic Applications

Kefeng Ping

TALLINNA TEHNIKAÜLIKOOL
TALLINN UNIVERSITY OF TECHNOLOGY
TALLINN 2021

TALLINN UNIVERSITY OF TECHNOLOGY
DOCTORAL THESIS
21/2021

Rational Design of Carbonaceous MOF-based Materials for Chemo- and Electrocatalytic Applications

KEFENG PING



TALLINN UNIVERSITY OF TECHNOLOGY

School of Science

Department of Chemistry and Biotechnology

This dissertation was accepted for the defense of the degree of Doctor of Philosophy in Chemistry on April 13, 2021.

Supervisor

Dr Pavel Starkov
Dept of Chemistry and Biotechnology
Tallinn University of Technology
Tallinn, Estonia

External Examiners

Prof Ahmad Masarwa
Institute of Chemistry
The Hebrew University in Jerusalem
Jerusalem, Israel

Dr Roman Mysyk
Centre for Cooperative Research on Alternative Energies
Basque Research and Technology Alliance
Vitoria-Gasteiz, Spain

Defense of the thesis: May 25, 2021, Tallinn

Declaration:

I confirm that the work presented in this thesis is my own. Where information has been derived from other sources, I confirm that it has been indicated and acknowledged. This thesis has not been submitted for doctoral or equivalent academic degree at any other institution.

Kefeng Ping

Signature



European Union
European Regional
Development Fund



Investing
in your future

Copyright: Kefeng Ping, 2021

ISSN 2585-6898 (publication)

ISBN 978-9949-83-684-0 (publication)

ISSN 2589-6901 (PDF)

ISBN 978-9949-83-685-7 (PDF)

Printed by Koopia Niini & Rauam

TALLINNA TEHNIKAÜLIKOO
DOKTORITÖÖ
21/2021

**Süsinikurikastel, metall–orgaanilistel
võrestikel põhinevate materjalide disain ja
nende kasutuselevõtt kemo- ja
elektrokatalüütilistes rakendustes**

KEFENG PING

Table of contents

List of publications	6
Author contribution	7
Abbreviations	8
Introduction	13
1 M–N–C catalyst materials	14
1.1 Preparation of catalysts	16
1.2 Characterization of catalysts	19
1.3 Outlook and conclusions	21
1.4 Aims and objectives	21
2 Hybrid ligands for metal–organic frameworks-derived bifunctional oxygen electrocatalysts and heterogenous oxidation reactions	22
3 Multifunctional catalyst material from an amorphous cobalt metal–organic framework	29
4 Shungite as a carbon support for bifunctional oxygen electrocatalysts	34
5 Experimental section	37
Conclusions	52
References	53
Acknowledgements	65
Abstract	66
Lühikokkuvõte	68
Appendix	71
Publication I	71
Publication II	79
Publication III	87
Publication IV	97
Publication V	101
Curriculum vitae	113
Elulookirjeldus	115

List of publications

- I **Ping, K.**; Brashinsky, A.; Alam, M.; Bhadoria, R.; Mihkli, V.; Mere, A.; Vlassov, S.; Kook, M.; Rähn, M.; Sammelseg, V.; Aruväli, J.; Tammeveski, K.; Kongi, N.; Starkov, P.
Fused hybrid linkers for metal–organic framework-derived bifunctional oxygen electrocatalysts.
ACS Appl. Energy Mater. **2020**, *3*, 152–157.
[DOI:10.1021/acsaem.9b02039](https://doi.org/10.1021/acsaem.9b02039)
- II **Ping, K.**; Alam, M.; Käärik, M.; Leis, J.; Kongi, N.; Järving, I.; Starkov, P.
Surveying iron–organic framework TAL–1-derived materials in ligandless heterogeneous oxidative catalytic transformations of alkylarenes.
Synlett **2019**, *30*, 1536–1540.
[DOI:10.1055/s-0037-1611877](https://doi.org/10.1055/s-0037-1611877)
- III **Ping, K.**; Alam, M.; Kahnert, S. R.; Bhadoria, R.; Mere, A.; Mikli, V.; Käärik, M.; Aruväli, J.; Paiste, P.; Kikas, A.; Kisand, V.; Järving, I.; Leis, J.; Tammeveski, K.; Kongi, N.; Starkov, P.
Multi-purpose chemo- and electrocatalyst material from an amorphous cobalt metal–organic framework.
Manuscript submitted.
- IV Kongi, N.; Tammeveski, K.; Starkov, P.; **Ping, K.**
Novel catalyst materials.
PCT Appl. PCT/EP2019/072050
<https://patentscope.wipo.int/search/en/detail.jsf?docId=WO2020035607>
- V Kazimova, N.; **Ping, K.**; Danilson, M.; Merisalu, M.; Aruväli, J.; Käärik, M.; Mikli, V.; Leis, J.; Tammeveski, K.; Starkov, P.; Kongi, N.
Shungite-derived graphene as a carbon support for bifunctional oxygen electrocatalysts.
J. Catal. **2021**, *395*, 178–187.
[DOI:10.1016/j.jcat.2021.01.004](https://doi.org/10.1016/j.jcat.2021.01.004)

Author contribution

- I Prepared and characterized the ligands and the MOF derived materials; writing the manuscript and the SI
- II Prepared and characterized the organic compounds; writing the manuscript and the SI
- III Prepared and characterized the organic compounds; assembled the zinc–air battery; writing the manuscript and the SI
- IV Prepared and characterized the ligands and MOF derived materials; performed stability tests; writing the PCT application
- V Prepared and characterized the catalyst materials; writing the manuscript and the SI

CRedit author statement

Conceptualization, methodology, validation, formal analysis, investigation, writing – original draft, writing – review and editing, visualization.

Abbreviations

AC	activated carbon
Ac	acetate
Ar	aryl
BET	Brunauer–Emmett–Teller method
BINAP	2,2'-bis(diphenylphosphino)-1,1'-binaphthalene
CNT	carbon nanotube
CO ₂ RR	carbondioxide reduction reaction
COF	covalent organic framework
CV	cyclic voltammetry
DABCO	1,4-diazabicyclo[2.2.2]octane
DCDA	dicyandiamide
DCM	dichloromethane
DMF	dimethylformamide
DMSO	dimethyl sulfoxide
equiv	equivalent
EDX	energy-dispersive X-ray spectroscopy
EELS	electron energy loss spectroscopy
EXAFS	extended X-ray absorption fine structure
EtOH	ethanol
FC	fuel cell
FTIR	Fourier-transform infrared spectroscopy
GC	glassy carbon
GDL	gas diffusion layers
GO	graphene oxide
h	hour
HAADF	high-angle annular dark-field
HER	hydrogen evolution reaction
HHTP	hexahydroxytriphenylene
HITP	hexaiminotriphenylene
HMT–PMBI	hexamethyl-p-terphenyl poly(benzimidazolium)
HPLC	high-performance liquid chromatography
HRMS	high resolution mass spectrometry
HRSEM	high-resolution scanning electron microscopy
HRTEM	high-resolution transmission electron microscopy
ICP–AES	inductively coupled plasma atomic emission spectroscopy
ICP–MS	inductively coupled plasma mass spectrometry
ICP–OES	inductively coupled plasma optical emission spectroscopy
K–L	Koutecky–Levich
LSV	linear sweep voltammetry
MAB	metal–air battery

Me	methyl
mel	melamine
2-mim	2-methylimidazole
M–N–C	metal, nitrogen-doped carbon
M–N _x	nitrogen coordinated metal center
MOF	metal organic framework
MP–AES	microwave plasma–atomic emission spectrometer
NMR	nuclear magnetic resonance
NP	nanoparticle
NRR	nitrogen reduction reaction
OER	oxygen evolution reaction
ORR	oxygen reduction reaction
Pd/C	palladium on carbon
PE	petrol ether
PGM	platinum group metals
PTFE	polytetrafluoroethylene
PVA	poly(vinyl alcohol)
PVP	polyvinylpyrrolidone
PXRD	powder X-ray diffraction
Py	pyridinyl
RDE	rotating disk electrode
ref	reference
rGO	reduced graphene oxide
RT	room temperature
SAC	single atom catalyst
SEM	scanning electron microscopy
SI	supporting information
STEM	scanning transmission electron microscopy
TBHP	<i>tert</i> -butyl hydroperoxide
TCA	trichloroacetic acid
TEA	triethylamine
TEM	transmission electron microscopy
TFA	trifluoroacetic acid
THF	tetrahydrofuran
UV	ultraviolet
vs	versus
XANES	X-ray absorption near edge structure
XAS	X-ray absorption spectroscopy
XPS	X-ray photoelectron spectroscopy

绳锯木断，水滴石穿

Perseverance will prevail

Introduction

Development of universal catalyst materials is the cornerstone of sustainable technologies. The lock-and-key relationship between one specific catalyst and one specific process is widely relied upon; however, well-optimized heterogeneous catalysts can eventually be used for various applications. The purpose of my PhD work was to develop a series of novel iron and cobalt-based materials derived from polycrystalline and amorphous metal-organic frameworks, respectively, and applied these materials as universal catalysts (i) in organic transformations, namely, oxidation and benzylic homocoupling reactions; and (ii) in various electrocatalytic reactions that are directly linked to energy conversion and storage devices, specifically, oxygen reduction reaction (ORR), oxygen evolution reaction (OER), and hydrogen evolution reaction (HER).

Chapter 1 gives a concise overview on preparation and characterization of novel M–N–C materials. Chapter 2 (Publications I, II, and IV) describes fabrication and applications of novel iron-based materials derived from a set of 5,6-substituted benzimidazoles in ORR, OER and oxidative transformations of alkylarenes. In Chapter 3 (Publications III and IV), the best preforming ligand was used to prepare a series of cobalt based materials, which were then used to identify an optimal one that can simultaneously be used both as chemo- and electrocatalyst. In Chapter 4 (Publication V), shungite, a carbon-rich raw material is introduced as a new carbon support. Chapter 5 includes experimental details.

1 M–N–C catalyst materials

In this Chapter, I give a concise **overview** of the fabrication, morphological and physical characterization techniques in relation to M–N–C (metal, nitrogen-doped carbon) materials, which is a hot topic in heterogeneous and electrocatalysis [1].

In the **heterogeneous catalysis** domain, most of the organic transformations comprise of reduction and oxidation reactions, which may often be coupled to a secondary process such as amination, condensation, or esterification (Table 1) [2–20]. Most of the work reported to date has focused on the use of iron and cobalt-based materials.

In the **electrocatalysis** domain, M–N–C catalysts are the cornerstone of the next-generation clean energy storage and conversion devices, including rechargeable metal–air batteries (MABs), fuel cells (FCs), and electrolyzers (Fig. 1) [21]. The most fundamental electrocatalytical interconversions are oxygen reduction reaction (ORR) [22], oxygen evolution reaction (OER) [23], hydrogen evolution reaction (HER) [24], nitrogen reduction reaction (NRR) [25] and carbondioxide reduction reaction (CO₂RR) [26].

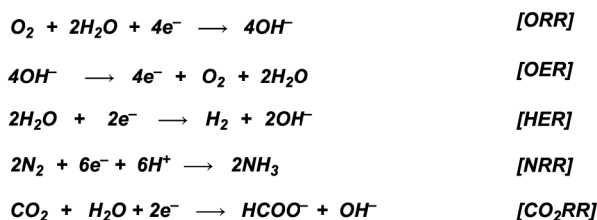
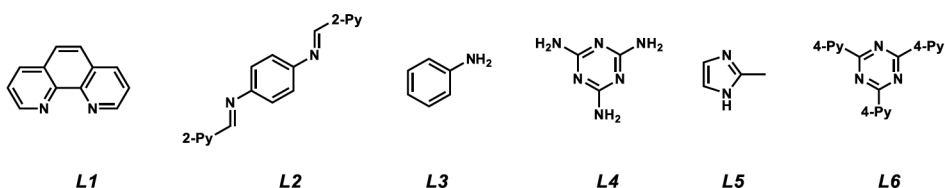


Figure 1. Electrochemical processes with M–N–C materials.

While in organometallic and especially, in organocatalysis, a number of ligands have been designated as the ‘privileged ligands’ such as BINAP and cinchona alkaloids [27], it would be beneficial to establish a similar concept for the multifunctional catalysts used in heterogeneous and electrocatalysis.

Table 1. Applications of *M–N–C* materials in heterogeneous catalysis.



entry	ligand	support	reaction	substrate	reagent	ref
iron based catalysts						
1	L1	Vulcan XC72R	reduction	nitroarene	H ₂	[2]
2	L2	Vulcan XC72R	hydrogenation	(iso)quinolone	H ₂	[3]
3	L1	activated carbon	hydrogenation	furfural	^t BuOH	[4]
4	L1	Vulcan XC72R	dehydrogenation	<i>N</i> -heterocycle	air	[5]
5	L1	Vulcan XC72R	dehydrogenation	benzylamine	O ₂	[6]
6	L1	MgO	oxidation	ethylbenzene	TBHP	[7]
7	–	bamboo	oxidative rearrangement	<i>trans</i> -stilbene	TBHP	[8]
cobalt based catalysts						
8	L1	Vulcan XC72R	reduction	nitroarene	H ₂	[9]
9	L1	Mg(OH) ₂	reductive coupling to azo compounds	nitroarene	H ₂	[10]
10	L2	SiO ₂	reductive amination	nitroarene with benzaldehyde	HCOOH	[11]
11	L3	SiO ₂	reductive alkylation	quinoline with benzaldehyde	HCOOH	[12]
12	L1	Al ₂ O ₃	hydrogenation	quinoline	H ₂	[13]
13	L4	TiO ₂	hydrogenation	pyridine	H ₂	[14]
14	L1	SiO ₂	hydrogenation	alkyne	H ₂	[15]
15	L1	LUDOX®	oxidative esterification + bond cleavage	alcohol	O ₂	[16]
16	ZIF-67 [using L5]		oxidative esterification	ArCH ₂ OH	air	[17]
17	ZIF-67 [using L5]		oxidation	benzyl alcohol	air	[18]
18	ZIF-67 [using L5]		oxidation	alkylarene, alkene	TBHP, O ₂	[19]
19	L6	–	oxidative amidation	ArCHO	TBHP	[20]

1.1 Preparation of catalysts

There are two main strategies to fabricate M–N–C catalysts [22, 28]. One of them is based on combining various supports, metal salts and heteroatom dopants. Another one relies on using nitrogen-rich metal–organic or metal-doped covalent organic frameworks (MOFs and COFs, respectively). However, **carbonization** by heat treatment in the 400–1000 °C range, is always required to increase the carbon content and generate the active species. Typically, this leads to the formation of metal nanoparticles (NPs) and metal-free and/or metal-coordinated sites. The latter are often referred to as single atom catalysts (SACs) [29, 30]. In the more complexed, bimetallic systems, additional catalytically active sites are ligated bimetallic sites [31] as well as metal alloy nanoparticles [32]. These species may contribute to the overall enhanced catalytic properties of the underlying materials either independently or synergistically.

In case one prefers to use a **combination** of various precursors (metal salts, supports, dopants) to generate the M–N–C materials, a greater consideration should be given to the role that each of the components plays, including their ratios. For example, there is a multitude of **carbon supports**, onto which the catalytically active sites can be installed [33]. These include carbon nanotubes (CNTs), activated carbon, Vulcan XC72R, graphene, graphene oxide (GO), reduced graphene oxide (rGO), MXenes [34], and polymers such as polyvinylpyrrolidone (PVP) [35]. Additionally, nature, biomass and waste-derived sources of carbon can be used such as shungite [36], bird droppings [37], wood [38], chicken manure [39], bamboo [40], cabbage [41], and beetroot [42]. However, these precursors also have traces of heteroatoms and metals, which may contribute to the overall activity. In heterogeneous catalysis, often, non-carbon, **Lewis acidic supports** are employed such as Al_2O_3 [43], TiO_2 [44], Nb_2O_5 [45] and ZrO_2 [46]. Other supports, specifically, $\text{Mg}(\text{OH})_2$ [47], MgO [48], SiO_2 [49], and NaCl [35] are employed as **sacrificial supports**, which can later be removed by acid or base etching.

Crystalline porous materials, predominantly, metal–organic frameworks (MOFs) but also covalent organic frameworks (COFs), are gaining recognition as promising carbon templates [50, 51, 52]. Since they are crystalline and have a precise topology, they give rise to carbonized materials that are highly ordered and highly porous; hence, they have large surface area. Typically, MOFs and metal-modified COFs have metals and heteroatoms already present in their frameworks, so no additional doping is required. In several instances, metal exchange can be utilized as a strategy to introduce various transitional metals in place of the existing ones, while maintaining the topology of the original MOF, e.g. by using zinc-based ZIF–8 as a precursor [53].

Doping with metals is typically done by pre-mixing the supports with metal salts or other metal containing compounds prior to the carbonization step by using ball milling, sonication, hydrothermal or thermal treatments. The organometallic compounds used as co-dopants include metal porphyrins [54], metal phthalocyanines [55] or other pre-formed metal complexes, for instance, with 1,10-phenanthroline [10].

In most cases, carbonization is carried out under inert gases (i.e. dinitrogen or argon). However, dihydrogen or ammonia, which at higher temperatures decompose to give dihydrogen, are often utilized to modify the atmosphere [56]. This leads to an improved reduction of metal salts and oxides to give metal nanoparticles. The use of dioxygen, on the other hand, leads to the formation of metal oxides and/or partially oxidized carbon support, which improves overall conductivity and activity of the material.

Heteroatom doping is an essential modification of M–N–C materials because it is crucial for the formation of catalytic sites at the surface of the carbon to which the metal can coordinate (Table 2). In addition to metal(0), metal oxide and metal carbide NPs, the use of heteroatoms can also lead to the formation of other metal species such as metal nitrides, sulfides, and phosphides. Finally, in some cases heteroatom sites may on their own act as catalysts without a necessity for a metal.

The nitrogen-ligated metal species (M–N_x, where x = 3–5) are the most widely studied ones. However, metal species coordinated to several different heteroatoms have been also reported. As doping with nitrogen is the most prevalent and the most important contributor to the overall activity of M–N–C materials, a larger number of different nitrogen sources has been investigated (Table 2 and Fig. 2). When MOFs are used as precursors, nitrogen doping is not necessary because MOFs themselves have a high nitrogen content.

Table 2. Examples of heteroatom doping.

<i>heteroatom</i>	<i>heteroatom source</i>
boron	B(OH) ₃ [57] B ₂ O ₃ [58]
phosphorous	phytic acid [59, 60] hexachlorocyclophosphazene [61] H ₃ PO ₄ [62] NaH ₂ PO ₂ [63]
sulfur	KSCN [64] sulfur [65] thiourea [66]
nitrogen	DCDA [67] melamine [67] DABCO [67] urea [67] thiourea [67] and the metal complexes (Fig. 2)
oxygen	H ₂ O ₂ [68] air [60]
fluorine	NH ₄ F [70, 71, 72] PTFE [73]

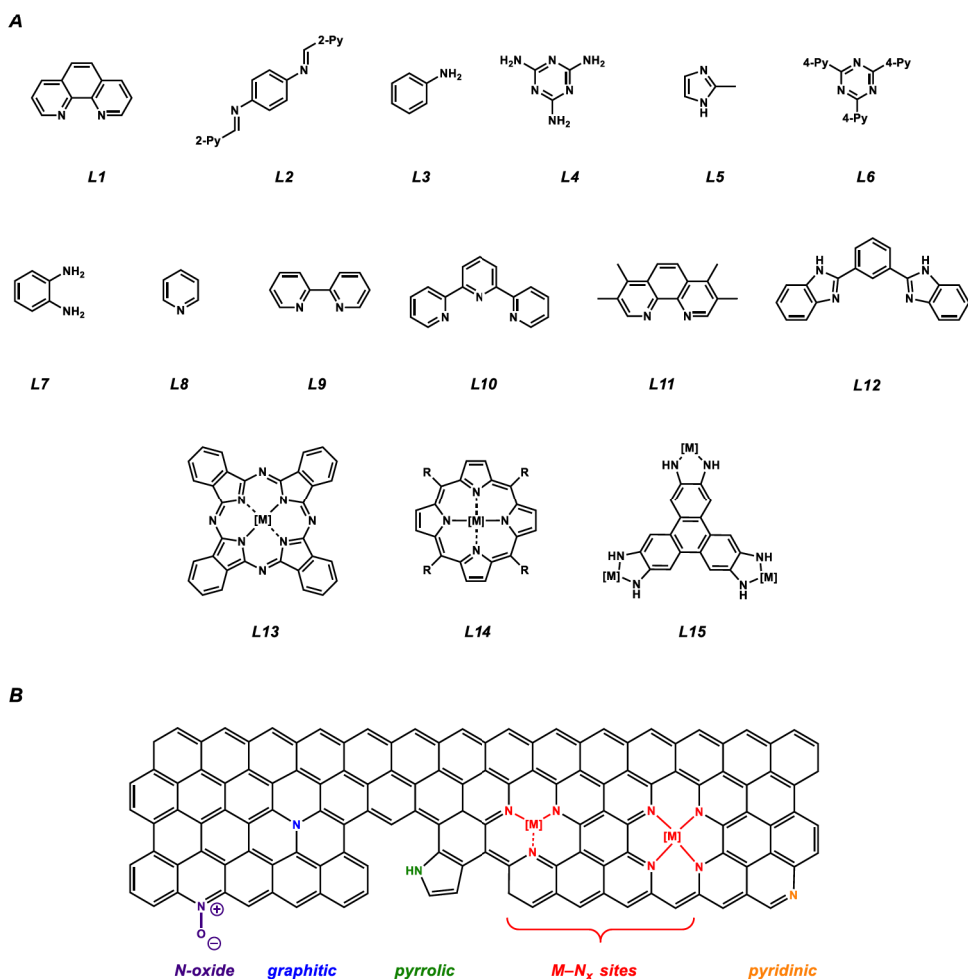


Figure 2. (A) Widely used nitrogen containing ligands for M–N–C catalysts. (B) Different nitrogen catalytic sites. Adapted with changes from ref [74].

Chemical etching is performed with acids such as HCl, HNO₃, H₂SO₄ or combination thereof to remove metal oxides adsorbed onto the catalyst material surface or supports that have been used as templates. Sometimes base (e.g. NaOH) can be used to remove silicon-based sacrificial supports. While materials used in electrochemical transformations are always chemically etched, the materials used for heterogeneous catalysis are generally not etched. This, however, creates a misperception about the nature of catalytically active sites (e.g. nitrogen coordinated metal sites within the molecular network M–N_x) and species (e.g. metal or metal oxide nanoparticles). Often, chemically etched samples are subject to an additional carbonization step to remove nitro and sulfonyl groups, which may be formed during acid treatment.

In the long term, there is a need for the fabrication methods that are more well-thought-out so that to be able to control and finetune the properties of the underlying catalyst materials. This is indeed needed because there is a myriad of factors that go on to contribute to the overall catalyst properties, including stability, activity, and importantly, the reproducibility.

1.2 Characterization of catalysts

Various metal nanoparticles and M–N_x sites are the most commonly acknowledged active species. The nature of the underlying catalyst and its catalytic sites material may change drastically when different metal and nitrogen sources and supports are being used as precursors. The same is valid for carbonization at different temperatures and etching conditions. Thorough characterization of active and spent catalysts provides a better understanding into the origin of catalytic activity of the specific sites. Unfortunately, the acid etching step is often omitted for the M–N–C materials used in heterogeneous catalysis. Surely, this raises some questions about the composition of the material itself including the identity of the active species involved.

By merging the datasets obtained from several characterization techniques, one may get a better insight into the composition as well as the morphological and physical makeup of both the active and spent catalysts. This information may help understand the catalytic processes at hand and the ways how to improve catalyst's performance. These methods also give an opportunity to study spent catalysts by knowing how the catalyst is being deactivated by using a combination of experimental and computational analyses. Various analytical methods used in materials science are briefly summarized below.

Powder X-ray diffraction (PXRD) is a cost-effective method to study the composition of the material including the degree of crystallinity. It relies on a crystalline structure causing a beam of incident X-rays to diffract into many specific directions. In the study of heterogeneous catalysts, one can decipher the presence of various metallic nanoparticles. The main limitation of this technique is its poor sensitivity when the concentration of a given species is low.

X-ray photoelectron spectroscopy (XPS) is used to study elemental composition of materials at the surface both qualitatively and quantitatively. XPS provides with the chemical and electronic states of the elements, e.g. M–N_x sites and different nitrogen species (Fig. 2b). XPS can be used to monitor the formation of active sites at the surface of precursors, active and spent catalysts.

Mössbauer spectroscopy is based on Mössbauer effect, which consists of nearly recoil-free emission and absorption of nuclear gamma rays in solids. It is widely used to discriminate between different iron species and requires a relatively large sample amount.

Scanning electron microscope (SEM) is used to study the morphology and elemental composition of the material. However, it is not quantitative in the latter case because the information is obtained only from the surface of a material.

Transmission electron microscopy (TEM) is a method that uses a beam of electrons transmitting through a sample. It can be utilized at any stage of material fabrication while continuously providing insight into the structure of the catalyst. However, it cannot be used to detect the presence of single atom catalysts (SACs).

Energy-dispersive X-ray spectroscopy (EDX) is used to study, identify, map, and quantify elemental composition of surfaces or samples when combined with SEM or TEM, respectively.

Electron energy loss spectroscopy (EELS) is complementary to EDX. EELS is capable of characterizing materials containing relatively low atomic number elements (C, N, and occasionally O) in terms of their atomic composition, chemical bonding, valence and conduction band electronic properties, surface properties, and element-specific pair distance distribution.

High-angle annular dark-field scanning transmission electron microscopy (HAADF-STEM) is often used when TEM is not able to detect any visible particles, which is the case for SACs. Different single metal atoms can be detected.

Raman spectroscopy is used to observe how carbon structure defects affect the activity of a material. It is generally used to determine the ratio between D and G bands, where the G band is a result of the in-plane vibrations of sp^2 carbons and the D band is due to the out-of-plane vibrations attributed to the presence of structural defects. Additionally, certain metal species can also be characterized by this method.

Brunauer-Emmett-Teller (BET) is used to study gas uptake, surface area and pore sizes of a material. Both active and spent catalysts can be examined by this method to make sure that no changes occurred during catalytic transformations.

X-ray absorption near edge structure/extended X-ray absorption fine structure (XANES/EXAFS). XAFS (X-ray absorption fine structure) measurements are of importance not only in demonstrating atomic dispersion of metal atoms but also in giving a more detailed information on different oxidation states, coordination numbers and configurations of SACs, and is the most powerful technique to get insight into the structural information of SACs. The X-ray absorption spectrum can be divided into X-ray absorption near-edge spectroscopy (XANES) and extended X-ray absorption fine structure (EXAFS) spectroscopy. XANES mainly reflects the valence state and some structural information on the absorbing atom. EXAFS is strongly sensitive to the coordination environment of the absorbing atom. As metal-metal bonds of a same metal are not observed in EXAFS spectra, it is an efficient method to detect both single and bimetallic SACs.

Inductively coupled plasma/microwave plasma-mass spectrometry/optical emission spectroscopy/atomic emission spectroscopy (ICP-MS, ICP-OES, ICP-AES, MP-AES) are used to quantify metal composition within a given sample. These methods are also used to monitor metal leaching.

The contribution of different active species (nanoparticles vs. M-N_x sites) is often studied by selective **chemical deactivation** by using chemical reagents. For instance, Fe-N_x and Co-N_x sites can be deactivated using sodium nitrite [75] and potassium thiocyanate [76], respectively. Chlorine gas was used to deactivate iron carbide nanoparticles, which were then reactivated by treatment with dihydrogen [77].

All of these techniques can also be applied to characterize spent catalysts to understand how and why active catalysts lose their activity, for example, metal leaching from M-N_x sites (e.g. MP-AES), decomposition of nanoparticles (TEM, XRD), which may be associated with changes in porosity and pore sizes (BET), oxidation of carbon network (XPS, TEM), etc.

1.3 Outlook and conclusions

M–N–C materials, which are based on non-precious metals (Fe, Ni, Co, Mn, Cu), are gaining popularity in both heterogeneous and electrocatalysis. Their fabrication strategies are quite similar, albeit acid etching is omitted in the former case. To date, the choice of ligands has remained rather limited, and relied on the use of 1,10-phenanthroline, porphyrins, phthalocyanines and well-established MOFs (ZIF-8 and ZIF-67). In the future, it might be more insightful to explore a wider range of ligands and metal combinations to improve the stability and performance profiles of the final catalysts. This will also be essential for getting more sophisticated computational models and will eventually result in the uptake of M–N–C materials for the use in large scale applications. This, however, will require a deeper understanding of deactivation mechanisms of the catalysts in-hand so as to reduce their loadings, obtain their environmental toxicity profiles and ensure their sustainability in the long term.

1.4 Aims and objectives

The aim of this study was to develop versatile, carbon-rich MOF-derived materials for their simultaneous use in heterogeneous and electrocatalysis applications. Specifically, to

- [1] design cost-effective carbonaceous ligands (**TL1–TL9**) to replace non-modular systems based on HHTP, HITP, porphyrin, phthalocyanine, 2-methylimidazole (Fig. 3);
- [2] test them as electrocatalysts in oxygen reduction and oxygen evolution reactions;
- [3] explore their use including the recyclability in organic transformations such as oxidation and benzylic homocoupling reactions.

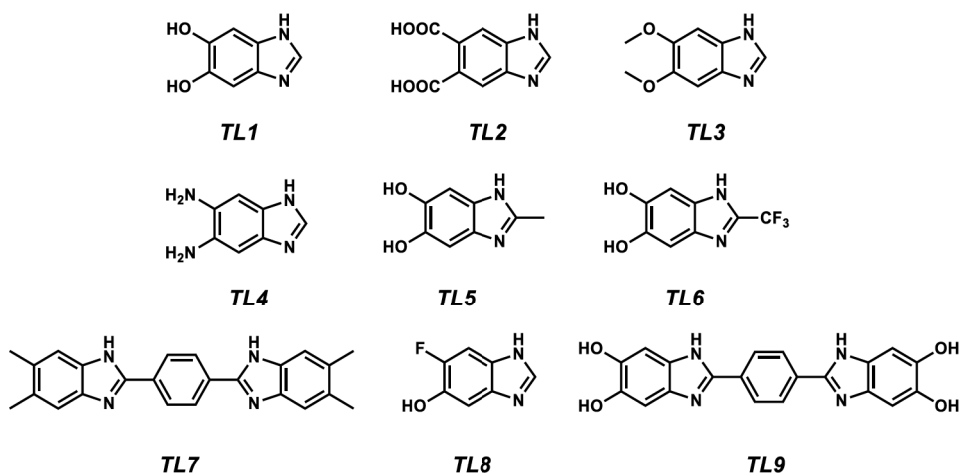


Figure 3. Ligands screened for the linker effects.

2 Hybrid ligands for metal–organic frameworks-derived bifunctional oxygen electrocatalysts and heterogenous oxidation reactions

This Chapter is based on the work published in Publication I [78] and Publication II [74].

Only a very small panel of organic ligands as precursors for MOF-derived bifunctional catalysts has been reported to date (Fig. 4a) [79–85]. We wished to explore whether the use of various carbonaceous [86] organic linkers may lead to variations in the performance of M–N–C materials. This work was based on the preliminary data obtained in the Starkov group, where different substituents in C-2 position of 1*H*-benzo[*d*]imidazole-5,6-diol were examined [87]. My primary focus was on the identification of effects caused by alterations at positions C-5 and C-6 of the parent benzimidazole (Fig. 4b). These results were published as a communication [78].

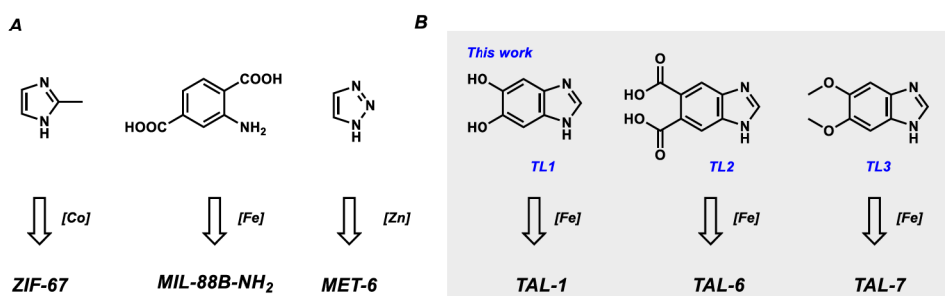


Figure 4. Organic precursors for metal–organic frameworks used (A) previously and (B) in this work. Adapted with changes from ref [78].

Three *polycrystalline* MOFs (TAL–1, TAL–6 and TAL–7) were prepared from iron chloride and 5,6-disubstituted-1*H*-benzo[*d*]imidazoles (TL1, R = OH; TL2, R = COOH; TL3, R = OCH₃) (Fig. 4). Upon carbonization at 900 °C, acid etching and recarbonization, three electrocatalyst materials referred to as TAL–1–900, TAL–6–900 and TAL–7–900 were obtained.

The HRTEM images of TAL–1–900 and TAL–7–900 indicated the presence of α -Fe/Fe₃C nanocrystals, surrounded by the graphitic layers (Fig. 5b), with a lattice distance of 0.203 nm and 0.371 nm, respectively [88, 89–92]. These nanoparticles were also confirmed by PXRD (Fig. 5c). TAL–6–900, however, incorporated iron oxide nanoparticles with a characteristic interplanar spacing of 0.29 nm corresponding to *d* (220) of Fe₃O₄ [93]. The XPS data was consistent with elemental composition (Fig. 5d and S1 and Table S2 in ref [78]) showing rather low levels of iron present at the surface of all of the materials (<0.41 at%). This was also in line with the data obtained from MP–AES (Table S1 in ref [78]; <3.6 wt%).

The electrochemical behavior of TAL–1–900, TAL–6–900 and TAL–7–900 was assessed by using cyclic voltammetry (CV) in 0.1 M KOH solution at RT (Fig. 6a). The catalyst loadings used in this work were 800 $\mu\text{g cm}^{-2}$ for TAL-derived materials (loading dependences are shown in Fig. S6c in ref [78]). The TAL electrocatalysts exhibited a symmetrical and rectangular CV profile without any characteristic redox features. The double-layer capacitance was larger than that of Pt/C, indicating that TAL–derived materials have high electrochemically accessible surface area.

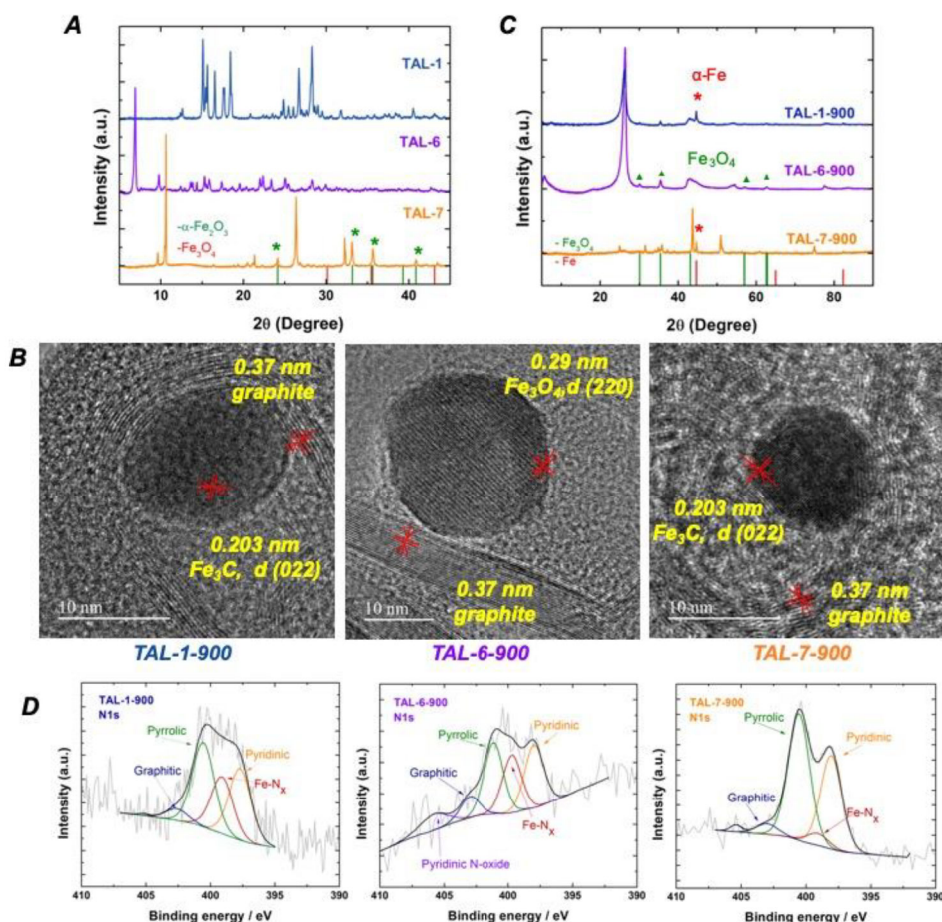


Figure 5. Physical and morphological characterization of TAL-X-900 precursors and derived catalyst materials. (A) PXRD patterns of TAL precursors. (B) HRTEM micrographs. (C) PXRD patterns of TAL-derived catalyst materials. (D) XPS core-level spectra in the N1s region. Scale bars, 10 nm. Adapted from ref [78].

The rotating disk electrode (RDE) technique was employed to study the ORR kinetics of TAL-modified glassy carbon (GC) electrodes in O₂-saturated 0.1 M KOH (Fig. 6b). TAL-1-900 (R = OH) performed on par with 20 wt% Pt/C catalyst ($E_{on} = 1.01$ V, $E_{1/2} = 0.87$ V vs. $E_{on} = 1.01$ V, $E_{1/2} = 0.85$ V). TAL-6-900 was less active, while electrocatalyst TAL-7-900 still showed reasonable performance. The number of electrons transferred per O₂ molecule (n) was four (inset in Fig. 6c and S11 in ref [78]) for all the catalyst materials suggesting that O₂ was fully reduced to water in a stepwise process ($2e \times 2e$). Stability for TAL-1-900 was determined by continuous cycling from 0.6 to 1.0 V vs. RHE ($\Delta E_{1/2} = 6.1$ mV, Fig. 6f).

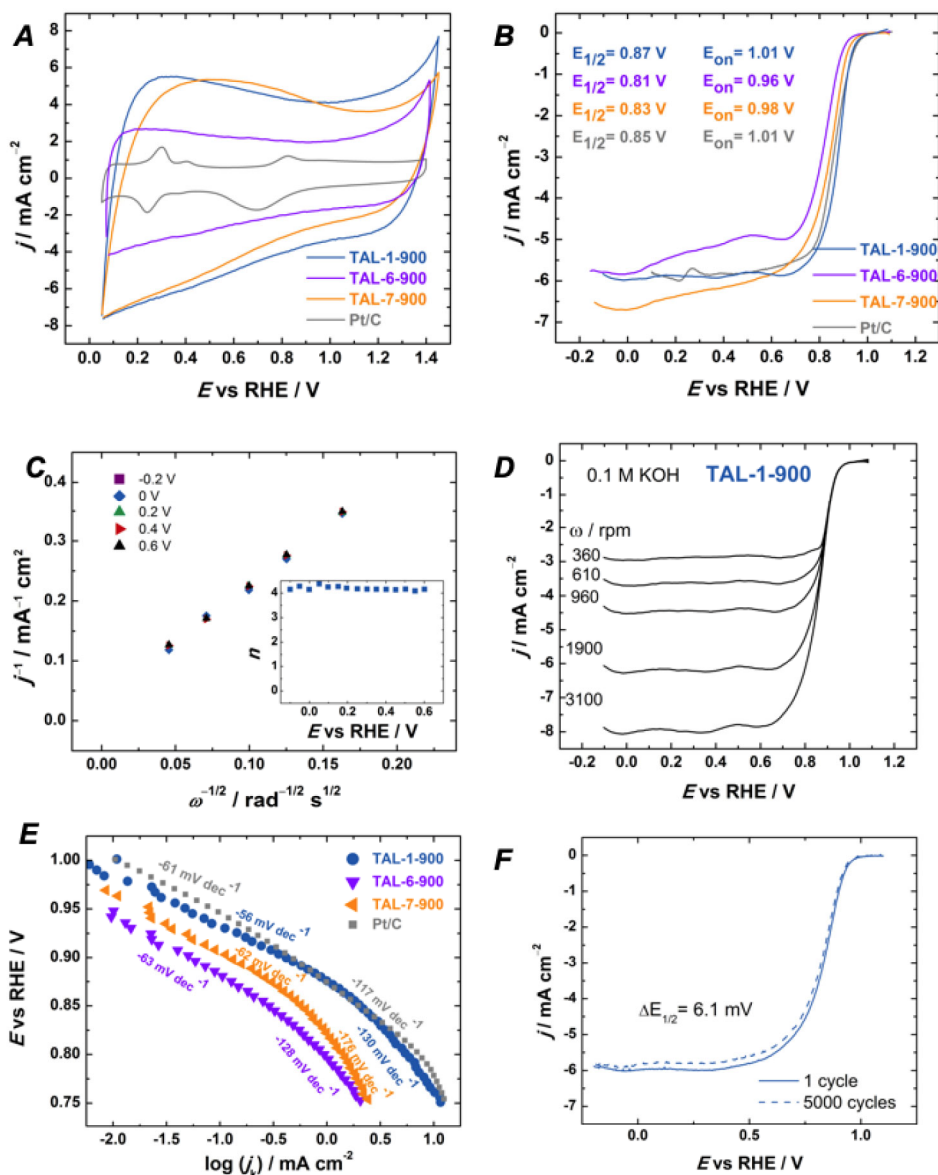


Figure 6. Electrochemical oxygen reduction on TAL materials in 0.1 M KOH. (A) Cyclic voltammograms of electrocatalyst-modified GC electrodes (under argon); $v = 50 \text{ mV s}^{-1}$. (B) RDE polarization curves for TAL and Pt/C modified GC electrodes at 1900 rpm; $v = 10 \text{ mV s}^{-1}$. (C) Koutecký–Levich plots for O_2 reduction on TAL-1-900 modified GC electrode, inset: number of electrons transferred per O_2 molecule. (D) RDE polarization data on oxygen reduction recorded at various rotation rates on TAL-1-900 modified GC electrode; $v = 10 \text{ mV s}^{-1}$. (E) Tafel plots for O_2 reduction on TAL and Pt/C catalysts. (F) Electrochemical stability test for TAL-1-900 (mid-range: 0.6–1.0 V). Adapted from ref [78].

The TAL materials were also tested in oxygen evolution reaction (Fig. 7). It is well known that the materials that are highly active in both ORR and OER are useful for applications in rechargeable metal–air batteries [97]. The standard way to assess such bifunctional activity is to calculate the potential differences (ΔE) of OER at a current density of 10 mA cm^{-2} and of ORR at a current density of -3 mA cm^{-2} at electrode rotation rate of 1600 rpm. The bifunctional activity of TAL–1–900 ($\Delta E = 0.73 \text{ V}$; $E_{10} = 1.60 \text{ V @ } 10 \text{ mA cm}^{-2}$) was one of the best performing ones (*cf.*, Table S7 in ref [78]). Stability of TAL–1–900 was evaluated using chronoamperometry (Fig. 7c) and continuous cycling of TAL–1–900 between 1.0 and 1.8 V vs. RHE (Fig. 7d).

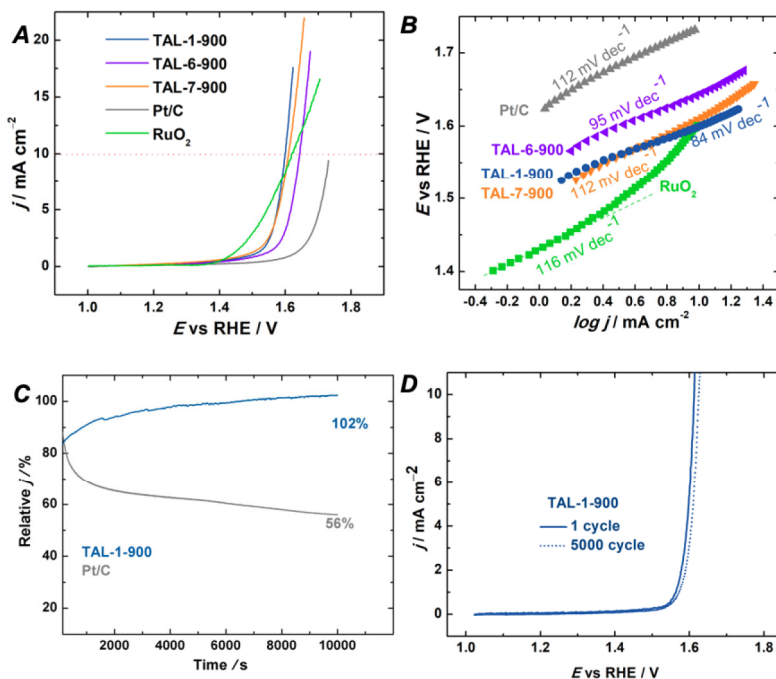
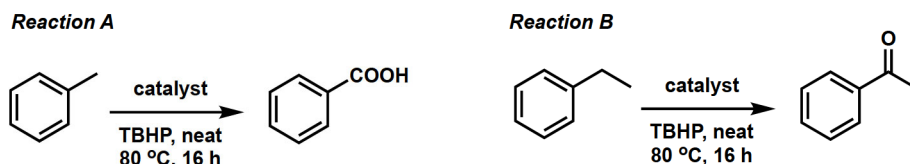


Figure 7. Electrochemical oxygen evolution on TAL materials in 0.1 M KOH. (A) LSV curves for TAL-modified GC electrodes, $v = 10 \text{ mV s}^{-1}$. (B) Tafel plots based on LSV curves. (C) Chronoamperometric response for TAL–1–900 and Pt/C recorded at applied potential of 1.6 V. (D) Electrochemical stability of TAL–1–900 after 5000 cycles. Adapted from ref [78].

The performance among the TAL-derived materials (TAL–1–900 > TAL–7–900 >> TAL–6–900) suggests that electron-rich precursors may boost the ORR/OER catalyst's activity. One clear explanation is that the catechol unit [95] increases conductivity, however, other factors may also be at play. These include the presence and distribution of different nitrogen species and the Fe–N_x sites [96–101], the possibility of mixed M–O_x [102] and/or Fe–N_xO_y sites [103], involvement and contribution of Fe/Fe₃C nanoparticles [89–92] and that of the organic ligand in the electrochemical processes [98, 99, 104, 105]. Notably, in the case of TAL–6–900, we observed formation of Fe₃O₄ but not Fe/Fe₃C nanocrystals. This observation suggests that the organic linker itself may not only modulate the rate of formation of nanocrystals embedded into the carbon support but also their composition.

Next, we wished to examine the performance of these newly developed iron-based heterogeneous catalysts in oxidation transformations of alkylarenes [78]. We compared reaction conditions for oxidation of toluene and ethylbenzene to benzoic acid and acetophenone, respectively (Table 3). We found that use of TAL-1 is not safe, because it led to rigorous reactions, including overheating and explosion. The carbonized material TAL-1-900, on the other hand, was safer and more robust.

Table 3. Optimization of reaction conditions for oxidation of toluene and ethylbenzene^a.



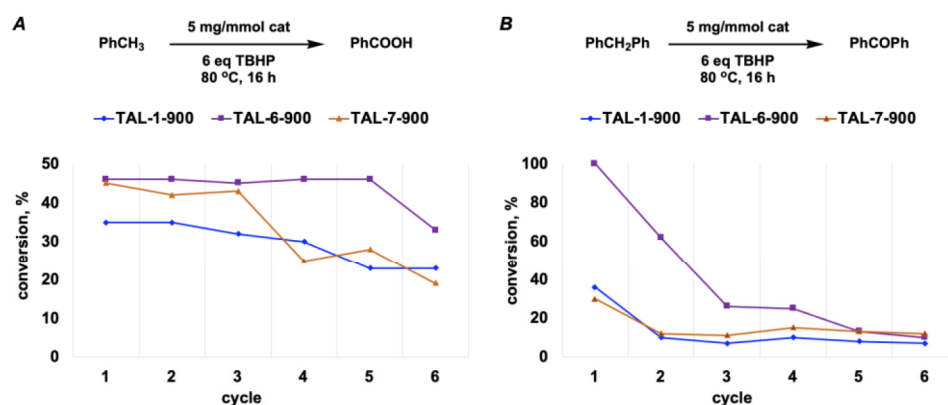
entry ^b	catalyst	equiv of TBHP	isolated yield, % reaction A	isolated yield, % reaction B
1	TAL-1	3	11	9
2	TAL-1	6	11	34
3	TAL-1	10	14	50
4	TAL-1-900	3	28	24
5	TAL-1-900	6	34	44
6 ^c	TAL-1-900	6	34	67
7	TAL-1-900	10	35	45

^a Reaction conditions: 70% aq. TBHP, neat, 80 °C, 16 h.

^b Catalyst loading: 5 mg/mmol of substrate, except entry 6.

^c Catalyst loading: 10 mg/mmol of substrate.

We then compared the three TAL catalysts in the recycling tests using toluene and diphenylmethane as substrates. Interestingly, over the course of time the diacid derived catalyst TAL-6-900 outperformed the rest of the catalysts (Fig. 8a).



^a Reaction conditions: 70% aq. TBHP, neat, 80 °C, 16 h; catalyst loading: 5 mg/mmol of substrate.

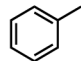
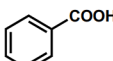
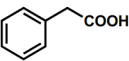
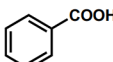
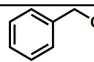
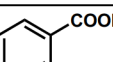
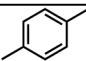
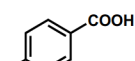
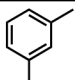
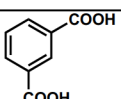
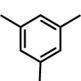
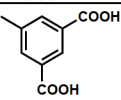
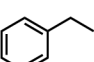
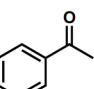
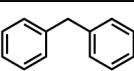
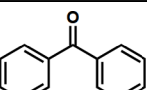
^b Yields were determined by NMR using 1,3,5-trimethoxybenzene as internal standard.

Figure 8. Stability of iron-based catalysts in oxidation of (A) toluene and (B) diphenylmethane.

However, based on the accessibility and cost-effectiveness within different TAL systems, the scope of the reaction was explored using TAL–1–900 (Table 4). We have focused on converting methylarenes to carboxylic acids [106] on a practical, lab-bench scale because the use of strong oxidants, typically, KMnO_4 , in the stoichiometric amounts is not sustainable. Recently, Bolm *et al.* introduced FeCl_3 -catalyzed conditions using pyridine as solvent and *tert*-butyl hydroperoxide (TBHP) as a terminal oxidant [107]. However, the conversion of methylarenes to carboxylic acids was less well explored with only one example of *p*-methylanisole having been reported.

In addition to toluene (entry 1), phenylacetic acid and benzyl alcohol were also converted to benzoic acid (entries 2–4). The former compound first undergoes oxidation to phenylglyoxylic acid, which is then decarboxylated by the TBHP radical [108, 109]. With polymethylarenes, only the major products were isolated (entries 5–7). *para*-Xylene formed *para*-toluic acid (entry 5), *meta*-xylene resulted in isophthalic acid (entry 6), and mesitylene gave uvic acid (entry 7). Ketones were obtained from ethylbenzene and diphenylmethane (entries 8–11). Increasing TBHP equivalents from 3 to 6 improved conversion to benzophenone, however, the isolated yield of acetophenone did not change significantly.

Table 4. TAL–1–900 catalyzed oxidations^a.

entry	substrate	major product	equiv of TBHP	isolated yield, %
1			6	37
2			3	49
3			6	70
4			3	84
5			12	34
6			12	32
7			18	38
8			3	50
9			6	54
10			3	47
11			6	94

^a Reaction conditions: TAL–1–900 (5 mg/mmol of substrate), 70% aq. TBHP, neat, 80 °C, 24 h.

In conclusion, we introduced a small library of novel, carbonaceous ligands for fabrication of M–N–C materials, where M = Fe. We have then tested them as bifunctional catalyst materials and extended their application to heterogeneous catalysis. Our data suggests that there is a nexus between the original ligand and the nature of nanoparticles entrapped into the material (Fe_3O_4 vs. Fe_3C), its catalytic activity and stability.

3 Multifunctional catalyst material from an amorphous cobalt metal–organic framework

Metal–organic frameworks, which are employed in fabrication of M–N–C materials are typically, *crystalline* [110]. For example, zinc and 2-methylimidazole-based ZIF–8 and cobalt and 2-methylimidazole-based ZIF–67 are morphologically rhombic dodecahedra [82, 111, 112]; iron and 2-aminoterephthalic acid-based MIL–88B–NH₂ crystals are needle-like bipyramidal hexagonal prisms [81, 113]; and zinc and triazole-based energetic MOF MET–6 crystals are octahedron shaped [83, 114]. Their corresponding topologies are often carried through the carbonization step.

In Chapter 2 we focused on iron-based *polycrystalline* MOFs [74, 78], Chapter 3, which is based on Publication III, will introduce the use of a cobalt-based *amorphous* metal–organic framework (aMOF) [115, 116] as a precursor for the synthesis of M–N–C materials.

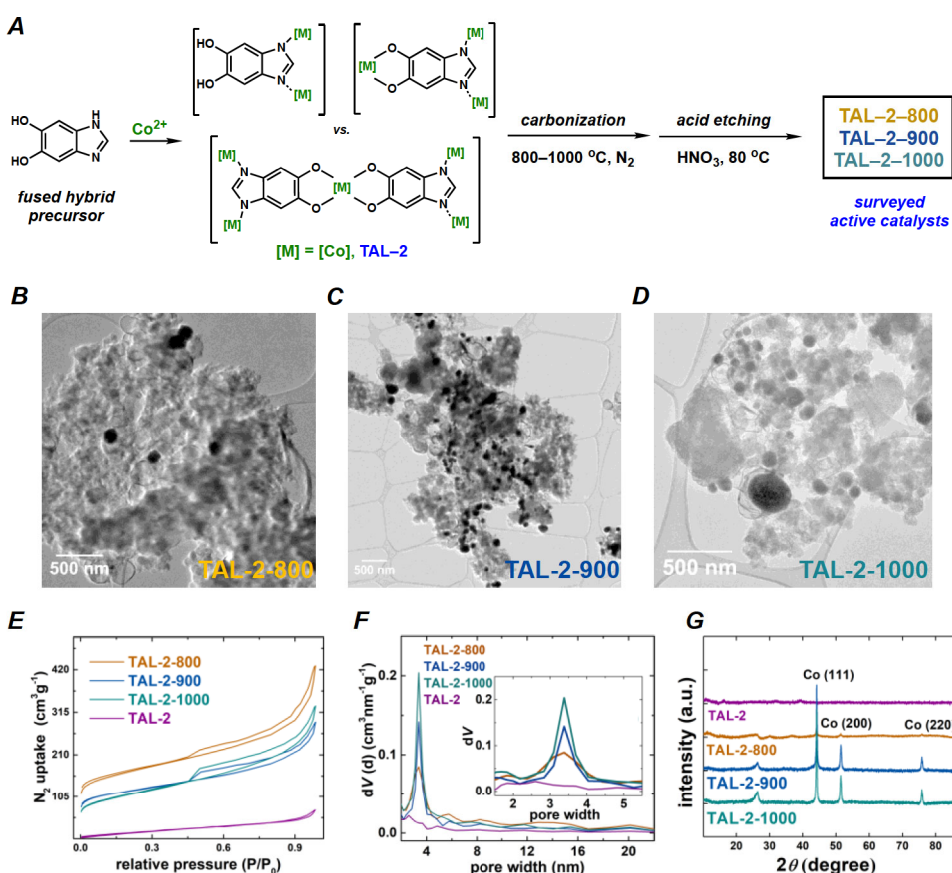


Figure 9. TAL-2 derived catalysts materials. (A) Preparation of materials. Morphological characterization by HRTEM micrographs of (B) TAL–2–800, (C) TAL–2–900 and (D) TAL–2–1000 catalysts. Physical characterization of the materials by (E) N₂ uptake, and (F) pore size distribution and (G) PXRD patterns. Adapted from ref [117].

We prepared a series of materials (TAL-2-800, TAL-2-900 and TAL-2-1000) using ligand **TL1** and CoCl₂ in 25% aq ammonia/DMF/EtOH/H₂O 4:10:10:15 solvent mixture followed by carbonization at three different temperatures 800, 900 and 1000 °C (Fig. 9a). We then tested them as heterogeneous catalysts in three electrocatalytic reactions (ORR, OER, HER) and two organic transformations.

All the materials incorporated metallic cobalt nanoparticles, albeit TAL-2-800 had fewer of them (HRTEM; Fig. 9b–9d, S1 and S2 in ref [117]). The distribution of pore sizes (3–4 nm) was determined from the nitrogen uptake curves (Fig. 9e and 9f). PXRD patterns indicated the presence of graphitic carbon and Co(0) nanoparticles (Fig. 9g).

The TAL-2 derived Co–N–C catalysts were then tested in oxidative conditions using low catalyst loadings (5 mg/mmol of substrate, 1.7 mol% Co) (Fig. 10). Interestingly, while several transformations of arylmethanes involving TBHP as an oxidant have been disclosed so far using the Fe–N–C systems [7, 8, 107, 74], the only instance employing Co–N–C catalyst is limited to just one substrate, ethylbenzene [118].

Overall, Co–N–C materials were more robust and more efficient as catalysts than the Fe–N–C catalysts derived from iron-based TAL precursors (*cf.* Fig. 8) [74, 78]. While TAL-2-900 was more effective for oxidation of toluene to benzoic acid, TAL-2-1000 remained active for six cycles when diphenylmethane was used as substrate.

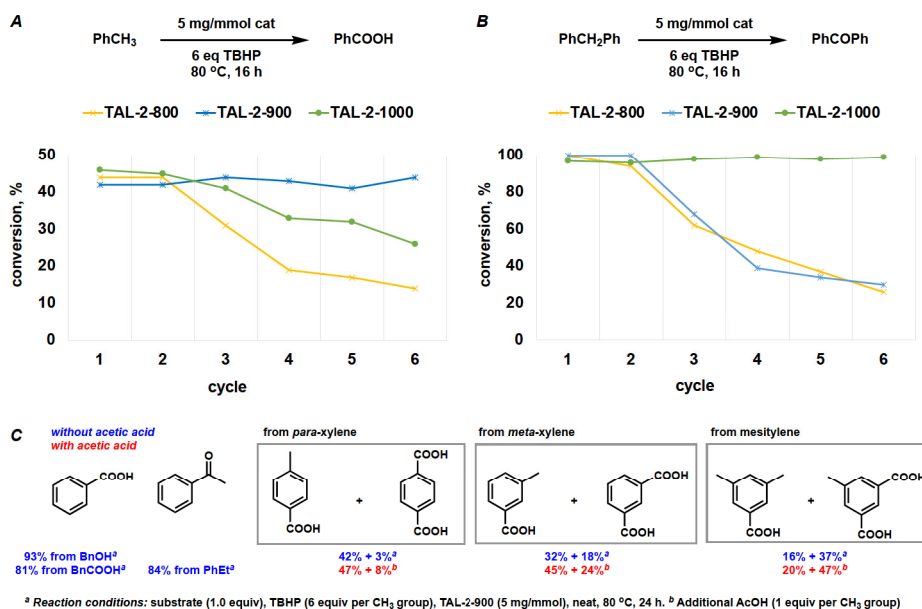


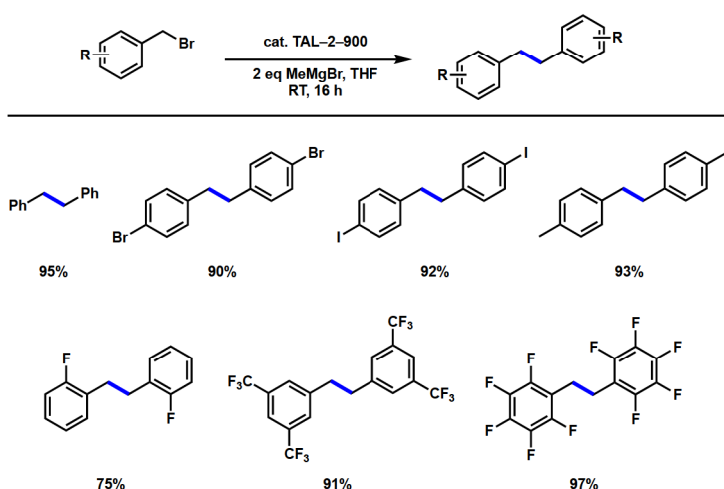
Figure 10. Use of TAL-derived catalysts in oxidative transformations. (A) Catalyst recyclability during oxidation of toluene into benzoic acid. (B) Catalyst recyclability during oxidation of diphenylmethane into benzophenone (conversion were determined by NMR using 1,3,5-trimethoxybenzene as internal standard). (C) Substrate scope for TAL-2-900-catalyzed oxidations (isolated yields). Adapted with changes from ref [117].

A screen of additives (AcOH, TCA, TFA, B(OMe)₃, TEA, pyridine) in the oxidation of toluene revealed that only acetic acid resulted in improved conversions and isolated yields. This effect was also confirmed with polymethylated substrates (Fig. 10c).

Since the oxidation reactions involve radical intermediates, we were keen to see whether it were possible to catalyze other radical transformations. We opted for the benzylic homocoupling reaction. This carbon–carbon bond forming reaction is typically carried out with stoichiometric lithium [119], magnesium [120], copper [121] or nickel [122]. Recently, photo- [123, 124] and Rh-catalyzed processes employing dimethylzinc [125] were reported.

Gratifyingly, when TAL–2–900 (5 mg/mmol, 1.7 mol%) was used as a catalyst together with methylmagnesium bromide, the desired homocoupling products were observed (Table 5). The catalyst was significantly deactivated when exposed to aqueous work-up. To recycle the catalyst, the solvent containing the product was removed using a syringe, and the reaction vessel was recharged with a new batch of starting material and MeMgBr.

Table 5. TAL–2–900 catalyzed $C(sp^3)$ – $C(sp^3)$ homocoupling reaction. Adapted from ref [117].



^a Reaction conditions: substrate (1.0 equiv), MeMgBr (2.0 equiv), TAL-2-900 (5 mg/mmol), THF, RT, 16 h

TAL–2 catalysts were profiled against the three electrochemical reactions: oxygen reduction (ORR), oxygen evolution (OER) and hydrogen evolution (HER) reactions (Fig. 11). TAL–2–900, once again, showed a superior activity profiles in all of these processes.

In ORR in 0.1 M KOH, TAL–2–900 ($421 \text{ m}^2 \text{ g}^{-1}$) was the best performing catalyst with an onset potential (E_{on}) of 1.00 V, a half-wave potential ($E_{1/2}$) of 0.85 V and a diffusion-limiting current density of -5.78 mA cm^{-2} (Fig. 11a–11c). The number of electrons transferred per O_2 molecule (n) was four. RRDE studies confirmed that oxygen reduction proceeds via a two-step 2×2 mechanism (Fig. S5b and S5c in ref [117]).

In OER in 0.1 M KOH, current density of 10 mA cm^{-2} for TAL–2–900 was achieved at 1.60 V (Fig. 11d–11f). In chronoamperometric studies (at 1.6 V), after 2.8 h the catalyst was proven to be stable, while the relative current density of a benchmark catalyst (RuO_2) had decreased to 74%.

The HER activity of TAL–2 derived materials was compared in both alkaline (1 M KOH) and acidic conditions (0.5 M H_2SO_4) against the commercial standard (Pt/C) at the current density of -10 mA cm^{-2} (Fig. 11g–11i). The best overpotential value (that for TAL–2–900) was achieved at -264 mV vs. RHE with a low Tafel slope value of 115 mV dec^{-1} .

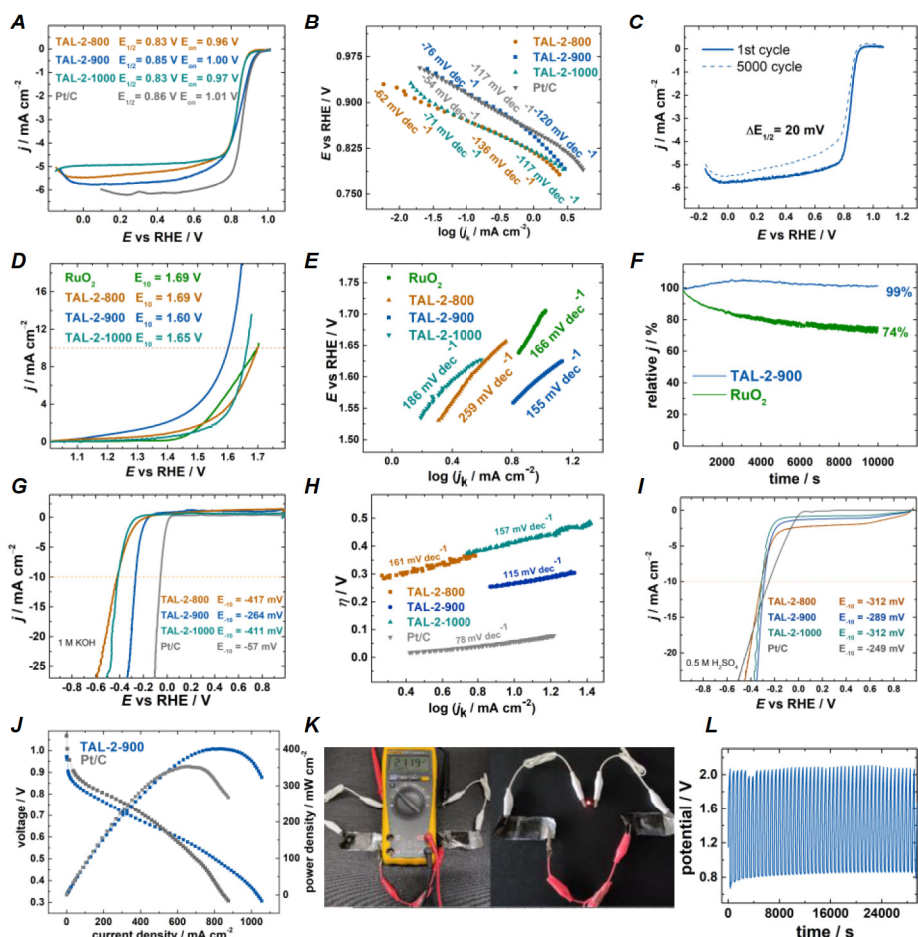


Figure 11. Electrochemical characterization of TAL-2 derived catalyst materials. (A) ORR polarization curves for TAL and Pt/C-modified GC electrodes at 1600 rpm; $v = 10 \text{ mV s}^{-1}$. (B) Tafel plots for ORR on TAL and Pt/C catalysts. (C) Electrochemical ORR stability test for TAL-2-900 (mid-range: 0.6–1.0 V). (D) OER polarization curves (under argon); $v = 10 \text{ mV s}^{-1}$. (E) OER Tafel plots. (F) OER chronoamperometric stability of TAL-2-900 and RuO_2 in 0.1 M KOH over 10,000 seconds (1.6 V). (G) HER polarization curves for TAL and Pt/C electrocatalysts in 1 M KOH; $v = 10 \text{ mV s}^{-1}$. (H) HER Tafel plots for TAL and Pt/C electrocatalysts in 1 M KOH. (I) HER polarization curves for TAL and Pt/C electrocatalysts in 0.5 M H_2SO_4 ; $v = 10 \text{ mV s}^{-1}$. (J) Alkaline single fuel cell test of TAL-2-900 and Pt/C. (K) Zinc–air battery testing with TAL-2-900, shows the voltage produced by two batteries, LED light using the same batteries, and (L) galvanostatic cycling of one battery for 8 h. Adapted from ref. [117].

Finally, TAL-2-900 was evaluated in alkaline electrolyte membrane fuel cell and zinc–air battery. At 2 mg cm^{-2} loading and HMT–PMBI as a polymer electrolyte, alkaline membrane fuel cell test yielded current density up to 1100 mA cm^{-2} (Fig. 11j), which was 20% better activity than Pt/C. The value of power density for TAL-2-900 was $>400 \text{ mW cm}^{-2}$, that above of Pt/C (350 mW cm^{-2}). Stability of solid-state PVA-based zinc–air battery with TAL-2-900 as an electrode material was examined at constant current density of 5.0 mA cm^{-2} (Fig. 11k and 11l). The TAL-2-900-driven zinc–air battery had a cycle life of 8 h.

In conclusion, we have demonstrated that amorphous metal–organic frameworks (coordination networks [126]) can be used to access new heterogeneous catalysts. Using TAL–2–900, we have shown their ability to catalyze various electrochemical and synthetic transformations, including $C(sp^3)–C(sp^3)$ carbon–carbon bond formation, the first example of use of carbonized material to carry out reactions in the presence of organometallic reagents.

4 Shungite as a carbon support for bifunctional oxygen electrocatalysts

The heterogeneous catalysts prepared from MOFs TAL-1 and TAL-2, which were discussed in Chapters 2 and 3, did not employ any carbon support. Typically, however, carbon supports such as CNTs, activated carbon or Vulcan XC72R are utilized [33]. In this Chapter, which is based on Publication V, I introduce shungite, a raw material, as a new carbon support [36].

Shungite is an accessible mineraloid containing 98% of carbon by weight, which was first found in Karelia, a northwestern region of Russia [127–129]. It has high conductivity and high specific surface area making it a potentially useful and affordable source of carbon [130, 131].

The raw shungite (Sh-raw) was first acid etched with a 1:1 mixture of 48% HF and 65% HNO₃ acids for 12 h at RT and washed with water and 2-propanol to give purified shungite (Sh). These steps ensured removal of traces of metals (Fe, Ni, Mg, Al, Si) and sulfur was confirmed by EDX analysis (Fig. 12).

The acid-etched shungite was modified during carbonization step with CoCl₂·6H₂O or Fe(OAc)₂ or a combination of both in the presence of the two most widely used nitrogen sources, dicyandiamide (DCDA) and melamine (mel) [67].

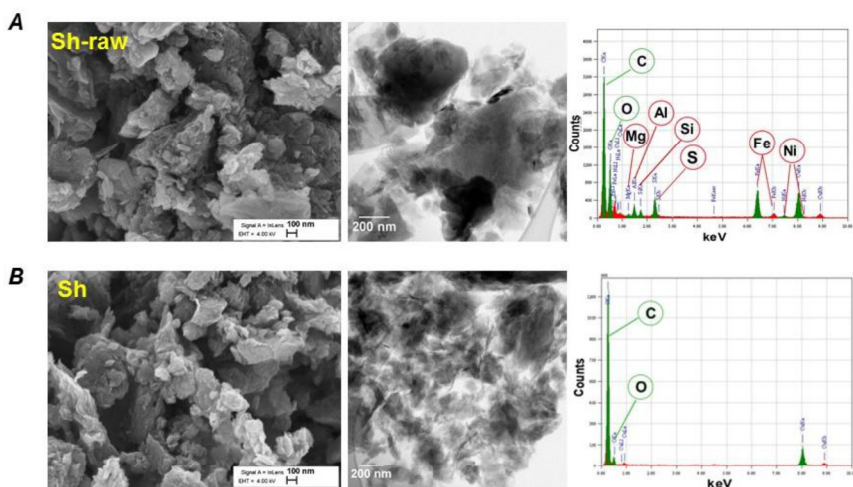


Figure 12. SEM and TEM micrographs and EDX spectra of (A) as-received shungite (Sh-raw) and (B) acid-etched shungite (Sh). Adapted with changes from ref. [36].

From the ORR and OER data, which were obtained in 0.1 M KOH with catalyst loading of 153 $\mu\text{g cm}^{-2}$ (Fig. 13), it is clear that only the materials derived from a mixture of the two metals showed superior bifunctional activities (ΔE for Sh–DCDA–CoFe and Sh–mel–CoFe are 0.84 V and 0.85 V, respectively).

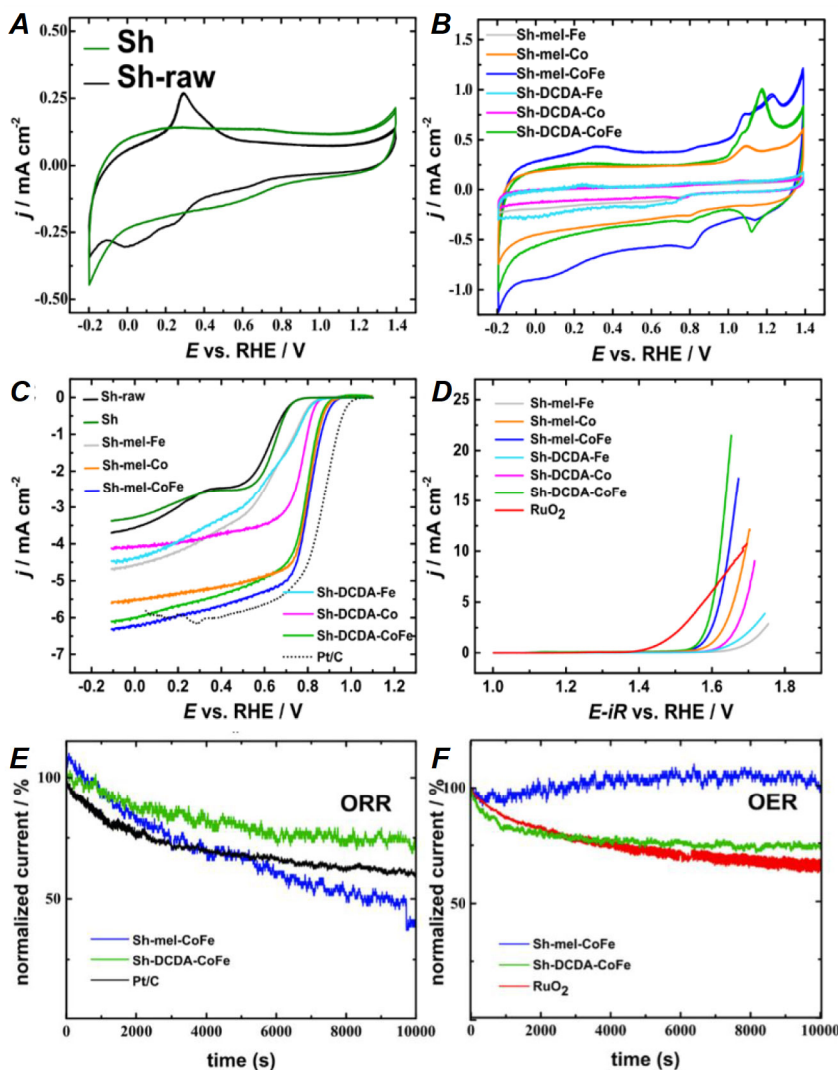


Figure 13. Characterization of DCDA and melamine modified electrocatalysts. Cyclic voltammetry curves for (A) undoped shungite and (B) all the doped shungite-based powders modified GC electrodes in argon-saturated 0.1 M KOH, scan rate 50 mV s^{-1} . (C) Comparison of ORR polarization curves at 1600 rpm, scan rate $v = 10 \text{ mV s}^{-1}$. (D) iR -corrected OER polarization curves in argon-saturated 0.1 M KOH at 10 mV s^{-1} . Current–time chronoamperometry response for (E) ORR at 0.75 V and (F) OER at 1.60 V vs. RHE. Adapted with changes from ref. [36].

We then characterized the Sh–DCDA–CoFe catalyst by STEM and HRTEM (Fig. 14). From the elemental mapping and HRTEM micrographs, it was evident that the mixed alloy FeCo nanoparticles were formed, which were also present in the spent catalyst (SI in ref. [36]), which means that they are essential for the catalytic activity.

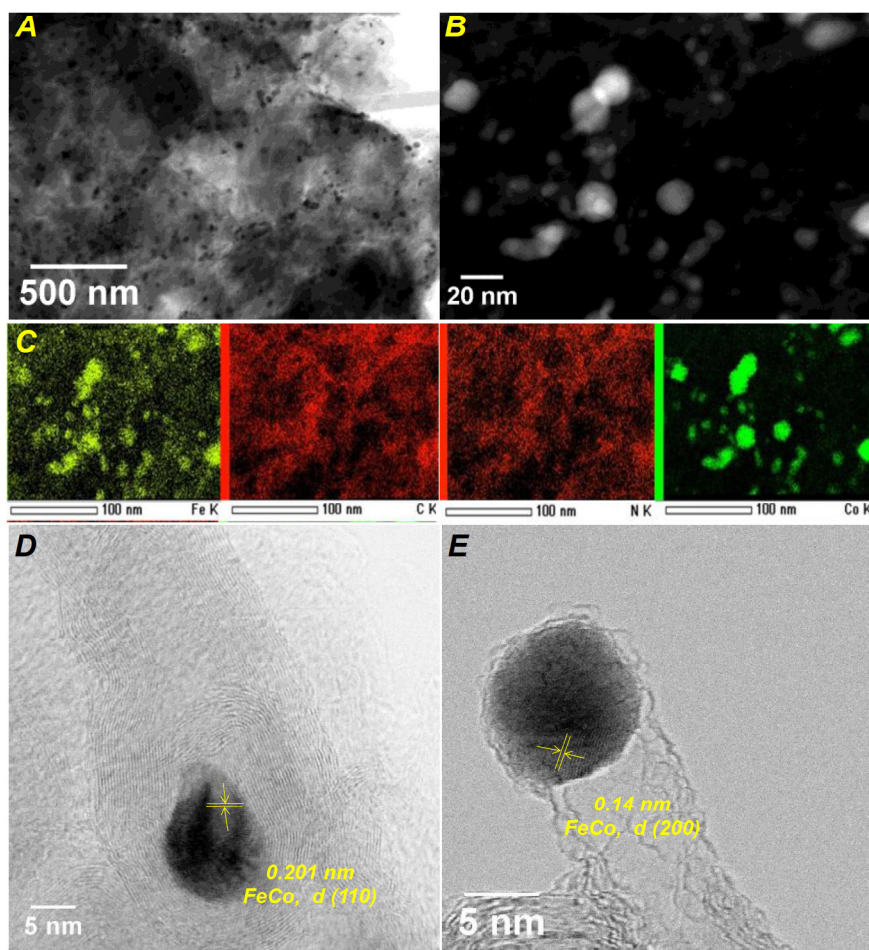


Figure 14. Characterization of Sh-DCDA-CoFe catalyst by STEM and TEM. Adapted with changes from ref. [36].

Additionally, we have tried to use acid-etched shungite as a carbon support together with MOFs ZIF-67, TAL-1 and TAL-2 as metal/nitrogen precursors. However, impregnation using ball milling or sonification did not result in highly active catalysts and needs further rounds of optimization (unpublished data).

In conclusion, we have demonstrated that shungite, a raw material, can serve as carbon support for bifunctional oxygen catalysts. Highly efficient bifunctional performance was achieved in the cases where FeCo alloy nanoparticles were formed. Direct modifications with MOFs as a single source of metal and nitrogen need further optimization.

5 Experimental section

General

Synthetic chemistry. All chemicals were used as supplied. Chromatographic separations were performed on ThoMar OHG silica gel 60Å (40–63 µm). Thin-layer chromatography was performed on Merck TLC Silica gel 60 F₂₅₄ and visualized by UV (365/254 nm), KMnO₄ and/or phosphomolybdic acid. ¹H and ¹³C NMR spectra were recorded on Bruker Avance 400 spectrometer. Residual solvent peaks were used as internal standards [132]. Chemical shifts are quoted in ppm using the following abbreviations: *s* singlet; *d* doublet; *t* triplet; *q* quartet; *qn* quintet; *sx* sextet; *non* nonet, *m* multiplet; *br* broad; or a combination thereof. The coupling constants *J* are measured in Hz. High resolution mass spectra (HRMS) were recorded on Agilent HPLC/Q-TOF G6540A mass spectrometer. Preparation of ligands **TL1**, **TL2** and **TL3** was previously reported in ref [78], and **TL5** and **TL6** in ref [87]. Preparation of metal–organic frameworks TAL–1, TAL–6 and TAL–7 was previously reported in ref [78], and TAL–20, and TAL–22 in ref [87]. Preparation of catalyst materials TAL–1–900, TAL–6–900 and TAL–7–900 was previously reported in ref [78], and TAL–20–900, and TAL–22–900 in ref [87]. Shungite was purchased from Strecker UG (Würzburg, Germany). All procedure of modifying of shungite-derived materials were previously described [36].

PXRD. The powder XRD pattern for TAL–1 were recorded on a Rigaku Ultima IV diffractometer with Cu Kα radiation (λ = 1.5406 Å, 40 kV at 40 mA) and using the silicon strip detector D/teX Ultra with the scan range of 2θ = 10.0–60.0°, scan step 0.02°, scan speed 5 deg/min. The powder XRD patterns for the rest including additional run for TAL–1 were recorded on a Bruker D8 Advanced diffractometer using Ni filtered Cu Kα radiation and LynxEye line detector. Scanning steps were 0.013° 2θ from 5° to 90° 2θ and total counting time was 173 s per step. The scan axis was 2θ/θ. JCPDS Cards No. for α-Fe (#87-0722), Fe₃C (#89-2867), Fe₃O₄ (#75-0033), α-Fe₂O₃ (#33-0664) and Co (#42-1467) were compared.

SEM. Surface morphology was studied by SEM using Zeiss Ultra–55. The solid was deposited onto the carbon tape (TAL–1, TAL–6, TAL–7 and TAL–2 samples were covered with a thin gold layer to improve conductivity).

XPS. The surface elemental composition was investigated by XPS using the Scienta SES–100 spectrometer. For preparing the samples, the catalytic materials were dispersed in isopropanol at a concentration of 2 mg mL^{–1} and deposited onto GC plates (1.1×1.1 cm). The samples were tested with a non-monochromatic twin anode X-ray tube (XR3E2), where the characteristic energies were 1253.6 eV (Mg K_{α1,2}, FWHM 0.68 eV) and 1486.6 eV (Al K_{α1,2}, FWHM 0.83 eV). The pressure in the analysis chamber was below 10^{–9} torr and the source power was 300 W. Survey spectra were obtained using the following parameters: energy range 800 to 0 eV, pass energy 200 eV, step size 0.5 eV. High resolution XPS scans were performed using pass energy 200 eV and step size 0.1 eV. An Ag wire attached to the sample holders was used for energy reference (Ag 3d_{5/2} at 367.8 eV), no charging effects were observed. Peak fitting was done using CasaXPS (version 2.3.16) software.

TEM. Scanning transmission electron microscopy was done using FEI Titan 200 with 200 keV electron beam. TEM measurements were also performed using a JEOL-2200FS FEG (S)TEM equipped with Schottky field emission gun (FEG) and operating at accelerating voltage of 200 kV. TEM samples were dispersed in 2-propanol and sonicated for 10 minutes. The resulted suspension was pipetted on a 200 mesh copper grid covered by carbon film.

BET. Low-temperature nitrogen adsorption was done at the boiling temperature of nitrogen (77K) by using the NOVAtouch LX² (Quantachrome Instruments). Specific surface (S_{BET}) of carbon samples was calculated from N₂ adsorption corresponding to the BET theory in the P/P_0 interval of 0.02–0.2, the total pore volume (V_{tot}), calculated at P/P_0 of 0.97. The calculations of pore size distribution and specific surface (S_{DFT}) from N₂ isotherms were done by using a quenched solid density functional theory (QSDFT) equilibria model for slit type pores.

MP–AES. Analytical samples were digested in Anton Paar Multiwave PRO microwave digestion system using NXF100 vessels (PTFE/TFM liner) in 8NXF100 rotor. TAL-X-900 samples (10 mg) were dissolved in 69% HNO₃ (4 mL) and H₂O₂ (2 mL), then 48% HF (0.1 mL) was added, the vessels were capped and digested in the microwave unit. After digestion, the samples were diluted using 2% HNO₃ to a final dilution factor of 61,000 and analyzed using Agilent 4210 MP–AES. Fe and Lu (an internal standard added online via a T-shaped micro-mixer) were measured at 371.993 and 547.669 nm, respectively.

Electroanalytical studies. All electrochemical measurements were performed in a three-electrode glass cell, using a rotating disk electrode (RDE) setup and an Autolab potentiostat/galvanostat PGSTAT30 (Eco Chemie B.V.). A glassy carbon (GC) rod served as counter electrode. Potentials were measured against a reversible hydrogen electrode (RHE) connected to the cell through a Luggin capillary. GC disks (geometric area of 0.126 cm²) polished to a mirror finish with 1 and 0.3 μm alumina slurries (Buehler) pressed into a Teflon holder served as working electrodes.

Prior to modification, the GC electrode was sonicated in both isopropanol and Milli-Q water for 5 min to remove polishing residues. The catalyst suspension was homogenized by sonication for 30 min and catalyst suspension was spin-coated onto the GC electrode and allowed to dry in air, yielding the catalyst loading of 500 μg cm^{−2}.

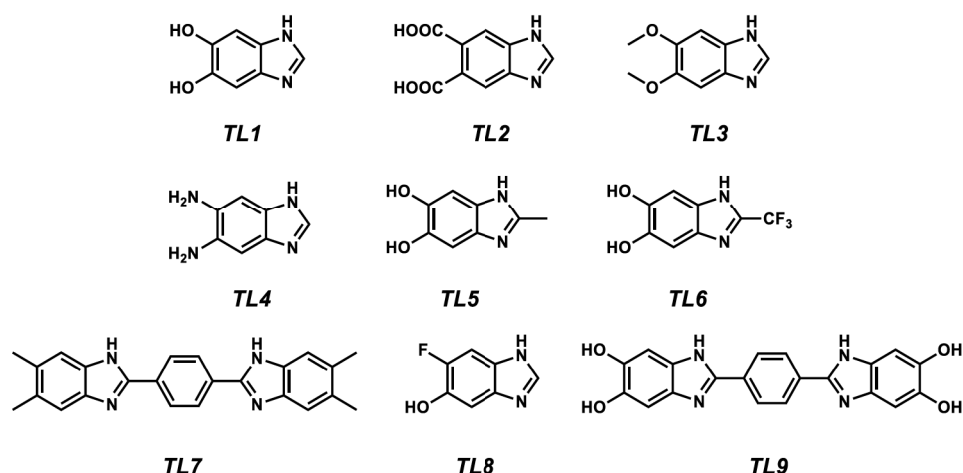
The electrolyte solution was prepared using Milli-Q water, KOH pellets (p.a. quality, Merck); saturated with pure O₂ (99.999%, AGA) and deaerated with argon (99.999%, AGA). Comparison experiments were performed with 20 wt% Pt/C (E-TEK; loading of 20 μg_{Pt} cm^{−2}) and 99.9% RuO₂ (Alfa Aesar; loading of 200 μg cm^{−2}).

The RDE technique was used to explore the electrocatalytic activity of the catalysts towards the ORR. Cyclic voltammograms were recorded at a potential sweep rate (v) of 50 mV s^{−1} in argon-saturated solution in the potential range of −0.1÷1.4 V. The RDE polarization curves were measured in O₂-saturated 0.1 M KOH solution at a scan rate of 10 mV s^{−1} in the potential range of −0.1÷1.1 V at different electrode rotation rates (ω): 360–4600 rpm. Electrode rotation rate was controlled using a CTV101 speed control unit connected to an EDI101 rotator (Radiometer). Background currents (not shown) were measured in argon-saturated solution at a scan rate 10 mV s^{−1} in the potential range of −0.1÷1.1 V. The background correction was made by subtracting background currents

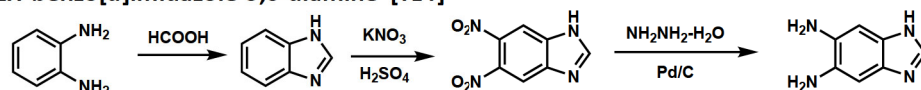
from the RDE data. The data was normalized to the geometric area of the GC electrode. The ORR and OER data were automatically corrected for iR drop using Nova software.

HER measurements were performed in Argon-saturated 1 M KOH solution. HER was measured also in 0.5 M H₂SO₄ solution. Before measurement electrodes were cycled 5 times at scan rate of 50 mV s⁻¹ and stable LSV was recorded at 10 mV s⁻¹ within the potential range of -0.8 to 1 V vs RHE.

Preparation of TL ligands



1H-benzo[d]imidazole-5,6-diamine [TL4]



1H-Benzo[d]imidazole

A mixture of *o*-phenylenediamine (15.00 g, 0.139 mol) and formic acid (100 mL) was left to stir at 100 °C. After 16 h, it was concentrated under reduced pressure, redissolved in water (200 mL), basified with K₂CO₃ and filtered to give the desired compound as a colorless solid (15.26 g, 0.130 mol, 94%).

¹H NMR (CD₃OD, 400 MHz) δ 8.14 (s, 1H), 7.62–7.58 (m, 2H), 7.27–7.23 (m, 2H)

¹³C NMR (CD₃OD, 100 MHz) δ 142.4, 123.8, 116.1.

5,6-Dinitro-1H-benzo[d]imidazole

KNO₃ (1.07 g, 10.58 mmol, 2.5 equiv.) was added to a solution of 1H-benzo[d]imidazole (500 mg, 4.23 mmol, 1.0 equiv.) in conc. H₂SO₄ (2 mL) at 0 °C and the mixture was left to stir at 50 °C. After 1 h, additional KNO₃ (2.14 g, 21.16 mmol, 5.0 equiv.) and conc. H₂SO₄ (2 mL) were added and the mixture was left to stir at 110 °C. After 8 h, crushed ice was added, the formed precipitate was collected by filtration and purified by flash chromatography (DCM/MeOH, 100:1) to give the desired compound as a light yellow solid (373.4 mg, 1.79 mmol, 42%).

¹H NMR (DMSO-*d*₆, 400 MHz) δ 8.77 (s, 1H), 8.49 (s, 2H).

¹³C NMR (DMSO-*d*₆, 100 MHz) δ 140.4, 131.3, 130.7, 105.0.

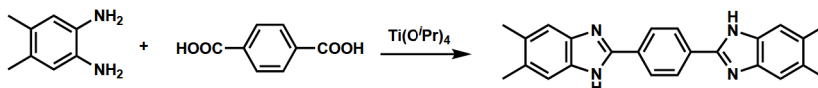
1*H*-Benzo[*d*]imidazole-5,6-diamine

Hydrazine monohydrate (3.1 mL, 63.74 mmol, 11.2 equiv) was added dropwise to a solution of 5,6-dinitro-1*H*-benzo[*d*]imidazole (1.179 g, 5.66 mmol, 1.0 equiv) and Pd/C (10 wt%, 0.12 g) in anhydrous EtOH (20 mL) at 0 °C and the mixture was left to stir at 80 °C. After 30 min, it was filtered through silica gel, and concentrated under reduced pressure to give the desired compound as a colorless solid (0.837 g, 5.65 mmol, quant).

¹H NMR (DMSO-*d*₆, 400 MHz) δ 7.67 (s, 1H), 6.71 (s, 2H), 4.28 (br s, 4H).

¹³C NMR (DMSO-*d*₆, 100 MHz) δ 137.6, 132.9, two carbons were not observed.

1,4-Bis(5,6-dimethyl-1*H*-benzo[*d*]imidazole-2-yl)benzene [TL7]



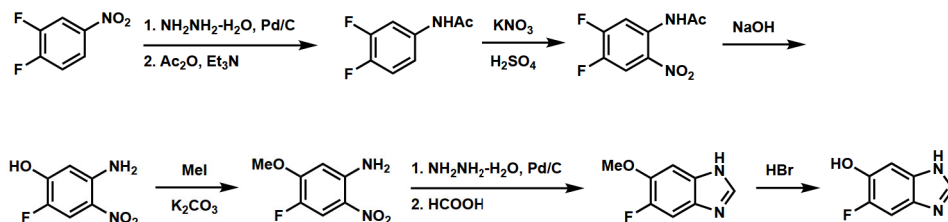
Terephthalic acid (1.74 g, 10.47 mmol, 1.0 equiv) was added into a mixture of 4,5-dimethylbenzene-1,2-diamine (3.00 g, 22.03 mmol, 2.1 equiv) in titanium isopropoxide (20 mL), the mixture was left to stir at 150 °C. After 16 h, the mixture was filtered, washed with MeOH, and dried to give the desired product as a light yellow solid (2.82 g, 7.69 mmol, 73%).

¹H NMR (DMSO-*d*₆, 400 MHz) δ 8.27 (s, 4H), 7.38 (s, 4H), 2.33 (s, 12H).

¹³C NMR (DMSO-*d*₆, 100 MHz) δ 150.0, 131.2, 130.8, 127.2, 126.6, 115.3, 20.1.

HRMS for C₂₄H₂₃N₄ [M+H]⁺ found 367.1906; calcd. 367.1917.

5-Fluoro-1*H*-benzo[*d*]imidazole-6-ol [TL8]



N-(3,4-Difluorophenyl)acetamide [133]

Hydrazine monohydrate (7.65 mL, 0.153 mol, 11.2 equiv) was added dropwise to a solution of 1,2-difluoro-4-nitrobenzene (2.17 g, 13.64 mmol, 1.0 equiv) and Pd/C (5 wt%, 0.108 g) in anhydrous EtOH (25 mL) at 0 °C and the mixture was left to stir at 80 °C. After 30 min, it was filtered through silica gel concentrated, redissolved in DCM (100 mL), washed with water (3×20 mL), dried over MgSO₄, and concentrated to 50 mL. Ac₂O (1.93 mL, 20.46 mmol, 1.5 equiv) and Et₃N (2.85 mL, 20.46 mmol, 1.5 equiv) were added at 0 °C to this solution and the mixture was left to stir at RT. After 1 h, it was concentrated, redissolved in CHCl₃ (100 mL), washed with 1 M HCl (30 mL), sat. NaHCO₃ solution (30 mL) and brine (30 mL), dried over Na₂SO₄ and concentrated to give the desired product as a colorless solid (1.79 g, 10.46 mmol, 77%).

¹H NMR (CDCl₃, 400 MHz) δ 7.62–7.56 (m, 1H), 7.52 (br s, 1H), 7.11–6.98 (m, 1H), 2.16 (s, 3H).

¹³C NMR (CDCl₃, 100 MHz) δ 168.6, 150.2 (*J*_{CF} = 246.0), 147.3 (*J*_{CF} = 271.0), 134.5 (*J*_{CF} = 11.8), 117.3 (*J*_{CF} = 18.0), 115.6, 109.9 (*J*_{CF} = 21.6).

***N*-(4,5-Difluoro-2-nitrophenyl)acetamide [133]**

KNO₃ (1.71 g, 16.97 mmol, 1.2 equiv.) was added into a solution of *N*-(3,4-difluorophenyl)acetamide (2.42, 14.14 mmol, 1.0 equiv.) in conc. H₂SO₄ (8 mL) on at 0 °C and the mixture was left to stir at 0 °C. After 3 h, ice was added, the formed precipitate was collected by filtration and washed with water to give the desired compound as a light yellow solid (2.43 g, 11.24 mmol, 80%).

¹H NMR (CDCl₃, 400 MHz) δ 10.45 (br s, 1H), 8.84 (dd, 1H, *J* = 12.8, 7.6), 8.12 (dd, 1H, *J* = 10.1, 8.0), 2.31 (s, 3H).

¹³C NMR (CDCl₃, 100 MHz) δ 169.2, 133.2, 115.0 (*J*_{CF} = 25.4), 110.8 (*J*_{CF} = 25.1), 25.8, two carbons were not observed.

5-Amino-2-fluoro-4-nitrophenol

A solution of *N*-(4,5-difluoro-2-nitrophenyl)acetamide (2.43 g, 11.24 mmol, 1.0 equiv) in 10% aq. NaOH (25 mL) was left to stir at 80 °C. After 16 h, it was allowed to cool to RT, acidified with conc. HCl, filtered, and washed with water to give the desired compound as a yellow solid (1.90 g, 11.04 mmol, 98%).

¹H NMR (DMSO-*d*₆, 400 MHz) δ 11.32 (br s, 1H, OH), 7.71 (d, 1H, *J* = 11.7), 7.42 (br s, 2H), 6.47 (d, 1H, *J* = 4.9).

¹³C NMR (CD₃OD, 100 MHz) δ 155.2, 147.0, 146.1, 143.7, 112.6 (*J*_{CF} = 23.2), 104.2.

4-Fluoro-5-methoxy-2-nitroaniline

A mixture of MeI (0.72 mL, 11.62 mmol, 2.0 equiv), 5-amino-2-fluoro-4-nitrophenol (1.00 g, 5.81 mmol, 1.0 equiv) and K₂CO₃ (1.20 g, 8.71 mmol, 1.5 equiv) in MeCN (10 mL) was left to stir at 70 °C. After 16 h, it was filtered, concentrated, redissolved in DCM, washed with water (3×30 mL), dried over Na₂SO₄ and concentrated to give the desired compound as a yellow solid (420 mg, 2.26 mmol, 39%).

¹H NMR (CDCl₃, 400 MHz) δ 7.86 (d, 1H, *J* = 11.6), 6.20 (d, 1H, *J* = 7.2), 6.17 (br s, 2H), 3.92 (s, 3H).

¹³C NMR (CDCl₃, 100 MHz) δ 155.3, 149.9, 143.8, 143.0, 112.5 (*J*_{CF} = 22.8), 99.9, 56.5.

5-Fluoro-6-methoxy-1*H*-benzo[d]imidazole

Hydrazine monohydrate (1.3 mL, 25.27 mmol, 10 equiv) was added dropwise to a solution of 4-fluoro-5-methoxy-2-nitroaniline (420 mg, 2.26 mmol, 1.0 equiv) and Pd/C (5 wt%, 21 mg) in anhydrous EtOH (20 mL) at 0 °C and the mixture was left to stir at 80 °C. After 90 min, it was filtered through silica gel, concentrated, redissolved in formic acid (30 mL) and was left to stir at 100 °C. After 16 h, the mixture was concentrated, redissolved in water (50 mL), basified with K₂CO₃ and extracted with DCM (3×10 mL) to give the desired compound as a light yellow solid (255.8 mg, 1.54 mmol, 68%).

¹H NMR (CD₃OD, 400 MHz) δ 8.07 (s, 1H), 7.32 (d, 1H, *J* = 11.1), 7.24 (d, 1H, *J* = 7.4), 3.91 (s, 3H).

¹³C NMR (CD₃OD, 100 MHz) δ 153.1, 150.7, 147.0, 142.5, 57.1, two carbons were not observed.

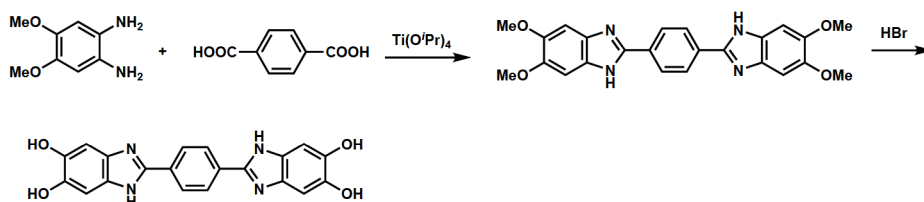
5-Fluoro-1*H*-benzo[d]imidazole-6-ol

A solution of 5-fluoro-6-methoxy-1*H*-benzo[d]imidazole (230 mg, 1.38 mmol, 1.0 equiv) in 48% aq. HBr (10 mL) was left to stir at 120 °C. After 4 h, the mixture was cooled down to RT, extracted with DCM (3×10 mL) and EtOAc (3×10 mL) to give the desired compound as a red solid (206.9 mg, 1.36 mmol, quant).

^1H NMR (CD_3OD , 400 MHz) δ 9.22 (s, 1H), 7.60 (d, 1H, $J = 9.9$), 7.31 (d, 1H, $J = 7.4$).

^{13}C NMR (CD_3OD , 100 MHz) δ 153.4 ($J_{\text{CF}} = 236.9$), 147.6, 140.3, 128.7, 124.6, 102.2 ($J_{\text{CF}} = 25.6$), 101.7 ($J_{\text{CF}} = 3.4$).

2,2'-(1,4-Phenylene)bis(1H-benzo[d]imidazole-5,6-diol) [TL9]



1,4-Bis(5,6-dimethoxy-1H-benzo[d]imidazole-2-yl)benzene

A mixture of terephthalic acid (1.51 g, 9.06 mmol, 1.0 equiv), 4,5-dimethoxybenzene-1,2-diamine (3.20 g, 19.02 mmol, 2.1 equiv) in titanium isopropoxide (20 mL) was left to stir at 150 °C. After 16 h, it was filtered, washed with methanol and dried to give the desired product as a light brown solid (2.02 g, 4.69 mmol, 52%).

^1H NMR ($\text{DMSO}-d_6$, 400 MHz) δ 12.74 (br s, 2H), 8.22 (s, 4H), 7.23 (s, 2H), 7.03 (s, 2H), 3.83 (s, 12H).

^{13}C NMR ($\text{DMSO}-d_6$, 100 MHz, rotamers are observed) δ 149.1, 147.2/146.5, 137.6, 130.8, 126.2, 101.6/94.3, 55.9.

2,2'-(1,4-Phenylene)bis(1H-benzo[d]imidazole-5,6-diol)

A solution of 1,4-bis(5,6-dimethoxy-1H-benzo[d]imidazole-2-yl)benzene (1.10 g, 2.56 mmol, 1.0 equiv) in 48% aq. HBr (30 mL) and was left to stir at 120 °C. After 48 h, it was cooled down to 0 °C, filtered, and the precipitate was washed with MeOH (10×50 mL) give the desired compound as a green solid (0.623 g, 1.66 mmol, 65%).

^1H NMR ($\text{DMSO}-d_6$, 400 MHz) δ 8.35 (s, 4H), 7.16 (s, 4H).

^{13}C NMR (CD_3OD , 100 MHz) δ 149.2, 129.4, 129.3, 98.8, one carbon not observed.

HRMS for $\text{C}_{20}\text{H}_{15}\text{N}_4\text{O}_4$ $[\text{M}+\text{H}]^+$ found 375.1075; calcd. 375.1088.

Preparation of TAL MOFs

General procedure A. Metal chloride salt (1.0 equiv) and organic ligand (2.0 equiv) were dissolved in a mixture of DMF/water (1:1) and mixture was left to stir at 100 °C. After 72 h, the mixture was cooled down to RT, centrifuged, washed with DMF (3×), and dried to give the desired material.

General procedure B. Metal chloride salt (1.0 equiv) and organic ligand (2.0 equiv) were dissolved in a mixture 25% aq. NH₃/DMF/EtOH/water (4:10:10:15), and the mixture was left to react at RT. After 24 h, it was washed with EtOH and dried to give the desired material.

TAL-2. CoCl₂·6H₂O (3.96 g, 16.64 mmol, 1.0 equiv) was added dropwise into a mixture of 1*H*-benzo[*d*]imidazole-5,6-diol (5.00 g, 33.30 mmol, 2.0 equiv) in 25% aq. NH₃/DMF/EtOH/water (4:10:10:15), the resulting solution was left to stir at RT. After 24 h, it was filtered, washed with EtOH and dried to give the desired material as a dark green solid (6.28 g).

TAL-13. A solution of FeCl₃·6H₂O (1.37 g, 5.07 mmol, 1.0 equiv) and 1*H*-benzo[*d*]imidazole-5,6-diamine (1.50 g, 10.14 mmol, 2.0 equiv) in DMF/water (5 mL/5 mL) was left to stir at 100 °C. After 72 h, the mixture was cooled down to RT, centrifuged, the precipitate was washed with DMF (3×10 mL), and dried to give the desired material as a black solid (1.36 mg).

TAL-23. A solution of FeCl₃·6H₂O (295 mg, 1.09 mmol, 1.0 equiv) and 1,4-bis(5,6-dimethyl-1*H*-benzo[*d*]imidazole-2-yl)benzene (800 mg, 2.18 mmol, 2.0 equiv) in 25% aq. NH₃/DMF/EtOH/water (4:10:10:15) was left to stir at RT. After 24 h, it was filtered, washed with EtOH and dried to give the desired material as a dark solid (1.03 g).

TAL-24. A solution of FeCl₃·6H₂O (178 mg, 0.659 mmol, 1.0 equiv) and 5-fluoro-1*H*-benzo[*d*]imidazole-6-ol (200 g, 1.31 mmol, 2.0 equiv) in DMF/water (2 mL/5 mL) was left to stir at 100 °C. After 72 h, the mixture was cooled down to RT, centrifuged, the precipitate was washed with DMF (3×10 mL), and dried to give the desired material as a black solid (35 mg).

TAL-25. A solution of FeCl₃·6H₂O (193 mg, 0.714 mmol, 1.0 equiv) and 2,2'-(1,4-phenylene)bis(1*H*-benzo[*d*]imidazole-5,6-diol) (534 mg, 1.43 mmol, 2.0 equiv) in DMF/water (4 mL/4 mL) was left to stir at 100 °C. After 72 h, the mixture was cooled down to RT, centrifuged, the precipitate was washed with DMF (3×10 mL), and dried to give the desired material as a brown solid (638 mg).

Preparation of carbonized TAL catalysts

Carbonization was done at 800–1000 °C (N₂, rapid heat, 2 h, slow cooling). The carbonized materials were suspended in a 1:1 mixture of 0.5 M H₂SO₄ and 0.5 M HNO₃ (for Fe-based MOFs) or 0.5 M HNO₃ (for Co-based MOFs), stirred for 8 h at 50 °C, filtered, and re-carbonized under N₂ at 900 °C for 2 h to give the acid leached materials.

Oxidations with Fe-based materials

Benzoic acid [134]

From toluene. A mixture of toluene (100 mg, 1.08 mmol, 1.0 equiv), TBHP (70% aq solution, 892 μ L, 6.51 mmol, 6.0 equiv) and TAL-1-900 (5.4 mg) was left to stir at 80 °C. After 24 h, it was filtered through a Celite pad using MeOH, concentrated under reduced pressure, the residue was redissolved in K₂CO₃ solution (10 mL), washed with DCM (2 \times 10 mL), the combined aqueous phase was acidified with HCl, extracted with DCM (3 \times 10 mL), dried over MgSO₄, and concentrated under reduced pressure to give the desired product as a colorless solid (48.4, 0.396 mmol, 37%).

From benzylalcohol. A mixture of benzyl alcohol (100 mg, 0.925 mmol, 1.0 equiv), TBHP (70% aq solution, 380 μ L, 2.77 mmol, 3.0 equiv) and TAL-1-900 (4.6 mg) was left to stir at 80 °C. After 24 h, it was filtered through a Celite pad using MeOH, concentrated under reduced pressure, the residue was redissolved in K₂CO₃ solution (10 mL), washed with DCM (2 \times 10 mL), the combined aqueous phase was acidified with HCl, extracted with DCM (3 \times 10 mL), dried over MgSO₄ and concentrated under reduced pressure to give the desired product as a colorless solid (94.5, 0.774 mmol, 84%).

From 2-phenylacetic acid with 3 equiv TBHP. A mixture of 2-phenylacetic acid (100 mg, 0.734 mmol, 1.0 equiv), TBHP (70% aq solution, 301 μ L, 2.20 mmol, 3.0 equiv) and TAL-1-900 (3.7 mg) was left to stir at 80 °C. After 24 h, it was filtered through a Celite pad using DCM, concentrated under reduced pressure, purified by flash chromatography (EtOAc/PE 1:20) to give the desired product as a colorless solid (43.6 mg, 0.357 mmol, 49%).

From 2-phenylacetic acid with 6 equiv TBHP. A mixture of 2-phenylacetic acid (100 mg, 0.734 mmol, 1.0 equiv), TBHP (70% aq solution, 602 μ L, 4.40 mmol, 6.0 equiv) and TAL-1-900 (3.7 mg) was left to stir at 80 °C. After 24 h, it was filtered through a Celite pad using DCM, concentrated under reduced pressure, purified by flash chromatography ((EtOAc/PE 1:20) to give the desired product as a colorless solid (62.8 mg, 0.514 mmol, 70%).

¹H NMR (400 MHz, CDCl₃) δ 8.13 (d, 2H, *J* = 7.1), 7.63 (t, 1H, *J* = 7.4), 7.49 (t, 2H, *J* = 7.7).

¹³C NMR (100 MHz, CDCl₃) δ 172.5, 134.0, 130.4, 129.4, 128.6.

Isophthalic acid [135]

A mixture of *m*-xylene (100 mg, 0.942 mmol, 1.0 equiv), TBHP (70% aq solution, 1.55 mL, 11.30 mmol, 12.0 equiv) and TAL-1-900 (4.7 mg) was left to stir at 80 °C. After 24 h, it was filtered through a Celite pad using MeOH, concentrated under reduced pressure and purified by flash chromatography (EtOAc/PE 1:20 \rightarrow 1:10) to give the desired product as a colorless solid (50.0 mg, 0.301 mmol, 32%).

¹H NMR (400 MHz, DMSO-*d*₆) δ 13.2 (s, 2H), 8.48 (s, 1H), 8.17 (d, 1H, *J* = 1.6), 8.15 (d, 1H, *J* = 1.6), 7.64 (t, 1H, *J* = 7.7)

¹³C NMR (100 MHz, DMSO-*d*₆) δ 166.6, 133.4, 131.2, 130.0, 129.2.

4-Methylbenzoic acid [136]

A mixture of *p*-xylene (100 mg, 0.942 mmol, 1.0 equiv), TBHP (70% aq solution, 1.55 mL, 11.30 mmol, 12.0 equiv) and TAL-1-900 (4.7 mg) was left to stir at 80 °C. After 24 h, it was filtered through a Celite pad using MeOH, concentrated under reduced pressure and purified by flash chromatography (EtOAc/PE 1:20) to give the desired product as a colorless solid (43.5 mg, 0.320 mmol, 34%).

¹H NMR (400 MHz, CDCl₃) δ 8.01 (d, 2H, *J* = 8.1), 7.28 (d, 2H, *J* = 8.1), 2.43 (s, 3H).

¹³C NMR (100 MHz, CDCl₃) δ 171.9, 144.8, 130.4, 129.4, 126.7, 21.9.

5-Methylisophthalic acid [137]

A mixture of mesitylene (100 mg, 0.832 mmol, 1.0 equiv), TBHP (70% aq solution, 2.05 mL, 14.98 mmol, 18.0 equiv) and TAL-1-900 (4.2 mg) was left to stir at 80 °C. After 24 h, it was filtered through a Celite pad using MeOH, concentrated under reduced pressure and purified by flash chromatography (EtOAc/PE 1:20→1:10) to give the desired product as a colorless solid (57.2 mg, 0.317 mmol, 38%).

¹H NMR (400 MHz, DMSO-*d*₆) δ 13.18 (s, 2H), 8.28 (s, 1H), 7.98 (s, 2H), 2.43 (s, 3H).

¹³C NMR (100 MHz, DMSO-*d*₆) δ 166.7, 138.8, 133.9, 131.2, 127.3, 20.6.

HRMS for C₉H₉O₄ [M+H]⁺ found 181.0496; calcd. 181.0495.

Acetophenone [138]

With 3 equiv TBHP. A mixture of ethylbenzene (100 mg, 0.942 mmol, 1.0 equiv), TBHP (70% aq solution, 387 μL, 2.83 mmol, 3.0 equiv) and TAL-1-900 (4.7 mg) was left to stir at 80 °C. After 24 h, it was filtered through a Celite pad using MeOH, concentrated under reduced pressure and purified by flash chromatography (EtOAc/PE 1:100) to give the desired compound as a colorless oil (56.9 mg, 0.474 mmol, 50%).

With 6 equiv TBHP. A mixture of ethylbenzene (100 mg, 0.942 mmol, 1.0 equiv), TBHP (70% aq solution, 774 μL, 5.66 mmol, 6.0 equiv) and TAL-1-900 (4.7 mg) was left to stir at 80 °C. After 24 h, it was filtered through a Celite pad using MeOH, concentrated under reduced pressure and purified by flash chromatography (EtOAc/PE 1:100) to give the desired compound as a colorless oil (61.2 mg, 0.509 mmol, 54%).

¹H NMR (400 MHz, CDCl₃) δ 7.96–7.93 (m, 2H), 7.57–7.53 (m, 1H), 7.47–7.43 (m, 2H), 2.59 (s, 3H).

¹³C NMR (100 MHz, CDCl₃) δ 198.2, 137.2, 133.2, 128.6, 128.4, 26.7.

Benzophenone [139]

With 3 equiv TBHP. A mixture of diphenylmethane (150 mg, 0.892 mmol, 1.0 equiv), TBHP (70% aq solution, 366 μL, 2.67 mmol, 3.0 equiv) and TAL-1-900 (4.5 mg) was left to stir at 80 °C. After 24 h, it was filtered through a Celite pad using DCM, concentrated under reduced pressure and purified by flash chromatography (EtOAc/PE 1:100) to give the desired compound as a colorless solid (76.6 mg, 0.420 mmol, 47%).

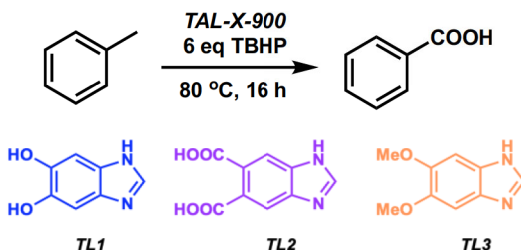
With 6 equiv TBHP. A mixture of diphenylmethane (150 mg, 0.892 mmol, 1.0 equiv), TBHP (70% aq solution, 732 μL, 5.34 mmol, 6.0 equiv) and TAL-1-900 (4.5 mg) was left to stir at 80 °C. After 24 h, it was filtered through a Celite pad using DCM, concentrated under reduced pressure and purified by flash chromatography (EtOAc/PE 1:100) to give the desired compound as a colorless solid (152.5 mg, 0.837 mmol, 94%).

¹H NMR (400 MHz, CDCl₃) δ 7.82–7.79 (m, 4H), 7.61–7.57 (m, 2H), 7.48 (t, 4H, *J* = 7.6).

¹³C NMR (100 MHz, CDCl₃) δ 196.9, 137.7, 132.5, 130.2, 128.4.

Oxidations with Co-based materials

Recyclability of TAL derived catalysts in oxidation of toluene into benzoic acid.^a

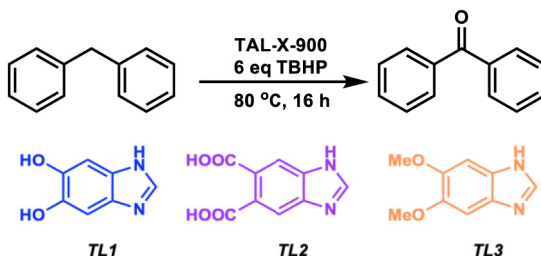


		reaction A							
		TAL-1-900	TAL-6-900	TAL-7-900	TAL-2-800	TAL-2-900	TAL-2-1000	TAL-26-900	TAL-27-900
		Fe	Fe	Fe	Co	Co	Co	Co	Co
		TL1	TL2	TL3	TL1	TL1	TL1	TL2	TL3
cycle	1	35%	46%	45%	44%	42%	46%	39%	41%
	2	35%	46%	42%	44%	42%	45%	31%	44%
	3	32%	45%	43%	31%	44%	41%	40%	27%
	4	30%	46%	25%	19%	43%	33%	24%	12%
	5	23%	46%	28%	17%	41%	32%	22%	16%
	6	23%	33%	19%	14%	44%	26%	8%	15%

^a Reaction conditions: toluene (100 mg), TAL-2-900 (5.4 mg), 6 equiv TBHP (892 μ L), 80 °C, 16 h.

^b NMR yield with 1,3,5-trimethoxybenzene as internal control

Recyclability of TAL derived catalysts in oxidation of diphenylmethane into benzophenone.^a

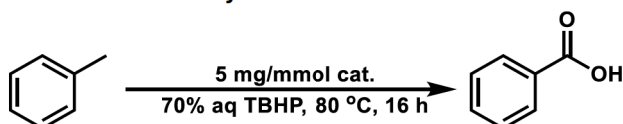


		reaction B							
		TAL-1-900	TAL-6-900	TAL-7-900	TAL-2-800	TAL-2-900	TAL-2-1000	TAL-26-900	TAL-27-900
		Fe	Fe	Fe	Co	Co	Co	Co	Co
		TL1	TL2	TL3	TL1	TL1	TL1	TL2	TL3
cycle	1	36%	100%	30%	100%	100%	93%	92%	64%
	2	10%	62%	12%	94%	100%	96%	100%	28%
	3	7%	26%	11%	62%	68%	98%	97%	24%
	4	10%	25%	15%	48%	39%	99%	73%	20%
	5	8%	13%	13%	37%	34%	98%	55%	16%
	6	7%	10%	12%	26%	30%	99%	46%	15%

^a Reaction conditions: diphenylmethane (150 mg), TAL-2-900 (4.5 mg), 6 equiv TBHP (732 μ L), 80 °C, 16 h.

^b NMR yield with 1,3,5-trimethoxybenzene as internal control.

Effect of additive in the oxidation of toluene to benzoic acid.^a



entry	additive	equiv	yield ^b
1	—	—	42%
2 ^c	—	—	0
3	TsOH	0.2	20%
4	AcOH	0.1	46%
5	AcOH	0.5	45%
6	AcOH	1.0	56%
7	AcOH	2.0	62%
8	AcOH	3.0	60%
9 ^c	AcOH	1.0	0%
10	AcOH+ B(OMe) ₃	1.0	41%
11	B(OMe) ₃	1.0	43%
12 ^d	AcOH	1.0	33%
13	TFA	0.1	25%
14	TFA	0.5	26%
15	TFA	1.0	17%
16	TFA	2.0	11%
17	TFA	3.0	4%
18	TCA	1.0	28%
19	benzoic acid	1.0	46%
20	Et ₃ N	0.1	34%
21	Et ₃ N	0.2	34%
22	Et ₃ N	0.5	34%
23	Et ₃ N	1.0	29%
24	pyridine	1.0	21%

^a Reaction conditions: toluene (100 mg), TAL–2–900 (5.4 mg), 6 equiv TBHP (892 μ L), 80 °C, 16 h

^b NMR yield with 1,3,5-trimethoxybenzene as internal control

^c 6 equiv of H₂O₂ as oxidant

^d MeCN (2 mL) as solvent

Benzoic acid [134]

From toluene. A mixture of toluene (100 mg, 1.08 mmol, 1.0 equiv), 70% TBHP (892 μ L, 6.48 mmol, 6.0 equiv) and TAL–2–900 (5.4 mg, 5 mg/mmol) was left to stir at 80 °C. After 24 h, it was filtered through a Celite pad using MeOH, concentrated under reduced pressure, the residue was redissolved in K₂CO₃ solution (10 mL), washed with DCM (2 \times 10 mL), the combined aqueous phase was acidified with HCl, extracted with DCM (3 \times 10 mL), dried over MgSO₄ and concentrated under reduced pressure to give the desired product as a colorless solid (59.7, 0.489 mmol, 45%).

From benzylalcohol. A mixture of benzyl alcohol (100 mg, 0.925 mmol, 1.0 equiv), 70% TBHP (760 μ L, 5.54 mmol, 6.0 equiv) and TAL–2–900 (4.6 mg, 5mg/mmol) was left to stir at 80 °C. After 24 h, it was filtered through a Celite pad using MeOH, concentrated under reduced pressure, the residue was redissolved in K₂CO₃ solution (10 mL), washed with DCM (2 \times 10 mL), the combined aqueous phase was acidified with HCl, extracted with DCM (3 \times 10 mL), dried over MgSO₄ and concentrated under reduced pressure to give the desired product as a colorless solid (105.2, 0.861 mmol, 93%).

From phenylacetic acid. A mixture of 2-phenylacetic acid (100 mg, 0.734 mmol, 1.0 equiv), 70% TBHP (602 μ L, 4.40 mmol, 6.0 equiv) and TAL-2-900 (3.7 mg, 5mg/mmol) was left to stir at 80 °C. After 24 h, it was filtered through a Celite pad using MeOH, concentrated under reduced pressure, purified by flash chromatography (EtOAc/PE 1:20) to give the desired product as a colorless solid (72.2 mg, 0.591 mmol, 81%).

^1H NMR (400 MHz, CDCl_3) δ 8.13 (d, 2H, J = 7.1), 7.63 (t, 1H, J = 7.4), 7.49 (t, 2H, J = 7.7).

^{13}C NMR (100 MHz, CDCl_3) δ 172.5, 134.0, 130.4, 129.4, 128.6.

Benzophenone [137]

A mixture of diphenylmethane (150 mg, 0.892 mmol, 1.0 equiv), 70% TBHP (732 μ L, 5.34 mmol, 6.0 equiv) and TAL-2-900 (4.5 mg, 5mg/mmol) was left to stir at 80 °C. After 24 h, it was filtered through a Celite pad using DCM, and concentrated under reduced pressure to give the desired compound as a colorless solid (157.4 mg, 0.864 mmol, 97%).

^1H NMR (400 MHz, CDCl_3) δ 7.82–7.79 (m, 4H), 7.61–7.57 (m, 2H), 7.48 (t, 4H, J = 7.6).

^{13}C NMR (100 MHz, CDCl_3) δ 196.9, 137.7, 132.5, 130.2, 128.4.

Acetophenone [138]

A mixture of ethylbenzene (100 mg, 0.942 mmol, 1.0 equiv), 70% TBHP (774 μ L, 5.66 mmol, 6.0 equiv) and TAL-2-900 (4.7 mg, 5mg/mmol) was left to stir at 80 °C. After 24 h, it was filtered through a Celite pad using MeOH, concentrated under reduced pressure and purified by flash chromatography (EtOAc/PE 1:100) to give the desired compound as a colorless oil (95.0 mg, 0.791 mmol, 84%).

^1H NMR (400 MHz, CDCl_3) δ 7.96–7.93 (m, 2H), 7.57–7.53 (m, 1H), 7.47–7.43 (m, 2H), 2.59 (s, 3H).

^{13}C NMR (100 MHz, CDCl_3) δ 198.2, 137.2, 133.2, 128.6, 128.4, 26.7.

4-Methylbenzoic acid [136] and Terephthalic acid [139]

A mixture of *p*-xylene (100 mg, 0.942 mmol, 1.0 equiv), 70% TBHP (1.55 mL, 11.30 mmol, 12.0 equiv) and TAL-2-900 (4.7 mg, 5mg/mmol) was left to stir at 80 °C. After 24 h, it was concentrated under reduced pressure and the residue was purified by flash chromatography (EtOAc/PE 1:20 \rightarrow 1:10) to give the desired products 4-methylbenzoic acid (53.8 mg, 0.395 mmol, 42%) and terephthalic acid (4.6 mg, 0.028 mmol, 3%), both as colorless solids.

The reaction was repeated in the presence of acetic acid (107.7 μ L, 1.884 mmol, 2 equiv) as an additive to give 4-methylbenzoic acid (60.7 mg, 0.446 mmol, 47%) and terephthalic acid (125 mg, 0.075 mmol, 8%).

4-Methylbenzoic acid [136]:

^1H NMR (400 MHz, CDCl_3) δ 8.01 (d, 2H, J = 8.1), 7.28 (d, 2H, J = 8.1), 2.43 (s, 3H).

^{13}C NMR (100 MHz, CDCl_3) δ 171.9, 144.8, 130.4, 129.4, 126.7, 21.9.

Terephthalic acid [139]:

^1H NMR (400 MHz, $\text{DMSO}-d_6$) δ 13.29 (s, 2H), 8.04 (s, 4H).

^{13}C NMR (100 MHz, $\text{DMSO}-d_6$) δ 166.7, 134.5, 129.5.

3-Methylbenzoic acid [139] and Isophthalic acid [135]

A mixture of *m*-xylene (100 mg, 0.942 mmol, 1.0 equiv), 70% TBHP (1.55 mL, 11.30 mmol, 12.0 equiv) and TAL-2-900 (4.7 mg, 5mg/mmol) was left to stir at 80 °C. After 24 h, it was concentrated under reduced pressure and the residue was purified by flash chromatography (EtOAc/PE 1:20 → 1:10) to give the desired products 3-methylbenzoic acid (40.9 mg, 0.300 mmol, 32%) and isophthalic acid (28.9 mg, 0.174 mmol, 18%) as colorless solid.

The reaction was repeated in the presence of acetic acid (107.7 μ L, 1.884 mmol, 2 equiv) as an additive, to give 3-methylbenzoic acid (58.1 mg, 0.427 mmol, 45%) and isophthalic acid (37.3 mg, 0.224 mmol, 24%).

3-Methylbenzoic acid [139]:

^1H NMR (400 MHz, DMSO- d_6) δ 12.86 (s, 1H), 7.76–7.73 (m, 2H), 7.43–7.35 (m, 2H), 2.35 (s, 3H).

^{13}C NMR (100 MHz, DMSO- d_6) δ 167.4, 137.9, 133.5, 130.7, 129.8, 128.5, 126.5, 20.8.

Isophthalic acid [135]:

^1H NMR (400 MHz, DMSO- d_6) δ 13.2 (s, 2H), 8.48 (s, 1H), 8.17 (d, 1H, $J = 1.6$), 8.15 (d, 1H, $J = 1.6$), 7.64 (t, 1H, $J = 7.7$).

^{13}C NMR (100 MHz, DMSO- d_6) δ 166.6, 133.4, 131.2, 130.0, 129.2.

3,5-Dimethylbenzoic acid [139] and 5-Methylisophthalic acid [137]

A mixture of mesitylene (100 mg, 0.832 mmol, 1.0 equiv), 70% aq TBHP (2.05 mL, 14.98 mmol, 18.0 equiv) and TAL-2-900 (4.2 mg, 5mg/mmol) was left to stir at 80 °C. After 24 h, it was concentrated under reduced pressure and the residue was purified by flash chromatography (EtOAc/PE 1:20 → 1:10) to give the desired products 3,5-dimethylbenzoic acid (20.5 mg, 0.137 mmol, 16%) and 5-methylisophthalic acid (55.6 mg, 0.309 mmol, 37%) as colorless solids.

The reaction was repeated in the presence of acetic acid (142.7 μ L, 2.496 mmol, 3 equiv) as an additive to give 3,5-dimethylbenzoic acid (24.6 mg, 0.164 mmol, 20%) and 5-methylisophthalic acid (70.7 mg, 0.392 mmol, 47%).

3,5-Dimethylbenzoic acid [139]:

^1H NMR (400 MHz, CDCl_3) δ 7.74 (s, 2 H), 7.24 (s, 1H).

^{13}C NMR (100 MHz, CDCl_3) δ 172.5, 138.3, 135.6, 129.3, 128.0, 21.3.

HRMS for $\text{C}_9\text{H}_9\text{O}_2$ $[\text{M}-\text{H}]^-$ found 149.0609; calcd. 149.0608.

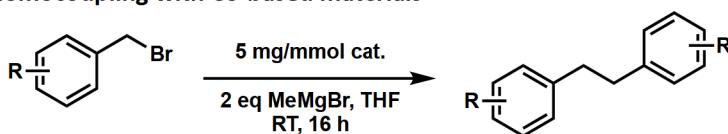
5-Methylisophthalic acid [137]:

^1H NMR (400 MHz, DMSO- d_6) δ 13.18 (s, 2H), 8.28 (s, 1H), 7.98 (s, 2H), 2.43 (s, 3H).

^{13}C NMR (100 MHz, DMSO- d_6) δ 166.7, 138.8, 133.9, 131.2, 127.3, 20.6.

HRMS for $\text{C}_9\text{H}_9\text{O}_4$ $[\text{M}+\text{H}]^+$ found 181.0496; calcd. 181.0495.

Benzylic homocoupling with Co-based materials



1,2-Diphenylethane [125]

A solution of MeMgBr (3 M in Et₂O, 876 μ L, 1.75 mmol, 2.0 equiv) was added dropwise into a solution of benzyl bromide (150 mg, 0.877 mmol, 1.0 equiv) and TAL-2-900 (4.4 mg, 5mg/mmol) in THF (5 mL) at 0 $^{\circ}$ C, and the reaction was left to stir at RT. After 16 h, it was quenched with 1 M HCl, extracted with DCM and evaporated under reduced pressure to give the product as a colorless solid (76.3 mg, 0.419 mmol, 95%).

¹H NMR (400 MHz, CDCl₃) δ 7.34–7.30 (m, 4H), 7.25–7.21 (m, 6H), 2.96 (s, 4H).

¹³C NMR (100 MHz, CDCl₃) δ 141.9, 128.6, 128.5, 126.0, 38.1.

1,2-Bis(4-bromophenyl)ethane [125]

A solution of MeMgBr (3 M in Et₂O, 600 μ L, 1.20 mmol, 2.0 equiv) was added dropwise into a solution of 4-bromobenzyl bromide (150 mg, 0.600 mmol, 1.0 equiv) and TAL-2-900 (3.0 mg, 5mg/mmol) in THF (5 mL) at 0 $^{\circ}$ C, and the mixture was left to stir at RT. After 16 h, it was quenched with 1 M HCl, extracted with DCM and evaporated under reduced pressure to give the product as a colorless solid (92.1 mg, 0.271 mmol, 90%).

¹H NMR (400 MHz, CDCl₃) δ 7.38 (d, 4 H, J = 8.3), 7.00 (d, 4H, J = 8.3), 2.85 (s, 4H).

¹³C NMR (100 MHz, CDCl₃) δ 140.2, 131.6, 130.4, 120.0, 37.2.

1,2-Bis(4-iodophenyl)ethane

A solution of MeMgBr (3 M in Et₂O, 337 μ L, 1.01 mmol, 2.0 equiv) was added dropwise into a solution of 4-iodobenzyl bromide (150 mg, 0.505 mmol, 1.0 equiv) and TAL-2-900 (2.5 mg, 5mg/mmol) in THF (5 mL) at 0 $^{\circ}$ C, and the mixture was left to stir at RT. After 16 h, it was quenched with 1 M HCl, extracted with DCM and evaporated under reduced pressure to give the product as a colorless solid (101.3 mg, 0.233 mmol, 92%).

¹H NMR (400 MHz, CDCl₃) δ 7.59 (d, 4H, J = 8.3), 6.88 (d, 4H, J = 8.3), 2.83 (s, 4H).

¹³C NMR (100 MHz, CDCl₃) δ 140.8, 137.4, 130.6, 91.2, 37.1.

HRMS for C₁₄H₁₃I₂ [M+H]⁺ found 434.9058; calcd. 434.9107.

1,2-Di-*p*-tolylethane [125]

A solution of MeMgBr (3 M in Et₂O, 540 μ L, 1.62 mmol, 2.0 equiv) was added dropwise into a solution of 4-iodobenzyl bromide (150 mg, 0.811 mmol, 1.0 equiv) and TAL-2-900 (4.1 mg, 5mg/mmol) in THF (5 mL) at 0 $^{\circ}$ C, and the mixture was left to stir at RT. After 16 h, it was quenched with 1 M HCl, extracted with DCM and evaporated under reduced pressure to give the product as a colorless solid (79.1 mg, 0.376 mmol, 93%).

¹H NMR (400 MHz, CDCl₃) δ 7.17 (s, 8H), 2.95 (s, 4H), 2.41 (s, 6H).

¹³C NMR (100 MHz, CDCl₃) δ 139.0, 135.4, 129.1, 128.4, 27.8, 21.1.

1,2-Bis(2-fluorophenyl)ethane

A solution of MeMgBr (3 M in Et₂O, 529 μ L, 1.59 mmol, 2.0 equiv) was added dropwise into a solution of 2-fluorobenzyl bromide (150 mg, 0.794 mmol, 1.0 equiv) and TAL-2-900 (4.0 mg, 5mg/mmol) in THF (5 mL) at 0 $^{\circ}$ C, and the mixture was left to stir at RT. After 16 h, it was quenched with 1 M HCl, extracted with DCM and evaporated under reduced pressure to give the product as a colorless solid (65.2 mg, 0.299 mmol, 75%).

^1H NMR (400 MHz, CDCl_3) δ 7.21–7.11 (m, 4H), 7.05–6.99 (m, 4H), 2.95 (s, 4H).

^{13}C NMR (100 MHz, CDCl_3) δ 161.3 (d, $J_{\text{CF}} = 243$), 130.9 (d, $J_{\text{CF}} = 5$), 128.4 (d, $J_{\text{CF}} = 15$), 127.9 (d, $J_{\text{CF}} = 8$), 124.0 (d, $J_{\text{CF}} = 3$), 115.3 (d, $J_{\text{CF}} = 22$), 29.9.

^{19}F NMR (376 MHz, CDCl_3) δ -119.0 – -119.1 (m).

1,2-Bis(3,5-bis(trifluoromethyl)phenyl)ethane:

A solution of MeMgBr (3 M in Et_2O , 326 μL , 0.977 mmol, 2.0 equiv) was added dropwise into a solution of 2-fluorobenzyl bromide (150 mg, 0.489 mmol, 1.0 equiv) and TAL-2-900 (2.4 mg, 5mg/mmol) in THF (5 mL) at 0 $^\circ\text{C}$, and the mixture was left to stir at RT. After 16 h, it was quenched with 1 M HCl, extracted with DCM and evaporated under reduced pressure to give the product as a colorless solid (101.2 mg, 0.223 mmol, 91%).

^1H NMR (400 MHz, CDCl_3) δ 7.76 (s, 2H), 7.58 (s, 4H), 3.11 (s, 4H).

^{13}C NMR (100 MHz, CDCl_3) δ 142.7, 132.1 (q, $J_{\text{CF}} = 33$), 128.8 (d, $J_{\text{CF}} = 2$), 123.4 (q, $J_{\text{CF}} = 271$, CF_3), 120.8 (p, $J_{\text{CF}} = 4$), 37.1.

^{19}F NMR (376 MHz, CDCl_3) δ -63.0.

1,2-Bis(perfluorophenyl)ethane [125]

A solution of MeMgBr (3 M in Et_2O , 383 μL , 1.15 mmol, 2.0 equiv) was added dropwise into a solution of 2-fluorobenzyl bromide (150 mg, 0.575 mmol, 1.0 equiv) and TAL-2-900 (2.9 mg, 5mg/mmol) in THF (5 mL) at 0 $^\circ\text{C}$, and the mixture was left to stir at RT. After 16 h, it was quenched with 1 M HCl, extracted with DCM, evaporated under reduced pressure to give the product as a colorless solid (100.7 mg, 0.278 mmol, 97%).

^1H NMR (400 MHz, CDCl_3) δ 3.02 (s, 4H).

^{13}C NMR (100 MHz, CDCl_3) δ 146.6–146.4 (m), 141.6–141.4 (m), 136.5–136.2 (m), 113.1–112.7 (m), 22.0.

^{19}F NMR (376 MHz, CDCl_3) δ -144.3 to -144.4 (m), -155.9 (t, $J = 20.6$), -162.0 to -162.2 (m).

Conclusions

In my PhD work, I have explored and have shown that the use of well-defined, novel single MOF precursors-derived materials is essential for their applications in both heterogeneous and electrocatalysis. Advanced, rationally designed organic linkers do play a role in determining the efficiency and the recyclability of the underlying catalysts. Namely,

- [1] I have designed, prepared and identified the most cost-effective and readily accessible benzimidazole-based ligands, which go on to form materials that serve as efficient bifunctional oxygen catalysts;
- [2] I have extended the use of TAL-1 (iron) and TAL-2 (cobalt) derived materials in oxidative transformations, electrochemical transformations and have applied them to building and testing the solid-state zinc—air batteries;
- [3] I have optimized the cobalt-based TAL-2 derived systems to acts as multifunctional catalysts in ORR, OER, HER, oxidative and benzylic homocoupling transformations;
- [4] By having developed a novel family of benzimidazole-based MOF precursors (nine in total) with the functional groups modulating their electronic and ligating properties, I have demonstrated that there is a link between the electronic and ligating properties of an initial organic ligand and the properties of the final M–N–C catalyst.

References

- [1] Chen, Y.Z.; Zhang, R.; Jiao, L.; Jiang, H.L. Metal–organic framework-derived porous materials for catalysis. *Coord. Chem. Rev.* **2018**, *362*, 1–23.
[DOI:10.1016/j.ccr.2018.02.008](#)
- [2] Jagadeesh, R.; Surkus, A.; Junge, H.; Pohl, M.; Radnik, J.; Rabeah, J.; Huan, H.; Schünemann, V.; Brückner, A.; Beller, M. Nanoscale Fe₂O₃-based catalysts for selective hydrogenation of nitroarenes to anilines. *Science* **2013**, *342*, 1073–1076.
[DOI:10.1126/science.1242005](#)
- [3] Sahoo, B.; Kreyenschulte, C.; Agostini, G.; Lund, H.; Bachmann, S.; Scalone, M.; Junge, K.; Beller, M. A robust iron catalyst for the selective hydrogenation of substituted (iso)quinolones. *Chem. Sci.* **2018**, *9*, 8134–8141.
[DOI:10.1039/C8SC02744G](#)
- [4] Li, J.; Liu, J.; Zhou, H.; Fu, Y. Catalytic transfer hydrogenation of furfural to furfuryl alcohols over nitrogen-doped carbon-supported iron catalyst. *ChemSusChem* **2016**, *9*, 1339–1347.
[DOI:10.1002/cssc.201600089](#)
- [5] Cui, X.; Li, Y.; Bachmann, S.; Scalone, M.; Surkus, A.; Junge, K.; Topf, C.; Beller, M. Synthesis and characterization of iron–nitrogen-doped graphene/core–shell catalysts: efficient oxidative dehydrogenation of N-heterocycles. *J. Am. Chem. Soc.* **2015**, *137*, 10652–10658.
[DOI:10.1021/jacs.5b05674](#)
- [6] Jagadeesh, R. V.; Junge, H.; Beller, M. “Nanorust”-catalyzed benign oxidation of amines for selective synthesis of nitriles. *ChemSusChem* **2015**, *8*, 92–96.
[DOI:10.1002/cssc.201402613](#)
- [7] Liu, W.; Zhang, L.; Liu, X.; Liu, X.; Yang, X.; Miao, S.; Wang, W.; Wang, A.; Zhang, T. Discriminating catalytically active FeN_x species of atomically dispersed Fe–N–C catalyst for selective oxidation of the C–H bond. *J. Am. Chem. Soc.* **2017**, *139*, 10790–10798.
[DOI:10.1021/jacs.7b05130](#)
- [8] Song, T.; Ma, Z.; Yuan, Y.; Xiao, J.; Yang, Y.; Ren, P. A bifunctional iron nanocomposite catalyst for efficient oxidation of alkenes to ketones and 1, 2-diketones. *ACS Catal.* **2020**, *10*, 4617–4629.
[DOI:10.1021/acscatal.9b05197](#)
- [9] Westerhaus, F.A.; Jagadeesh, R.V.; Wienhöfer, G.; Pohl, M.M.; Radnik, J.; Surkus, A.E.; Rabeah, J.; Junge, K.; Junge, H.; Nielsen, M.; Brückner, A.; Beller, M. 2013. Heterogenized cobalt oxide catalysts for nitroarene reduction by pyrolysis of molecularly defined complexes. *Nat. Chem.* **2013**, *5*, 537–543.
[DOI:10.1038/nchem.1645](#)
- [10] Liu, W.; Zhang, L.; Yan, W.; Liu, X.; Yang, X.; Miao, S.; Wang, W.; Wang, A.; Zhang, T.; Single-atom dispersed Co–N–C catalyst: structure identification and performance for hydrogenative coupling of nitroarenes. *Chem. Sci.* **2016**, *7*, 5758–5764.
[DOI:10.1039/C6SC02105K](#)
- [11] Zhou, P.; Zhang, Z. One-pot reductive amination of carbonyl compounds with nitro compounds by transfer hydrogenation over Co–N_x as catalyst. *ChemSusChem* **2017**, *10*, 1892–1897.
[DOI:10.1002/cssc.201700348](#)

- [12] Xie, F.; Xie, R.; Zhang, J.X.; Jiang, H.F.; Du, L.; Zhang, M. Direct reductive quinolyl β -C-H alkylation by multispherical cavity carbon-supported cobalt oxide nanocatalysts. *ACS Catal.* **2017**, *7*, 4780–4785.
[DOI:10.1021/acscatal.7b01337](https://doi.org/10.1021/acscatal.7b01337)
- [13] Chen, F.; Surkus, A.; He, L.; Pohl, M.; Radnik, J.; Topf, C.; Junge, K.; Beller, M. Selective catalytic hydrogenation of heteroarenes with n-graphene-modified cobalt nanoparticles (Co_3O_4 -Co/NGr@ α - Al_2O_3). *J. Am. Chem. Soc.* **2015**, *137*, 36, 11718–11724.
[DOI:10.1021/jacs.5b06496](https://doi.org/10.1021/jacs.5b06496)
- [14] Chen, F.; Li, W.; Sahoo, B.; Kreyenschulte, C.; Agostini, G.; Lund, H.; Junge, K.; Beller, M. Hydrogenation of pyridines using a nitrogen-modified titania-supported cobalt catalyst. *Angew. Chem.* **2018**, *130*, 14696–14700.
[DOI:10.1002/anie.201803426](https://doi.org/10.1002/anie.201803426)
- [15] Chen, F.; Kreyenschulte, C.; Radnik, J.; Lund, H.; Surkus, A.E.; Junge, K.; Beller, M. Selective semihydrogenation of alkynes with N-graphitic-modified cobalt nanoparticles supported on silica. *ACS Catal.* **2017**, *7*, 1526–1532.
[DOI:10.1021/acscatal.6b03140](https://doi.org/10.1021/acscatal.6b03140)
- [16] Luo, H.; Wang, L.; Shang, S.; Li, G.; Lv, Y.; Gao, S.; Dai, W. Cobalt nanoparticles-catalyzed widely applicable successive C–C bond cleavage in alcohols to access esters. *Angew. Chem. Int. Ed.* **2020**, ASAP.
[DOI:10.1002/anie.202008261](https://doi.org/10.1002/anie.202008261)
- [17] Zhong, W.; Liu, H.; Bai, C.; Liao, S.; Li, Y. Base-free oxidation of alcohols to esters at room temperature and atmospheric conditions using nanoscale Co-based catalysts. *ACS Catal.* **2015**, *5*, 1850–1856.
[DOI:10.1021/cs502101c](https://doi.org/10.1021/cs502101c)
- [18] Chen, H.; Shen, K.; Mao, Q.; Chen, J.; Li, Y. Nanoreactor of MOF-derived yolk-shell Co@C–N: Precisely controllable structure and enhanced catalytic activity. *ACS Catal.* **2018**, *8*, 1417–1426.
[DOI:10.1021/acscatal.7b03270](https://doi.org/10.1021/acscatal.7b03270)
- [19] Nie, R.; Chen, J.; Chen, M.; Qi, Z.; Goh, T.W.; Ma, T.; Zhou, L.; Pei, Y.; Huang, W. Aerobic oxidation of the C–H bond under ambient conditions using highly dispersed Co over highly porous N-doped carbon. *Green Chem.* **2019**, *21*, 1461–1466.
[DOI:10.1039/C8GC03653E](https://doi.org/10.1039/C8GC03653E)
- [20] Bai, C.; Yao, X.; Li, Y. Easy access to amides through aldehydic C–H bond functionalization catalyzed by heterogeneous Co-based catalysts. *ACS Catal.* **2015**, *5*, 884–891.
[DOI:10.1021/cs501822r](https://doi.org/10.1021/cs501822r)
- [21] Masa, J.; Xia, W.; Muhler, M.; Schuhmann, W. On the role of metals in nitrogen-doped carbon electrocatalysts for oxygen reduction. *Angew. Chem. Int. Ed.* **2015**, *54*, 10102–10120.
[DOI:10.1002/anie.201500569](https://doi.org/10.1002/anie.201500569)
- [22] Wu, Z.P.; Lu, X.F.; Zang, S.Q.; Lou, X.W. Non-noble-metal-based electrocatalysts toward the oxygen evolution reaction. *Adv. Funct. Mater.* **2020**, *30*, 1910274.
[DOI:10.1002/adfm.201910274](https://doi.org/10.1002/adfm.201910274)
- [23] Tahir, M.; Pan, L.; Idrees, F.; Zhang, X.; Wang, L.; Zou, J.J.; Wang, Z.L. Electrocatalytic oxygen evolution reaction for energy conversion and storage: a comprehensive review. *Nano Energy* **2017**, *37*, 136–157.
[DOI:10.1016/j.nanoen.2017.05.022](https://doi.org/10.1016/j.nanoen.2017.05.022)

- [24] Zhang, L.; Xiao, J.; Wang, H.; Shao, M. Carbon-based electrocatalysts for hydrogen and oxygen evolution reactions. *ACS Catal.* **2017**, *7*, 7855–7865.
[DOI:10.1021/acscatal.7b02718](https://doi.org/10.1021/acscatal.7b02718)
- [25] Qing, G.; Ghazfar, R.; Jackowski, S.T.; Habibzadeh, F.; Ashtiani, M.M.; Chen, C.P.; Smith III, M.R.; Hamann, T.W. Recent advances and challenges of electrocatalytic N₂ reduction to ammonia. *Chem. Rev.* **2020**, *120*, 5437–5516.
[DOI:10.1021/acs.chemrev.9b00659](https://doi.org/10.1021/acs.chemrev.9b00659)
- [26] Nitopi, S.; Bertheussen, E.; Scott, S.B.; Liu, X.; Engstfeld, A.K.; Horch, S.; Seger, B.; Stephens, I.E.; Chan, K.; Hahn, C.; Nørskov, J.K.; Jaramillo, T.F.; Chorkendorff, I. Progress and perspectives of electrochemical CO₂ reduction on copper in aqueous electrolyte. *Chem. Rev.* **2019**, *119*, 7610–7672.
[DOI:10.1021/acs.chemrev.8b00705](https://doi.org/10.1021/acs.chemrev.8b00705)
- [27] Yoon, T.P.; Jacobsen, E.N. Privileged chiral catalysts. *Science* **2003**, *299*, 1691–1693.
[DOI:10.1126/science.1083622](https://doi.org/10.1126/science.1083622)
- [28] He, Y.; Liu, S.; Priest, C.; Shi, Q.; Wu, G. Atomically dispersed metal–nitrogen–carbon catalysts for fuel cells: advances in catalyst design, electrode performance, and durability improvement. *Chem. Soc. Rev.* **2020**, *49*, 3484–3524.
[DOI:10.1039/C9CS00903E](https://doi.org/10.1039/C9CS00903E)
- [29] Wang, A.; Li, J.; Zhang, T. Heterogeneous single-atom catalysis. *Nat. Rev. Chem* **2018**, *2*, 65–81.
[DOI:10.1038/s41570-018-0010-1](https://doi.org/10.1038/s41570-018-0010-1)
- [30] Wang, Y.; Su, H.; He, Y.; Li, L.; Zhu, S.; Shen, H.; Xie, P.; Fu, X.; Zhou, G.; Feng, C.; Zhao, D.; Xiao, F.; Zhu, X.; Zeng, Y.; Shao, M.; Chen, S.; Wu, G.; Zeng, J.; Wang, C. Advanced electrocatalysts with single-metal-atom active sites. *Chem. Rev.* **2020**, *120*, 12217–12314.
[DOI:10.1021/acs.chemrev.0c00594](https://doi.org/10.1021/acs.chemrev.0c00594)
- [31] Bai, L.; Hsu, C.S.; Alexander, D.T.; Chen, H.M.; Hu, X. A cobalt–iron double–atom catalyst for the oxygen evolution reaction. *J. Am. Chem. Soc.* **2019**, *141*, 14190–14199.
[DOI:10.1021/jacs.9b05268](https://doi.org/10.1021/jacs.9b05268)
- [32] Ahn, M.; Cha, I.Y.; Cho, J.; Ham, H.C.; Sung, Y.E.; Yoo, S.J. Rhodium–Tin binary nanoparticle—a strategy to develop an alternative electrocatalyst for oxygen reduction. *ACS Catal.* **2017**, *7*, 5796–5801.
[DOI:10.1021/acscatal.7b02402](https://doi.org/10.1021/acscatal.7b02402)
- [33] Jayaraman, T.; Murthy, A.P.; Elakkiya, V.; Chandrasekaran, S.; Nithyadharseni, P.; Khan, Z.; Senthil, R.A.; Shanker, R.; Raghavender, M.; Kuppusami, P.; Jagannathan, M.; Ashokkumari, M. Recent development on carbon based heterostructures for their applications in energy and environment: A review. *J. Ind. Eng. Chem.* **2018**, *64*, 16–59.
[DOI:10.1016/j.jiec.2018.02.029](https://doi.org/10.1016/j.jiec.2018.02.029)
- [34] Zhan, X.; Si, C.; Zhou, J.; Sun, Z. MXene and MXene-based composites: synthesis, properties and environment-related applications. *Nanoscale Horiz.* **2020**, *5*, 235–258.
[DOI:10.1039/C9NH00571D](https://doi.org/10.1039/C9NH00571D)

- [35] Wang, W.; Chen, W.; Miao, P.; Luo, J.; Wei, Z.; Chen, S. NaCl crystallites as dual-functional and water-removable templates to synthesize a three-dimensional graphene-like macroporous Fe–NC catalyst. *ACS Catal.* **2017**, *7*, 6144–6149. DOI:10.1021/acscatal.7b01695
- [36] Kazimova, N.; Ping, K.; Danilson, M.; Merisalu, M.; Aruväli, J.; Käärik, M.; Mikli, V.; Leis, J.; Tammeveski, K.; Starkov, P.; Kongi, N. Shungite-derived graphene as a carbon support for bifunctional oxygen electrocatalysts. *J. Catal.* **2021**, *395*, 178–187. DOI:10.1016/j.jcat.2021.01.004
- [37] Wang, L.; Sofer, Z.; Pumera, M. Will any crap we put into graphene increase its electrocatalytic effect? *ACS Nano.* **2020**, *14*, 21–25. DOI:10.1021/acsnano.9b00184
- [38] Huang, J.; Zhao, B.; Liu, T.; Mou, J.; Jiang, Z.; Liu, J.; Li, H.; Liu, M. Wood-derived materials for advanced electrochemical energy storage devices. *Adv. Funct. Mater.* **2019**, *29*, 1902255. DOI:10.1002/adfm.201902255
- [39] Alonso-Lemus, I.L.; Figueroa-Torres, M.Z.; Lardizabal-Gutiérrez, D.; Bartolo-Pérez, P.; Carrillo-Rodríguez, J.C.; Rodríguez-Varela, F.J. Converting chicken manure into highly active N–P co-doped metal-free biocarbon electrocatalysts: effect of chemical treatment on their catalytic activity for the ORR. *Sustain. Energy Fuels* **2019**, *3*, 1307–1316. DOI:10.1039/C8SE00583D
- [40] Yang, W.; Li, J.; Ye, D.; Zhu, X.; Liao, Q. Bamboo charcoal as a cost-effective catalyst for an air-cathode of microbial fuel cells. *Electrochim. Acta* **2017**, *224*, 585–592. DOI:10.1016/j.electacta.2016.12.046
- [41] Meng, W.; Bai, X.; Wang, B.; Liu, Z.; Lu, S.; Yang, B. Biomass-derived carbon dots and their applications. *Energy Environ. Mater.* **2019**, *2*, 172–192. DOI:10.1002/eem2.12038
- [42] Veerakumar, P.; Panneer Muthuselvam, I.; Hung, C.T.; Lin, K.C.; Chou, F.C.; Liu, S.B. Biomass-derived activated carbon supported Fe₃O₄ nanoparticles as recyclable catalysts for reduction of nitroarenes. *ACS Sustainable Chem. Eng.* **2016**, *4*, 6772–6782. DOI:10.1021/acssuschemeng.6b01727
- [43] Cheon, J.Y.; Kim, T.; Choi, Y.; Jeong, H.Y.; Kim, M.G.; Sa, Y.J.; Kim, J.; Lee, Z.; Yang, T.H.; Kwon, K.; Terasaki, O.; Park, G. G.; Adzic, R. R.; Joo, S.H. Ordered mesoporous porphyrinic carbons with very high electrocatalytic activity for the oxygen reduction reaction. *Sci. Rep.* **2013**, *3*, 2715. DOI:10.1038/srep02715
- [44] Zhang, J.; Liu, X.; Xing, A.; Liu, J. Template-oriented synthesis of nitrogen-enriched porous carbon nanowhisker by hollow TiO₂ spheres nanothorns for methanol electrooxidation. *ACS Appl. Energy Mater.* **2018**, *1*, 2758–2768. DOI:10.1021/acsaem.8b00420
- [45] Bonakdarpour, A.; Tucker, R.T.; Fleischauer, M.D.; Beckers, N.A.; Brett, M.J.; Wilkinson, D.P. Nanopillar niobium oxides as support structures for oxygen reduction electrocatalysts. *Electrochim. Acta* **2012**, *85*, 492–500. DOI:10.1016/j.electacta.2012.08.005

- [46] Zhang, Z.; Liu, J.; Gu, J.; Su, L.; Cheng, L. An overview of metal oxide materials as electrocatalysts and supports for polymer electrolyte fuel cells. *Energy Environ. Sci.* **2014**, *7*, 2535–2558.
[DOI:10.1039/C3EE43886D](https://doi.org/10.1039/C3EE43886D)
- [47] Shen, C.; Chen, H.; Liu, Z. The Co–NC catalyst synthesized with a hard-template and etching method to achieve well-dispersed active sites for ethylbenzene oxidation. *Front. Chem.* **2019**, *7*, 426.
[DOI:10.3389/fchem.2019.00426](https://doi.org/10.3389/fchem.2019.00426)
- [48] Kamitaka, Y.; Takeshita, T.; Morimoto, Y. MgO-templated mesoporous carbon as a catalyst support for polymer electrolyte fuel cells. *Catalysts* **2018**, *8*, 230.
[DOI:10.3390/catal8060230](https://doi.org/10.3390/catal8060230)
- [49] Hu, B.C.; Wu, Z.Y.; Chu, S.Q.; Zhu, H.W.; Liang, H.W.; Zhang, J. Yu, S.H. SiO₂-protected shell mediated templating synthesis of Fe–N-doped carbon nanofibers and their enhanced oxygen reduction reaction performance. *Energy Environ. Sci.* **2018**, *11*, 2208–2215.
[DOI:10.1039/C8EE00673C](https://doi.org/10.1039/C8EE00673C)
- [50] Pérez-Mayoral, E.; Matos, I.; Bernardo, M.; Fonseca, I.M. New and advanced porous carbon materials in fine chemical synthesis. Emerging precursors of porous carbons. *Catalysts* **2019**, *9*, 133.
[DOI:10.3390/catal9020133](https://doi.org/10.3390/catal9020133)
- [51] Kaneti, Y.V.; Tang, J.; Salunkhe, R.R.; Jiang, X.; Yu, A.; Wu, K.C.W.; Yamauchi, Y. Nanoarchitected design of porous materials and nanocomposites from metal-organic frameworks. *Adv. Mater.* **2017**, *29*, 1604898.
[DOI:10.1002/adma.201604898](https://doi.org/10.1002/adma.201604898)
- [52] Xia, W.; Mahmood, A.; Zou, R.; Xu, Q. Metal–organic frameworks and their derived nanostructures for electrochemical energy storage and conversion. *Energy Environ. Sci.* **2015**, *8*, 1837–1866.
[DOI:10.1039/C5EE00762C](https://doi.org/10.1039/C5EE00762C)
- [53] Xie, F.; Lu, G.P.; Xie, R.; Chen, Q.H.; Jiang, H.F.; Zhang, M.; MOF-derived subnanometer cobalt catalyst for selective C–H oxidative sulfonylation of tetrahydroquinoxalines with sodium sulfinates. *ACS Catal.* **2019**, *9*, 2718–2724.
[DOI:10.1021/acscatal.9b00037](https://doi.org/10.1021/acscatal.9b00037)
- [54] Bouwkamp-Wijnoltz, A.; Visscher, W.; Van Veen, J.; Boellaard, E.; Van der Kraan, A.; Tang, S. On active-site heterogeneity in pyrolyzed carbon-supported iron porphyrin catalysts for the electrochemical reduction of oxygen: An *in situ* Mössbauer study. *J. Phys. Chem. B* **2002**, *106*, 12993–13001.
[DOI:10.1021/jp0266087](https://doi.org/10.1021/jp0266087)
- [55] Chen, R.; Li, H.; Chu, D.; Wang, G. Unraveling oxygen reduction reaction mechanisms on carbon-supported Fe-phthalocyanine and Co-phthalocyanine catalysts in alkaline solutions. *J. Phys. Chem. C* **2009**, *113*, 20689–20697.
[DOI:10.1021/jp906408y](https://doi.org/10.1021/jp906408y)
- [56] Wang, W.; Hong, X.; Yao, Q.; Lu, Z.H. Bimetallic Ni–Pt nanoparticles immobilized on mesoporous N-doped carbon as a highly efficient catalyst for complete hydrogen evolution from hydrazine borane. *J. Mater. Chem. A* **2020**, *8*, 13694–13701.
[DOI:10.1039/D0TA05322H](https://doi.org/10.1039/D0TA05322H)

- [57] Fei, H.; Ye, R.; Ye, G.; Gong, Y.; Peng, Z.; Fan, X.; Samuel, E.L.; Ajayan, P.M.; Tour, J.M. Boron–and nitrogen–doped graphene quantum dots/graphene hybrid nanoplatelets as efficient electrocatalysts for oxygen reduction. *ACS Nano* **2014**, *8*, 10837–10843.
[DOI:10.1021/nn504637y](https://doi.org/10.1021/nn504637y)
- [58] Zhao, J.; Chen, Z. Carbon-doped boron nitride nanosheet: An efficient metal-free electrocatalyst for the oxygen reduction reaction. *J. Phys. Chem. C* **2015**, *119*, 26348–26354.
[DOI:10.1021/acs.jpcc.5b09037](https://doi.org/10.1021/acs.jpcc.5b09037)
- [59] Long, X.; Li, Z.; Gao, G.; Sun, P.; Wang, J.; Zhang, B.; Zhong, J.; Jiang, Z.; Li, F. Graphitic phosphorus coordinated single Fe atoms for hydrogenative transformations. *Nat. Commun.* **2020**, *11*, 4074.
[DOI:10.1038/s41467-020-17903-0](https://doi.org/10.1038/s41467-020-17903-0)
- [60] Yuan, K.; Lützenkirchen-Hecht, D.; Li, L.; Shuai, L.; Li, Y.; Cao, R.; Qiu, M.; Zhuang, X.; Leung, M.K.; Chen, Y.; Scherf, U. Boosting oxygen reduction of single iron active sites via geometric and electronic engineering: nitrogen and phosphorus dual coordination. *J. Am. Chem. Soc.* **2020**, *142*, 2404–2412.
[DOI:10.1021/jacs.9b11852](https://doi.org/10.1021/jacs.9b11852)
- [61] Ahn, S.H.; Manthiram, A. Cobalt phosphide coupled with heteroatom-doped nanocarbon hybrid electrocatalysts for efficient, long-life rechargeable zinc–air batteries. *Small* **2017**, *13*, 1702068.
[DOI:10.1002/sml.201702068](https://doi.org/10.1002/sml.201702068)
- [62] Lin, G.; Wang, Q.; Yang, X.; Cai, Z.; Xiong, Y.; Huang, B. Preparation of phosphorus-doped porous carbon for high performance supercapacitors by one-step carbonization. *RSC Adv.* **2020**, *10*, 17768–17776.
[DOI:10.1039/D0RA02398A](https://doi.org/10.1039/D0RA02398A)
- [63] Xi, W.; Yan, G.; Lang, Z.; Ma, Y.; Tan, H.; Zhu, H.; Wang, Y.; Li, Y. Oxygen–doped nickel iron phosphide nanocube arrays grown on ni foam for oxygen evolution electrocatalysis. *Small* **2018**, *14*, 1802204.
[DOI:10.1002/sml.201802204](https://doi.org/10.1002/sml.201802204)
- [64] Lin, X.; Jie, S.; Liu, Z. Sulfur and nitrogen-doped porous cobalt carbon catalyst for high efficient aerobic oxidation of hydrocarbons. *Mol. Catal.* **2018**, *455*, 143–149.
[DOI:10.1016/j.mcat.2018.05.031](https://doi.org/10.1016/j.mcat.2018.05.031)
- [65] Fu, L.; Chen, Y.; Zhao, S.; Liu, Z.; Zhu, R. Sulfur-mediated synthesis of N–doped carbon supported cobalt catalysts derived from cobalt porphyrin for ethylbenzene oxidation. *RSC Adv.* **2016**, *6*, 19482–19491.
[DOI:10.1039/C5RA26509F](https://doi.org/10.1039/C5RA26509F)
- [66] Hu, K.; Tao, L.; Liu, D.; Huo, J.; Wang, S. Sulfur–doped Fe/N/C nanosheets as highly efficient electrocatalysts for oxygen reduction reaction. *ACS Appl. Mater. Interfaces* **2016**, *8*, 19379–19385.
[DOI:10.1021/acsami.6b02078](https://doi.org/10.1021/acsami.6b02078)
- [67] Deng, Y.; Xie, Y.; Zou, K.; Ji, X. Review on recent advances in nitrogen–doped carbons: preparations and applications in supercapacitors. *J. Mater. Chem. A*, **2016**, *4*, 1144–1173.
[DOI:10.1039/C5TA08620E](https://doi.org/10.1039/C5TA08620E)

- [68] Li, J.; Shen, B.; Hong, Z.; Lin, B.; Gao, B.; Chen, Y. A facile approach to synthesize novel oxygen-doped g-C₃N₄ with superior visible-light photoreactivity. *Chem. Commun.* **2012**, *48*, 12017–12019.
DOI:10.1039/C2CC35862J
- [69] Fujita, S.I.; Watanabe, H.; Katagiri, A.; Yoshida, H.; Arai, M. Nitrogen and oxygen-doped metal-free carbon catalysts for chemoselective transfer hydrogenation of nitrobenzene, styrene, and 3-nitrostyrene with hydrazine. *Mol. Catal. A Chem.* **2014**, *393*, 257–262.
DOI:10.1016/j.molcata.2014.06.021
- [70] Sun, X.; Song, P.; Chen, T.; Liu, J.; Xu, W. Fluorine-doped BP 2000: Highly efficient metal-free electrocatalysts for acidic oxygen reduction reaction with superlow H₂O₂ yield. *Chem. Commun.* **2013**, *49*, 10296–10298.
DOI:10.1039/C3CC45480K
- [71] Gumpu, M.B.; Mani, G.K.; Nesakumar, N.; Kulandaisamy, A.J.; Babu, K.J.; Rayappan, J.B.B. Electrocatalytic nanocauliflower structured fluorine doped CdO thin film as a potential arsenic sensor. *Sens. Actuators B Chem.* **2016**, *234*, 426–434.
DOI:10.1016/j.snb.2016.05.011
- [72] Peera, S.G.; Arunchander, A.; Sahu, A.K. Cumulative effect of transition metals on nitrogen and fluorine co-doped graphite nanofibers: an efficient and highly durable non-precious metal catalyst for the oxygen reduction reaction. *Nanoscale* **2016**, *8*, 14650–14664.
DOI:10.1039/C6NR02263D
- [73] Xie, J.; Zhao, X.; Wu, M.; Li, Q.; Wang, Y.; Yao, J. Metal-free fluorine-doped carbon electrocatalyst for CO₂ reduction outcompeting hydrogen evolution. *Angew. Chem. Int. Ed.* **2018**, *130*, 9788–9792.
DOI:10.1002/anie.201802055
- [74] Ping, K.; Alam, M.; Käärik, M.; Leis, J.; Kongi, N.; Järving, I.; Starkov, P. Surveying iron–organic framework TAL–1-derived materials in ligandless heterogeneous oxidative catalytic transformations of alkylarenes. *Synlett* **2019**, *30*, 1536–1540.
DOI:10.1055/s-0037-1611877
- [75] Malko, D.; Kucernak, A.; Lopes, T. *In situ* electrochemical quantification of active sites in Fe–N/C non-precious metal catalysts. *Nat. Commun.* **2016**, *7*, 13285.
DOI:10.1038/ncomms13285
- [76] Wan, X.; Wang, H.; Yu, H.; Peng, F. Highly uniform and monodisperse carbon nanospheres enriched with cobalt–nitrogen active sites as a potential oxygen reduction electrocatalyst. *J. Power Sources* **2017**, *346*, 80–88.
DOI:10.1016/j.jpowsour.2017.02.030
- [77] Varnell, J.A.; Edmund, C.M.; Schulz, C.E.; Fister, T.T.; Haasch, R.T.; Timoshenko, J.; Frenkel, A.I.; Gewirth, A.A. Identification of carbon-encapsulated iron nanoparticles as active species in non-precious metal oxygen reduction catalysts. *Nat. Commun.* **2016**, *7*, 12582.
DOI:10.1038/ncomms12582
- [78] Ping, K.; Alam, M.; Brashinsky, A.; Bhadoria, R.; Mihkli, V.; Mere, A.; Vlassov, S.; Kook, M.; Rähn, M.; Sammelselg, V.; Aruväli, J.; Tammeveski, K.; Kongi, N.; Starkov, P. Fused hybrid linkers for metal–organic framework-derived bifunctional oxygen electrocatalysts. *ACS Appl. Energy Mater.* **2020**, *3*, 152–157.
DOI:10.1021/acsaem.9b02039

- [79] H. B. Wu, X. W. Lou. Metal-organic frameworks and their derived materials for electrochemical energy storage and conversion: promises and challenges. *Sci. Adv.* **2017**, *3*, eaap9252.
DOI:10.1126/sciadv.aap9252
- [80] Diercks, C.S.; Kalmutzki, M.J.; Diercks, D.J.; Yaghi, O.M. Conceptual advances from Werner complexes to metal–organic frameworks. *ACS Cent. Sci.* **2018**, *4*, 1457–1464.
DOI:10.1021/acscentsci.8b00677
- [81] Zhao, S.; Yin, H.; Du, L.; He, L.; Zhao, K.; Chang, L.; Yin, G.; Zhao, H.; Liu, S.; Tang, Z. Carbonized nanoscale metal–organic frameworks as high performance electrocatalyst for oxygen reduction reaction. *ACS Nano* **2014**, *8*, 12660–12668.
DOI:10.1021/nn505582e
- [82] Xia, B.Y.; Yan, Y.; Li, N.; Wu, H.B.; Lou, X.W.; Wang, X. A metal–organic framework-derived bifunctional oxygen electrocatalyst. *Nat. Energy* **2016**, *1*, 15006.
DOI:10.1038/nenergy.2015.6
- [83] Zhao, R.; Liang, Z.; Gao, S.; Yang, C.; Zhu, B.; Zhao, J.; Qu, C.; Zou, R.; Xu, Q. Puffing up energetic metal–organic frameworks to large carbon networks with hierarchical porosity and atomically dispersed metal sites. *Angew. Chem. Int. Ed.* **2019**, *58*, 1975–1979.
DOI:10.1002/anie.201811126
- [84] Shinde, S.S.; Lee, C.H.; Jung, J.-Y.; Wagh, N.K.; Kim, S.-H.; Kim, D.-H.; Lin, C.; Lee, S.U.; Lee, J.H. Unveiling dual-linkage 3D hexaminobenzene metal–organic frameworks towards long-lasting advanced reversible Zn–air batteries. *Energy Environ. Sci.* **2019**, *12*, 727–738.
DOI:10.1039/C8EE02679C
- [85] Jasinski, R. A new fuel cell cathode catalyst. *Nature* **1964**, *201*, 1212–1213.
DOI:10.1038/2011212a0
- [86] Kong, D.; Gao, Y.; Xiao, Z.; Xu, X.; Li, X.; Zhi, L. Rational design of carbon-rich materials for energy storage and conversion. *Adv. Mater.* **2019**, *31*, 1804973.
DOI:10.1002/adma.201804973
- [87] Bhadoria, R. Design of heterobivalent molecules and their applications in chemical biology and materials science. Tallinn University of Technology, **2020**.
<https://digikogu.taltech.ee/en/Item/1b7c1e2b-17e6-472e-a643-1e5cb9ea3929>
- [88] Hu, Y.; Jensen, J.O.; Zhang, W.; Cleemann, L.N.; Xing, W.; Bjerrum, N.J.; Li, Q. Hollow spheres of iron carbide nanoparticles encased in graphitic layers as oxygen reduction catalysts. *Angew. Chem. Int. Ed.* **2014**, *53*, (2014) 3675–3679.
DOI:10.1002/anie.201400358
- [89] Yang, W.; Liu, X.; Yue, X.; Jia, J.; Guo, S. Bamboo-like carbon nanotube/Fe₃C nanoparticle hybrids and their highly efficient catalysis for oxygen reduction. *J. Am. Chem. Soc.* **2015**, *137*, 1436–1439.
DOI:10.1021/ja5129132
- [90] Kim, J.H.; Sa, Y.J.; Jeong, H.Y.; Joo, S.H. Roles of Fe–N_x and Fe–Fe₃C@C species in Fe–N/C electrocatalysts for oxygen reduction reaction. *ACS Appl. Mater. Interfaces* **2017**, *9*, 9567–9575.
DOI:10.1021/acsaami.6b13417
- [91] Sun, T.; Jiang, Y.; Wu, Q.; Du, L.; Zhang, Z.; Yang, L.; Wang, X.; Hu, Z. Is iron nitride or carbide highly active for oxygen reduction reaction in acidic medium? *Catal. Sci. Technol.* **2017**, *7*, 51–55.
DOI:10.1039/c6cy01921h

- [92] Hu, E.; Yu, X.-Y.; Chen, F.; Wu, Y.; Hu, Y.; Lou, X. W. Graphene layers-wrapped Fe/Fe₅C₂ nanoparticles supported on N-doped graphene nanosheets for highly efficient oxygen reduction. *Adv. Energy Mater.* **2018**, *8*, 1702476.
DOI:10.1002/aenm.201702476
- [93] Yang, S.; Jiang, J.-T.; Xu, C.-Y.; Wang, Y.; Xu, Y.-Y.; Cao, L.; Zhen, L. Synthesis of Zn(II)-doped magnetite leaf-like nanorings for efficient electromagnetic wave absorption. *Sci. Rep.* **2017**, *7*, 45480.
DOI:10.1038/srep45480
- [94] Huang, Z.-F.; Wang, J.; Peng, Y.; Jung, C.-Y.; Fisher, A.; Wang, X. Design of efficient bifunctional oxygen reduction/evolution electrocatalyst: recent advances and perspectives. *Adv. Energy Mater.* **2017**, *7*, 1700544.
DOI:10.1002/aenm.201700544
- [95] Filippidi, E.; Cristiani, T.R.; Eisenbach, C.D.; Waite, J.H.; Israelachvili, J.N.; Ahn, B.K.; Valentine, M.T. Toughening elastomers using mussel-inspired iron-catechol complexes. *Science* **2017**, *358*, 502–505.
DOI:10.1126/science.aao0350
- [96] Sarapuu, A.; Kibena-Pöldsepp, E.; Borghei, M.; Tammevski, K. Electrocatalysis of oxygen reduction on heteroatom-doped nanocarbons and transition metal–nitrogen–carbon catalysts for alkaline membrane fuel cells. *J. Mater. Chem. A* **2018**, *6*, 776–804.
DOI:10.1039/C7TA08690C
- [97] Shao, M.; Chang, Q.; Dodelet, J.-P.; Chenitz, R. Recent advances in electrocatalysts for oxygen reduction reaction. *Chem. Rev.* **2016**, *116*, 3594–3657.
DOI:10.1021/acs.chemrev.5b00462
- [98] Guo, D.; Shibuya, R.; Akiba, C.; Saji, S.; Kondo, T.; Nakamura, J. Active sites of nitrogen-doped carbon materials for oxygen reduction reaction clarified using model catalysts. *Science* **2016**, *351*, 361–365.
DOI:10.1126/science.aad0832
- [99] Kabir, S.; Artyushkova, K.; Serov, A.; Atanassov, P. Role of nitrogen moieties in N-doped 3D-graphene nanosheets for oxygen electroreduction in acidic and alkaline media. *ACS Appl. Mater. Interfaces* **2018**, *10*, 11623–11632.
DOI:10.1021/acsami.7b18651
- [100] Jiang, R.; Li, L.; Sheng, T.; Hu, G.; Chen, Y.; Wang, L. Edge-site engineering of atomically dispersed Fe–N₄ by selective C–N bond cleavage for enhanced oxygen reduction reaction activities. *J. Am. Chem. Soc.* **2018**, *140*, 11594–11598.
DOI:10.1021/jacs.8b07294
- [101] Ratso, S.; Ranjbar Sahraie, N.; Sougrati, M. T.; Käärik, M.; Kook, M.; Saar, R.; Paiste, P.; Jia, Q.; Leis, J.; Mukerjee, S.; Jaouen, F.; Tammeveski, K. Synthesis of highly-active Fe–N–C catalysts for PEMFC with carbide-derived carbons. *J. Mater. Chem. A* **2018**, *6*, 14663–14674.
DOI:10.1039/c8ta02325e
- [102] Liu, X.-H.; Hu, W.-L.; Jiang, W.-J.; Yang, Y.-W.; Niu, S.; Sun, B.; Wu, J.; Hu, J.-S. Well-defined metal–O₆ in metal–catecholates as a novel active site for oxygen electroreduction. *ACS Appl. Mater. Interfaces* **2017**, *9*, 28473–28477.
DOI:10.1021/acsami.7b07410

- [103] Zhong, H.; Ly, K. H.; Wang, M.; Krupskaya, Y.; Han, X.; Zhang, J.; Zhang, J.; Kataev, V.; Büchner, B.; Weidinger, I.M.; Kaskel, S.; Liu, P.; Chen, M.; Dong, R.; Feng, X. A phthalocyanine-based layered two-dimensional conjugated metal-organic framework as a highly efficient electrocatalyst for the oxygen reduction reaction. *Angew. Chem. Int. Ed.* **2019**, *58*, 10677–10682.
[DOI:10.1021/anie.201907002](https://doi.org/10.1021/anie.201907002)
- [104] Miner, E.M.; Gul, S.; Ricke, N.D.; Pastor, E.; Yano, J.; Yachandra, V.K.; van Voorhis, T.; Dincă, M. Mechanistic evidence for ligand-centered electrocatalytic oxygen reduction with the conductive MOF Ni₃(hexaiminotriphenylene)₂. *ACS Catal.* **2017**, *7*, 7726–7731.
[DOI:10.1021/acscatal.7b02647](https://doi.org/10.1021/acscatal.7b02647)
- [105] Miner, E.M.; Wang, L.; Dincă, M. Modular O₂ electroreduction activity in triphenylene-based metal–organic frameworks. *Chem. Sci.* **2018**, *9*, 6289–6291.
[DOI:10.1039/C8SC02049C](https://doi.org/10.1039/C8SC02049C)
- [106] Vanjari, R.; Singh, K.N. Utilization of methylenes as versatile building blocks in organic synthesis. *Chem. Soc. Rev.* **2015**, *44*, 8062–8096.
[DOI:10.1039/C5CS00003C](https://doi.org/10.1039/C5CS00003C)
- [107] Nakanishi, M.; Bolm, C. Iron-catalyzed benzylic oxidation with aqueous tert-butyl hydroperoxide. *Adv. Synth. Catal.* **2007**, *349*, 861–864.
[DOI:10.1002/adsc.200600553](https://doi.org/10.1002/adsc.200600553)
- [108] Zhang, S.; Guo, L.-N.; Wang, H.; Duan, X.-H. Bu₄Ni-catalyzed decarboxylative acyloxylation of an sp³ C–H bond adjacent to a heteroatom with α-oxocarboxylic acids. *Org. Biomol. Chem.* **2013**, *11*, 4308–4311.
[DOI:10.1039/C3OB40748A](https://doi.org/10.1039/C3OB40748A)
- [109] Barton, D.H.R.; Le Gloahec, V.N. The radical chemistry of *t*-butyl hydroperoxide (TBHP)—Part—further studies on hydrocarbon activation. *Tetrahedron* **1998**, *54*, 15457–15468.
[DOI:10.1016/S0040-4020\(98\)00974-0](https://doi.org/10.1016/S0040-4020(98)00974-0)
- [110] Liao, P.Q.; Shen, J.Q.; Zhang, J.P. Metal–organic frameworks for electrocatalysis. *Coord. Chem. Rev.* **2018**, *373*, 22–48.
[DOI:10.1016/j.ccr.2017.09.001](https://doi.org/10.1016/j.ccr.2017.09.001)
- [111] Huang, X.-C.; Lin, Y.-Y.; Zhang, J.-P.; Chen, X.-M. Ligand-directed strategy for zeolite-type metal-organic frameworks: Zinc(II) imidazoles with unusual zeolitic topologies. *Angew. Chem. Int. Ed.* **2006**, *45*, 1557–1559.
[DOI:10.1002/anie.200503778](https://doi.org/10.1002/anie.200503778)
- [112] Yang, F.; Mu, H.; Wang, C.; Xiang, L.; Yao, K. X.; Liu, L.; Yang, Y.; Han, Y.; Li, Y.; Pan, Y. Morphological map of ZIF-8 crystals with five distinctive shapes: Feature of filler in mixed-matrix membranes on C₃H₆/C₃H₈ separation. *Chem. Mater.* **2018**, *30*, 3467–3473.
[DOI:10.1021/acs.chemmater.8b01073](https://doi.org/10.1021/acs.chemmater.8b01073)
- [113] Ma, M.; Noei, H.; Mienert, B.; Niesel, J.; Bill, E.; Muhler, M.; Fischer, R.A.; Wang, Y.; Schatzschneider, U.; Metzler-Nolte, N. Iron metal–organic frameworks MIL-88B and NH₂-MIL-88B for the loading and delivery of the gasotransmitter carbon monoxide. *Chem. Eur. J.* **2013**, *19*, 6785–6790.
[DOI:10.1002/chem.201201743](https://doi.org/10.1002/chem.201201743)

- [114] Gándara, F.; Uribe-Romo, F.J.; Britt, D.K.; Furukawa, H.; Lei, L.; Cheng R.; Duan, X.; O’Keeffe, M.; Yaghi, O.M. Porous, conductive metal-triazolates and their structural elucidation by the charge-flipping method. *Chem. Eur. J.* **2012**, *18*, 10595–10601. DOI:10.1002/chem.201103433
- [115] Bennett, T.D.; Cheetham, A.K. Amorphous metal–organic frameworks. *Acc. Chem. Res.* **2014**, *47*, 5, 1555–1562. DOI:10.1021/ar5000314
- [116] Bennett, T.D.; Horike, S. Liquid, glass and amorphous solid states of coordination polymers and metal–organic frameworks. *Nat. Rev. Mater.* **2018**, *3*, 431–440. DOI:10.1038/s41578-018-0054-3
- [117] Ping, K.; Alam, M.; Kahnert, S.R.; Bhadoria, R.; Mere, A.; Mikli, V.; Käärrik, M.; Aruväli, J.; Paiste, P.; Kikas, A.; Kisand, V.; Järving, I.; Leis, J.; Tammeveski, K.; Kongi, N.; Starkov, P. Multi-purpose chemo- and electrocatalyst material from an amorphous cobalt metal–organic framework. *Manuscript submitted*.
- [118] Li, Y.; Jie, S.; Li, K.; Liu, Z. Synthesis of efficient Co and N co-doped carbon catalysts with high surface areas for selective oxidation of ethylbenzene. *New J. Chem.* **2018**, *42*, 12677–12683. DOI:10.1039/C8NJ01402G
- [119] Gilman, H.; Gorsich, R.G. The direct preparation of benzyllithium. *J. Am. Chem. Soc.* **1955**, *77*, 3134–3135. DOI:10.1021/ja01616a064
- [120] Aitken, R.A.; Hodgson, P.K.G.; Morrison, J.J.; Oyewale, A.O. Flash vacuum pyrolysis over magnesium. Part 1. Pyrolysis of benzylic, other aryl/alkyl and aliphatic halides. *J. Chem. Soc., Perkin Trans. 1* **2002**, *3*, 402–415. DOI:10.1039/b108663d
- [121] Ginah, F.O.; Donovan Jr., T.A.; Suchan, S.D.; Pfennig, D.R.; Ebert, G.W. Homocoupling of alkyl halides and cyclization of alpha,omega-dihaloalkanes via activated copper. *J. Org. Chem.* **1990**, *55*, 584–589. DOI:10.1021/jo00289a037
- [122] Inaba, S.-i.; Matsumoto, H.; Rieke, R.D. Metallic nickel as a reagent for the coupling of aromatic and benzylic halides. *Tetrahedron Lett.* **1982**, *23*, 4215–4216. DOI:10.1016/S0040-4039(00)88707-9
- [123] Levin, V.V.; Agababyan, D.P.; Struchkova, M.I.; Dilman, A.D. Dimerization of benzyl and allyl halides via photoredox-mediated disproportionation of organozinc reagents. *Synthesis* **2018**, *50*, 2930–2935. DOI:10.1055/s-0036-1591583
- [124] Park, G.; Yi, S.Y.; Jung, J.; Cho, E.J.; You, Y. Mechanism and applications of the photoredox catalytic coupling of benzyl bromides. *Chem. Eur. J.* **2016**, *22*, 17790–17799. DOI:10.1002/chem.201603517
- [125] Sato, K.; Inoue, Y.; Mori, T.; Sakaue, A.; Tarui, A.; Omote, M.; Kumadaki, I.; Ando, A. Csp³–Csp³ homocoupling reaction of benzyl halides catalyzed by rhodium. *Org. Lett.* **2014**, *16*, 3756–3759. DOI:10.1021/ol501619w
- [126] Carlucci, L.; Ciani, G.; Proserpio, D.M.; Mitina, T.G.; Blatov, V.A. Entangled two-dimensional coordination networks: A general survey. *Chem. Rev.* **2014**, *114*, 7557–7580. DOI:10.1021/cr500150m

- [127] Volkova, I.B.; Bogdanova, M.V. Petrology and genesis of Karelian shungite – high rank coal. *Int. J. Coal Geol.* **1986**, *4*, 369–379.
[DOI:10.1016/0166-5162\(86\)90011-X](https://doi.org/10.1016/0166-5162(86)90011-X)
- [128] Melezhik, V.A.; Filippov, M.M.; Romashkin, A.E. A giant Palaeoproterozoic deposit of shungite in NW Russia: Genesis and practical applications. *Ore Geol. Rev.* **2004**, *24*, 135–154.
[DOI:10.1016/j.oregeorev.2003.08.003](https://doi.org/10.1016/j.oregeorev.2003.08.003)
- [129] Gusmão, R.; Sofer, Z.; Bouša, D.; Pumera, M. Synergetic metals on carbocatalyst shungite. *Chem. Eur. J.* **2017**, *23*, 18232–18238.
[DOI:10.1002/chem.201703974](https://doi.org/10.1002/chem.201703974)
- [130] Tamburri, E.; Carcione, R.; Politi, S.; Angjellari, M.; Lazzarini, L.; Vanzetti, L.E.; Macis, S.; Pepponi, G.; Terranova, M.L. Shungite carbon as unexpected natural source of few-layer graphene platelets in a low oxidation state. *Inorg. Chem.* **2018**, *57*, 8487–8498.
[DOI:10.1021/acs.inorgchem.8b01164](https://doi.org/10.1021/acs.inorgchem.8b01164)
- [131] Krasnovyd, S.V.; Konchits, A.A.; Shanina, B.D.; Valakh, M.Y.; Yanchuk, I.B.; Yukhymchuk, V.O.; Yefanov, A.V.; Skoryk, M.A. Local structure and paramagnetic properties of the nanostructured carbonaceous material shungite. *Nanoscale Res Lett.* **2015**, *10*, 78.
[DOI:10.1186/s11671-015-0767-9](https://doi.org/10.1186/s11671-015-0767-9)
- [132] Gottlieb, H. E.; Kotlyar, V.; Nudelman, A. NMR chemical shifts of common laboratory solvents as trace impurities. *J. Org. Chem.* **1997**, *62*, 7512–7515.
[DOI:10.1021/jo971176v](https://doi.org/10.1021/jo971176v)
- [133] Asanuma, Y.; Mori, H.; Takahashi, R.; Nishihara, Y. Vinylene-bridged difluorobenzo [c][1, 2, 5]-thiadiazole (FBTzE): A new electron-deficient building block for high-performance semiconducting polymers in organic electronics. *J. Mater. Chem. C* **2019**, *7*, 905–916.
[DOI:10.1039/C8TC05764H](https://doi.org/10.1039/C8TC05764H)
- [134] Young, J. A. Benzoic acid. *J. Chem. Educ.* **2006**, *83*, 697.
[DOI:10.1021/ed083p697](https://doi.org/10.1021/ed083p697)
- [135] Crisostomo, C.; Crestani, M. G; Garcia, J. A. The catalytic hydration of 1,2-, 1,3- and 1,4-dicyanobenzenes using nickel(0) catalysts. *J. Mol. Catal.* **2007**, *266*, 139–148.
[DOI:10.1016/j.molcata.2006.10.054](https://doi.org/10.1016/j.molcata.2006.10.054)
- [136] Schmidt, A. K.; Stark, C. B.W. TPAP-catalyzed direct oxidation of primary alcohols to carboxylic acids through stabilized aldehyde hydrates. *Org. Lett.* **2011**, *13*, 4164–4167.
[DOI:10.1021/ol2014335](https://doi.org/10.1021/ol2014335)
- [137] Schorger, A. W. The action of aluminum chloride on cymene. *J. Am. Chem. Soc.* **1917**, *39*, 2671–2679.
[DOI:10.1021/ja02257a019](https://doi.org/10.1021/ja02257a019)
- [138] Yuan, Y.; Shi, X.; Liu, W. Transition-metal-free, chemoselective aerobic oxidations of sulfides and alcohols with potassium nitrate and pyridinium tribromide or bromine. *Synlett* **2011**, *4*, 559–564.
[DOI:10.1055/s-0030-1259516](https://doi.org/10.1055/s-0030-1259516)
- [139] Yang, D.; Yang, H.; Fu, H. Copper-catalyzed aerobic oxidative synthesis of aromatic carboxylic acids. *Chem. Commun.* **2011**, *47*, 2348–2350.
[DOI:10.1039/C0CC04319B](https://doi.org/10.1039/C0CC04319B)

Acknowledgements

I would like to thank my supervisor Dr. Pavel Starkov for his valuable guidance and enthusiastic support during this research work.

I would also like to thank my research colleagues Mahboob Alam, Rohit Bhadoria, Sean Ray Kahnert, Christer Lohk, Johanna Ley and other lab members for their support during my PhD work.

I would also like to thank all the technical staffs and other staff members at the Department.

I am deeply grateful to my family members for their constant encouragement, blessings, and support throughout my research work.

Funding from the Estonian Research Council (Starting Grant PUT1290), Tallinn University of Technology (Young Investigator Grant B62) and SA Archimedes (the Estonian Smart Specialization PhD Fellowship; the Graduate School of Biomedicine and Biotechnology #ASTRA 2014-2020.4.01.16-032) is acknowledged.

Abstract

Rational design of carbonaceous MOF-based materials for chemo- and electrocatalytic applications

This thesis focuses on rational design of novel metal–organic framework (MOF) derived materials, which incorporate non-precious metals. Their catalytic activity and stability was finetuned by altering the combination of organic ligands, metal sources and fabrication conditions for applications in heterogeneous and electrocatalysis.

Development of universal catalyst materials is the cornerstone of sustainable technologies. The lock-and-key relationship between one specific catalyst and one specific process is widely relied upon; however, well-optimized heterogeneous catalysts can eventually be used for various applications. In my PhD work, I have developed a series of novel iron and cobalt-based materials derived from polycrystalline and amorphous metal-organic frameworks, respectively. I have applied these materials as universal catalysts (i) in organic transformations, namely, oxidation and benzylic homocoupling reactions; and (ii) in various electrocatalytic reactions that are directly linked to energy conversion and storage devices, specifically, oxygen reduction reaction (ORR), oxygen evolution reaction (OER), and hydrogen evolution reaction (HER).

M–N–C materials, which are based on non-precious metals (Fe, Ni, Co, Mn, Cu), are gaining popularity in both heterogeneous and electrocatalysis. Their fabrication strategies are quite similar, albeit acid etching is omitted in the former case. To date, the choice of ligands that were applied has remained rather limited and relied on the use of 1,10-phenanthroline, porphyrins, phthalocyanines and well-established MOFs (ZIF–8 and ZIF–67). In the future, it might be more insightful to explore a wider range of ligands and metal combinations to improve the stability and the overall performance of final catalysts. This will also be essential for getting more sophisticated computational models and will eventually result in the uptake of M–N–C materials for the use in large scale applications. This, however, will require a deeper understanding of deactivation mechanisms of the catalysts in-hand so as to reduce their loadings, obtain their environmental toxicity profiles and ensure their sustainability in the long term.

In this work, I go on to prepare and screen a new class of organic ligands used as precursors for the formation of multifunctional materials. Namely, these include substitutions and alterations at different positions around the benzimidazole core. Importantly, I also include formation of symmetrical dimers that were obtained using a $\text{Ti}(\text{OPr})_4$ -mediated condensation reaction. By having used simple, albeit substituted benzimidazoles, I have extended the possibilities of finetuning our materials without relying on more complex chemical precursors, e.g. porphyrins and phthalocyanines.

Within this work I have also introduced a new carbon support. It is based on shungite, a raw material, which is carbon-rich and electroconductive. Unlike many other alternatives, it is inexpensive. I have shown that it can be used as a carbon support for highly efficient bifunctional electrode materials.

Chapter 1 gives a concise overview on preparation and characterization of novel M–N–C materials. Chapter 2 (Publications I, II, and IV) describes fabrication and applications of novel iron-based materials derived from a set of 5,6-substituted benzimidazoles in ORR, OER and oxidative transformations of alkylarenes. In Chapter 3 (Publications III and IV), the best preforming ligand was used to prepare a series of cobalt

based materials, which were then used to identify an optimal one that can simultaneously be used both as chemo- and electrocatalyst. In Chapter 4 (Publication V), shungite, a carbon-rich raw material is introduced as a new carbon support. Chapter 5 includes experimental details.

Lühikokkuvõte

Süsinikurikastel, metall–orgaanilistel võrestikel põhinevate materjalide disain ja nende kasutuselevõtt kemo- ja elektrokatalüütilistes rakendustes

Antud doktoritöö keskendub süsinikurikastel metall–orgaaniliste võrestike baasil arendatud funktsionaalsete materjalide disainimisele, mis ei sisalda väärismetalle. Nende katalüütiline aktiivsus ja stabiilsus on optimeeritud, kasutades erinevaid orgaanilisi ligande, metalli-allikaid ja valmistamistehnikaid selleks, et leida katalüsaatoreid heterogeensete ja elektrokatalüütiliste rakenduste jaoks.

Jätkusuutlikud tehnoloogiad toetuvad universaalsete katalüsaatormaterjalide väljatöötamisele. Kuigi tavaliselt on pööratud palju tähelepanu ühe katalüsaatori materjali väljatöötamisele ühe konkreetse rakenduse jaoks, tuleb siiski leida viis selliste katalüsaatorite väljatöötamiseks, mida saab kasutada samaaegselt nii heterogeensete kui elektrokatalüütiliste protsesside jaoks. Selles töös oleme uurinud raua- ja koobaltipõhiseid materjale, mis on saadud polükristallilistest ja amorfsetest metall–orgaanilistest võrestikest, mitmesuguste rakenduste jaoks. Oleme keskendunud orgaanilistele muundumistele, eelkõige alküülaareenide oksüdatiivsetele transformatsioonidele ja bensüülsidumisreaktsioonidele. Lisaks oleme näidanud, et meie innovaatilised katalüsaatormaterjalid on efektiivsed mitmetes elektrokatalüütilistes protsessides, mis on otseselt seotud energia muundamise ja salvestamise seadmetega, näiteks hapniku redutseerimise (ORR), hapniku evolutsiooni (OER) ja vesiniku evolutsiooni (HER) reaktsioonides. Samas oleme uurinud nende ainulaadsete multifunktsionaalsete materjalide stabiilsust ja ringlussevõetavust.

Antud töös valmistasin ja sõelusin uut klassi orgaanilisi ligande, mida kasutasin lähteainetena multifunktsionaalsete materjalide moodustamiseks. Nimelt hõlmavad need keemilisi asendusi ja muutusi erinevates asendites bensimidasooli ümber. Oluline fakt on see, et seeriasse on lisatud ka sümmeetrilisi dimeere, mis saadi $\text{Ti}(\text{OPr})_4$ -vahendatud kondensatsioonreaktsiooni abil. Kasutades lihtsaid, ehkki asendatud bensimidasoole, oleme laiendanud materjalide peenhäälestamise võimalusi, tuginemata märksa keerukamatele keemilistele lähteainetele, nt. porfüriinidele ja ftalotsüaniinidele.

Mitteväärismetallidel (eelkõige raual, niklil, koobaltil, mangaanil ja vasel) põhinevad niinimetatud metalli ja lämmastikuga dopeeritud süsinikmaterjalid (M–N–C) koguvad populaarsust nii heterogeenses kui elektrokatalüüsis. Nende valmistamisstrateegiad on üsna sarnased, ehkki happesöövitamine on heterogeensete katalüsaatorite väljatöötamisel tavaliselt ära jäetud. Siiani kasutatud ligandide valik on jäänud üsna piiratuks ning tugines 1,10-fenantroliini, porfüriinide, ftalotsüaniinide ja hästi tuntud MOF-ide (ZIF–8 ja ZIF–67) kasutamisele. Me näitasime, et tulevikus on mõistlikum uurida laiemat valikut ligande ja metallikombinatsioone selleks, et parandada lõppkatalüsaatorite stabiilsust ja jõudlust. Seda läheb vaja nii keerukamate arvutusmodelite väljatöötamiseks kui ka M–N–C materjalide kasutuselevõtuks suuremahulistes rakendustes. See aga nõuab põhjalikumat arusaama kuidas käesolevad katalüsaatorid deaktiveeruvad selleks, et vähendada nende kogust, saada nende keskkonnatoksilisuse profile ning tagada nende jätkusuutlikkust pikemas perspektiivis.

Selle töö raames olen tutvustanud ka uut süsinikkandjat Selleks on tooraine šungiit, mis on süsinikurikas ja on hea elektrijuht. Erinevalt paljudest muudest alternatiividest

on see odav. Olen näidanud, et seda saab kasutada süsinikkandjana ülitõhusate bifunktsionaalsete elektrootodimaterjalide jaoks.

Esimene peatükk sisaldab üldist ülevaadet M–N–C tüüpi materjalide valmistamisest ja iseloomustamisest. Teises peatükis (artiklid I, II ja IV) kirjeldatakse asendatud bensimidiasoolide baasil saadud uute rauapõhiste materjalide valmistamist ja kasutamist hapniku redutseerimise ja oksüdeerimise reaktsioonides ning alküülaareenide oksüdatiivsetes muundumistes. Kolmandas peatükis (artiklid III ja IV) arendati koobaltil põhinevaid materjale, mida kasutati multifunktsionaalse materjali tuvastamiseks ja mida saab samaaegselt kasutada nii heterogeense kui elektrokatalüsaatorina. Neljandas peatükis (artikkel V) tutvustatakse šungiiti, süsinikurikast toorainet, kui uut süsinikkandjat. Viies peatükk sisaldab eksperimentaalseid andmeid.

Appendix

Publication I

Ping, K.; Brashinsky, A.; Alam, M.; Bhadoria, R.; Mihkli, V.; Mere, A.; Vlassov, S.; Kook, M.; Rähn, M.; Sammelselg, V.; Aruväli, J.; Tammeveski, K.; Kongi, N.; Starkov, P.

Fused hybrid linkers for metal–organic framework-derived bifunctional oxygen electrocatalysts.

ACS Appl. Energy Mater. **2020**, 3, 152–157.

DOI:10.1021/acsaem.9b02039

Fused Hybrid Linkers for Metal–Organic Framework-Derived Bifunctional Oxygen Electrocatalysts

Kefeng Ping,[†] Alan Braschinsky,^{‡,§} Mahboob Alam,[†] Rohit Bhadoria,[†] Valdek Mikli,[§] Arvo Mere,[§] Jaan Aruväli,^{||} Päärn Paiste,^{||} Sergei Vlassov,[⊥] Mati Kook,[⊥] Mihkel Rähn,[⊥] Väino Sammelselg,^{‡,⊥} Kaido Tammeveski,[‡] Nadežda Kongi,^{*,‡} and Pavel Starkov^{*,†,||}

[†]Department of Chemistry and Biotechnology, Tallinn University of Technology, Tallinn 12618, Estonia

[‡]Institute of Chemistry, University of Tartu, Tartu 50411, Estonia

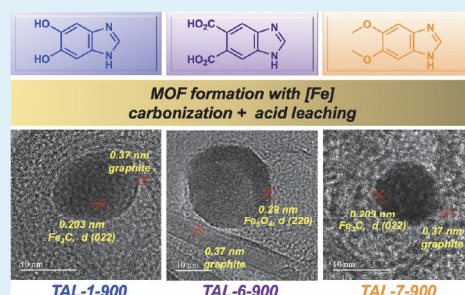
[§]Department of Materials and Environmental Technology, Tallinn University of Technology, Tallinn 19086, Estonia

^{||}Institute of Ecology and Earth Sciences, University of Tartu, Tartu 50411, Estonia

[⊥]Institute of Physics, University of Tartu, Tartu 50411, Estonia

Supporting Information

ABSTRACT: Preparation of electrocatalysts often relies on the use of multiple starting materials, with examples arising from a single precursor being less common. We have surveyed a series of heterobivalent scaffolds to identify an iron/benzimidazole-based metal–organic framework as a uniform starting material. By merging the catechol and imidazole units together, we get a direct entry into a highly efficient bifunctional oxygen electrocatalyst, which alleviates the need for dopants and modifying conditions. We demonstrate that by fine-tuning the chemical nature of an organic linker, one is able to modulate the electrochemical properties of a single precursor-derived electrocatalyst material.



KEYWORDS: bifunctional electrocatalyst, iron, oxygen reduction reaction, oxygen evolution reaction, renewable energy

Metal–organic frameworks (MOFs) are a great platform for designing and building novel materials with a foray into applications in energy storage and conversion, e.g., water splitting, fuel cells, and metal–air batteries.¹ MOFs incorporate both the metal centers and organic ligands, which serve as essential building blocks.² Hence, having an intrinsic ability to modify their combinations may lead to more efficient, modular electrocatalyst materials. The oxygen reduction reaction (ORR) electrocatalysts have been exemplary with different MOFs having been traditionally employed as carbon-scaffolds and nitrogen-rich sources.¹ However, they often necessitate using dopants to raise the overall performance of the underlying electrocatalyst.¹ To date, only a few MOF-derived materials were shown to serve as highly efficient electrocatalysts for ORR (Figure 1). Among them are iron-based MIL-88B-NH₂,³ cobalt-based ZIF-67,⁴ and bimetallic systems based on MET-6⁵ and hexaminobenzene.⁶

In the ORR domain, the use of organic constituents for fabrication of earth-abundant-metal-based electrocatalyst materials (M–N–C) dates back^{10,11} to the report of the first M–N–C catalyst, cobalt phthalocyanine (Figure 1A).¹² Since then, a number of complementary metal complexes (e.g., phthalocyanines,^{12–14} porphyrins,¹⁵ phenanthrolines,^{16–18} and ferrocene¹⁹) have been examined. Recent work indicated that

conductive MOFs such as M₃(HITP)₂^{7,20} and M₃(HHTP)₂^{20,21} may also serve as potential ORR catalysts. While such systems show low intrinsic activity, they have been used to demonstrate that organic constituents can participate in the electrochemical O₂ reduction through complementary ligand-centric mechanisms (Figure 1B).⁷

Herein, we introduce a new family of carbon-rich²² benzimidazole-based MOF precursors, which are equipped with additional functional groups to modulate their electronic and ligating properties (Figure 1C). We assess them as ORR and oxygen evolution reaction (OER)²³ catalyst materials to identify that monocatechol/imidazole fused hybrid **1** is the best performing ligand for fabricating effective bifunctional oxygen (ORR/OER, $\Delta E = 0.73$ V in 0.1 M KOH) electrocatalyst from an iron MOF-derived single-component precursor.

We envisaged building an Fe–N–C catalyst from a single MOF precursor by using designer ligands. While one would typically rely on multidirectional, symmetric structures based on porphyrins, phthalocyanines, and hexasubstituted triphenyl-

Received: October 15, 2019

Accepted: December 18, 2019

Published: December 18, 2019

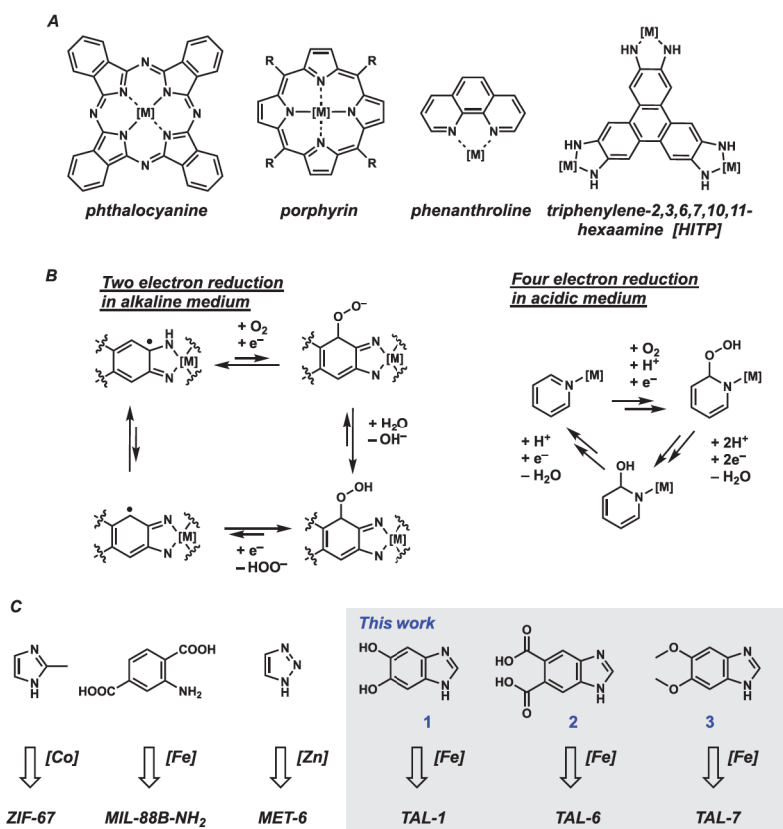


Figure 1. (A) Organic ligands complexed to a metal (M), widely used to prepare M–N–C cathode electrocatalyst materials for ORR. (B) Noninnocent ligand participation in the ORR.^{7–9} (C) Metal–organic frameworks used as single precursors for unsupported and nondoped ORR electrocatalysts.

lenes, we wished to focus on constructing several related but unique heterobivalent scaffolds. This would have given us means to see whether and how different organic ligands could affect the morphology and catalytic performance of the final electrocatalyst materials. To test this hypothesis, we prepared three MOFs as insoluble, polycrystalline powders TAL-1, TAL-6, and TAL-7 from iron chloride and 5,6-disubstituted 1H-benzo[d]imidazoles (1, R = OH; 2, R = COOH; 3, R = OCH₃) as ligands (Figure 2A). For TAL-1, we have tested various ratios of metal to linker (2:1, 1:1, 1:2); however, they did not significantly alter the chemical composition of the material obtained (Table S5). TAL materials were then subjected to carbonization at $T = 900^\circ\text{C}$ and acid leaching to give three electrocatalysts termed TAL-1-900, TAL-6-900, and TAL-7-900, respectively.

The structure and morphology of prepared electrocatalysts were examined by powder X-ray diffraction (PXRD), X-ray photoelectron spectroscopy (XPS), and high-resolution scanning and transmission electron microscopy (HRSEM and HRTEM) (Figure 2 and SI). The HRTEM images of TAL-1-900 and TAL-7-900 show dense α -Fe/Fe₃C@C nanocrystals, which are embedded into the structured, onion-like shells of carbon (Figure 2B). The characteristic layer

distance of the iron/iron carbide particles was 0.203 nm, and the spacing of the carbon shells was 0.371 nm; they remain constant after acid leaching.^{24–27} The presence of α -Fe in the Fe₃C@C nanocrystals in TAL-1-900 and TAL-7-900 was confirmed by PXRD (Figure 2C). TAL-6-900 material, however, incorporated iron oxide nanoparticles with a characteristic interplanar spacing of 0.29 nm corresponding to $d(220)$ of Fe₃O₄.²⁸ The XPS survey spectra show the presence of carbon, oxygen, nitrogen, and iron on the surface of the catalyst materials (Figure 2D, Figure S1, and Table S2). The deconvoluted N 1s region shows the presence of graphitic N (nitrogen), pyrrolic N, Fe–N_x, and pyridinic N species, which are all required for the high ORR/OER activity.^{10,11,23} The iron content at the surface of the materials was low (<0.41 at. %). This is consistent with a low total content of iron in the materials as measured by microwave plasma atomic emission spectroscopy (MP-AES) (Table S1, <3.6 wt %).

With the optimized materials in hand, we evaluated the electrochemical behavior of TAL-1-900, TAL-6-900, and TAL-7-900 using cyclic voltammetry (CV) in argon-saturated 0.1 M KOH solution at room temperature (Figure 3A). We compared electrochemical performance (catalyst loading 800 $\mu\text{g cm}^{-2}$; loading dependences are shown in Figure S6c)

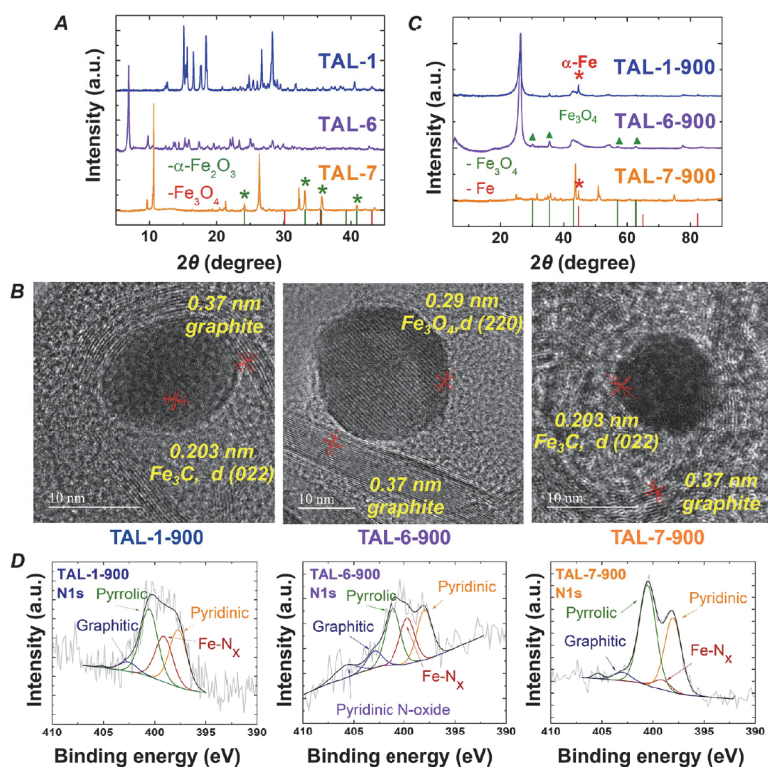


Figure 2. Physical and morphological characterization of TAL-X-900 precursors and derived catalyst materials. (A) PXRD patterns of TAL precursors. (B) HRTEM micrographs. (C) PXRD patterns of TAL-derived catalyst materials. (D) XPS core-level spectra in the N 1s region. Scale bars, 10 nm.

against the state-of-the-art commercial 20 wt % Pt/C catalyst (E-TEK; loading $20 \mu\text{g}_{\text{Pt}} \text{cm}^{-2}$).

The TAL electrocatalysts exhibited a symmetrical and rectangular CV profile without any characteristic redox features. The double-layer capacitance was larger than that of Pt/C, indicating that TAL-derived materials have a high electrochemically accessible surface area. The porosity of prepared catalysts was examined with the Brunauer–Emmett–Teller (BET) multipoint theory (Table S4). TAL-1-900 has slightly larger surface area, while the pore size distribution indicates that all the materials are mesoporous (Figure S3).

The rotating disk electrode (RDE) technique was employed to study the ORR kinetics of TAL-modified glassy carbon (GC) electrodes in O_2 -saturated 0.1 M KOH (Figure 3B). TAL-1-900 (R – OH) performed on par with 20 wt % Pt/C catalyst ($E_{\text{on}} = 1.01 \text{ V}$, $E_{1/2} = 0.87 \text{ V}$ vs $E_{\text{on}} = 1.01 \text{ V}$, $E_{1/2} = 0.85 \text{ V}$). While TAL-6-900 was less active than TAL-1-900, electrocatalyst TAL-7-900 showed good performance, albeit with a slight offset in the onset potential (E_{on}). Notably, when 1 and iron(III) chloride were premixed in DMF for 2 h, concentrated, and subjected to carbonization, the afforded material was not effective in the ORR tests (data not shown). Hence, the formation of corresponding MOFs is a prerequisite for fabrication of an active electrocatalyst. The effect of various catalyst loadings was explored. RDE measurements confirmed that increasing the catalyst loading from 0.1 to 0.8 mg cm^{-2}

significantly improved the ORR activity (Figure S4c): higher current densities and more positive half-wave potentials. For loadings $<0.4 \text{ mg cm}^{-2}$, the calculated electron count (n) was <4 .

Koutecký–Levich (K–L) plots (Figure 3C) were constructed from the RDE data (Figure 3D) and showed good linearity and parallelism for TAL-1-900. This behavior is typical for the first-order reaction kinetics with respect to the concentration of dissolved dioxygen. The number of electrons transferred per O_2 molecule (n) was calculated from the RDE data using the K–L equation. All TAL-derived electrocatalysts follow the desired four-electron transfer pathway ($n = 4$; the insets in Figure 3C and Figure S11), indicating that oxygen is reduced fully to water. Kinetic current densities were calculated using the K–L equation at 0.9 V and compared. TAL-1-900 exhibited the j_k value similar to that of Pt/C (2.0 vs 1.9 mA cm^{-2}).

In the kinetically controlled region of the ORR, the Tafel plots of TAL-1-900 overlapped with those of Pt/C, with two distinct regions present at different potential ranges (Figure 3E). TAL-1-900 catalyst had similar dual Tafel slopes in the low and high overpotential regions as Pt/C (-56 and -130 mV dec^{-1} vs -61 and -117 mV dec^{-1}). The Tafel slope value of -56 mV dec^{-1} for TAL-1-900 indicates that the rate-determining step in the ORR is the formation of adsorbed intermediates (OOH).

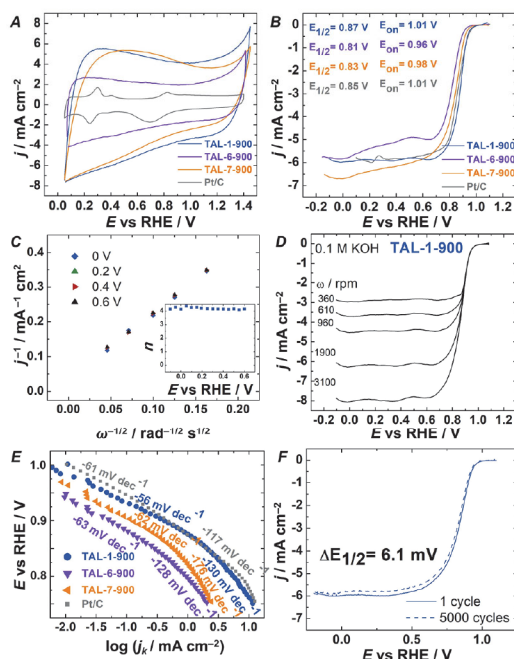


Figure 3. Electrochemical oxygen reduction on TAL materials in 0.1 M KOH. (A) Cyclic voltammograms of electrocatalyst-modified GC electrodes (under argon); $\nu = 50 \text{ mV s}^{-1}$. (B) RDE polarization curves for TAL and Pt/C-modified GC electrodes at 1900 rpm; $\nu = 10 \text{ mV s}^{-1}$. (C) Koutecky–Levich plots for O_2 reduction on TAL-1-900 modified GC electrode. Inset: number of electrons transferred per O_2 molecule. (D) RDE polarization data on oxygen reduction recorded at various rotation rates on TAL-1-900 modified GC electrode; $\nu = 10 \text{ mV s}^{-1}$. (E) Tafel plots for O_2 reduction on TAL and Pt/C catalysts. (F) Electrochemical stability test for TAL-1-900 (mid-range: 0.6–1.0 V).

After continuous cycling from 0.6 to 1.0 V vs RHE, electrocatalytic activity of TAL-1-900 remained at the same level without any change in the onset potential (Figure 3F). However, only a slight decrease in diffusion-limited current density was observed indicating that its porosity remains largely unaffected.

As TAL-1-900 showed excellent electrocatalytic behavior in the ORR tests, we wished to see how it performs in the oxygen evolution reaction (Figure 4). The materials with high bifunctional activity are used in metal–air batteries;²³ however, the active sites responsible for OER's high activity are different from the sites required for ORR.^{10,11,23} To assess the overall oxygen electrode activity (ΔE) of TAL electrocatalysts, the potential differences of OER at a current density of 10 mA cm^{-2} and of ORR at a current density of -3 mA cm^{-2} were calculated at electrode rotation rate of 1600 rpm. The bifunctional ORR/OER activity of TAL-1-900 ($\Delta E = 0.73 \text{ V}$; $E_{10} = 1.60 \text{ V @ } 10 \text{ mA cm}^{-2}$) is among the best reported to date (Table S7), while TAL-6-900 and TAL-7-900 were less active ($\Delta E = 0.83$ and 0.78 V , respectively).

TAL-1-900 has a Tafel slope of 84 mV dec^{-1} (Figure 4B), which is considerably smaller than those of TAL-6-900 (95 mV dec^{-1}), TAL-7-900 (112 mV dec^{-1}), RuO_2 (116 mV dec^{-1}),

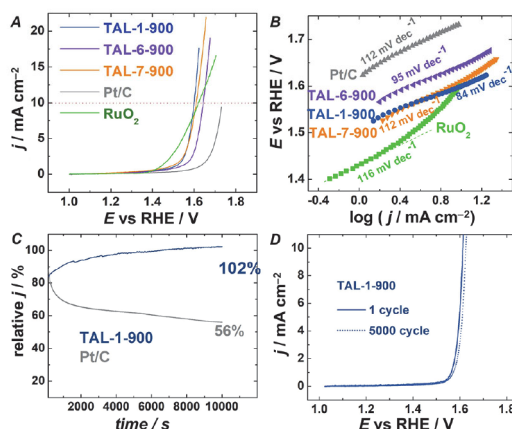


Figure 4. Electrochemical oxygen evolution on TAL materials in 0.1 M KOH. (A) LSV curves for TAL-modified GC electrodes, $\nu = 10 \text{ mV s}^{-1}$. (B) Tafel plots based on LSV curves. (C) Chronoamperometric response for TAL-1-900 and Pt/C recorded at applied potential of 1.6 V. (D) Electrochemical stability of TAL-1-900 after 5000 cycles.

and Pt/C (112 mV dec^{-1}), indicating faster OER kinetics. The durability of the TAL-1-900 catalyst was evaluated by a chronoamperometry test at an applied potential of 1.6 V (Figure 4C). The current density of the TAL-1-900 catalyst shows a slight increase during the testing time, demonstrating that the catalyst exhibits excellent durability toward OER. Electrocatalytic OER behavior also remained unchanged after continuous cycling of the TAL-1-900 electrode 5000 times in the potential range between 1.0 and 1.8 V vs RHE (Figure 4D).

The overall relationship TAL-1-900 > TAL-7-900 >> TAL-6-900 indicates that electron-rich precursors may boost the ORR/OER catalyst's activity. Our observation, however, may have several alternative explanations. These include rendering the activity of Fe– N_x sites and pyridinic, pyrrolic, and graphitic nitrogen;^{8–11} initiation of the ligand-centered $2e \times 2e$ pathway similar to the one proposed for HITP and HHTP ligands (Figure 1B);^{7,20,21} creation of catalytically active M– O_x ¹⁴ or mixed Fe– N_xO_x sites; the control of pore sizes and other structural aspects of the carbonized molecular meshwork. Notably, in the case of TAL-6-900, we observed formation of Fe_3O_4 but not Fe/ Fe_3C nanocrystals. While the M– N_x species are known to reduce dioxygen in the ORR via a direct reduction of oxygen to hydroxide (a $4e$ process), the less active metal-based particles (e.g., Fe/ Fe_3C ,^{24–27} Fe_2N ²⁶) do it in a stepwise $2e \times 2e$ manner (first, forming the peroxides and then decomposing them to water).^{10,11,24,25} This observation also suggests that the organic linker itself may modulate not only the rate of formation of nanocrystals embedded into carbon support but also their composition.

Interestingly, we observed an improvement in the TAL-1-900 vs TAL-7-900 performance. This may be attributed to the catechol unit itself because the iron–catechol complexation is sufficiently strong,²⁹ and several polycatechol-based covalent³⁰ and metal–organic frameworks were previously reported.^{14,20} Hence, employing catechol precursors may lead to increased conductivity of the final material and/or additional (electro)-

chemical contributions (e.g., enhanced carbonization or ligand-centered $2e \times 2e$ processes).

In summary, we have surveyed a series of carbon-rich, fused hybrid-type organic linkers to construct iron-based MOFs, which serve as direct precursors for efficient bifunctional electrocatalyst materials. This single simple-precursor strategy relied on carbonization of benzimidazole derivatives under a nonmodifying (N_2) atmosphere. The active Fe–N–C materials contained Fe–N_x sites, pyridinic nitrogen, and Fe/Fe₃C nanocrystals, except for TAL-6-900, which contained Fe₃O₄ and was much less active. Our results confirm that there is a link between the electronic and ligating properties of the initial organic ligands and the electrocatalytic properties of the final electrocatalyst materials. Translating this into practice will require further exploration of structure–activity relationships of chemically decorated carbon-rich precursors.

■ ASSOCIATED CONTENT

Supporting Information

The Supporting Information is available free of charge at <https://pubs.acs.org/doi/10.1021/acsaem.9b02039>.

Experimental details and characterization of catalyst materials (PXRD, XPS, MP-AES, HRTEM, HRSEM, BET, CHN analysis, and Raman), characterization of spent catalyst (PXRD, HRTEM), and preparation and characterization of ligands (NMR, IR) (PDF)

■ AUTHOR INFORMATION

Corresponding Authors

*E-mail: nadezda.kongi@ut.ee.

*E-mail: pavel.starkov@taltech.ee.

ORCID

Pavel Starkov: 0000-0003-1421-4731

Present Address

[#]A.B.: Department of Chemistry, Durham University, South Road, Durham DH1 3LE, United Kingdom.

Author Contributions

The manuscript was written through contributions of all authors. All authors have given approval to the final version of the manuscript.

Notes

The authors declare the following competing financial interest(s): K.P., K.T., N.K., P.S. are inventors on a related patent application owned by Tallinn University of Technology and the University of Tartu.

■ ACKNOWLEDGMENTS

This research was supported by Estonian Research Council Grant PUT1290 and TalTech Young Investigator Grant B62 (to P.S.); Estonian Research Council Grant PSG250 (to N.K.) and an Institutional Research Funding IUT20-16 of the Estonian Ministry for Education and Research and the Centre of Excellence TK141: Advanced materials and high-technology devices for energy recuperation systems from the EU ERDF program (both to K.T.). We thank COST Actions CA15135 and CA18224 members for helpful discussions and Dr. Maik Käärik and Dr. Jaan Leis for the BET measurements. TalTech (V.M.) and UT HRSEM (S.V.) facilities are supported by TK141, and IUT-T4 and PUT1689, respectively. TalTech (A.M.) and UT (J.A.) XRD facilities are supported by IUT19-4 and TK141. UT HRTEM (M.R., V.S.) and BET facilities are

supported by Institutional Research Funding IUT2-24 and IUT34-14 of the Estonian Ministry for Education and Research. K.P. acknowledges the Estonian Smart Specialization PhD Fellowship.

■ REFERENCES

- (1) Wu, H. B.; Lou, X. W. Metal-organic frameworks and their derived materials for electrochemical energy storage and conversion: promises and challenges. *Sci. Adv.* **2017**, *3*, No. eaap9252.
- (2) Diercks, C. S.; Kalmutzki, M. J.; Diercks, D. J.; Yaghi, O. M. Conceptual advances from Werner complexes to metal–organic frameworks. *ACS Cent. Sci.* **2018**, *4*, 1457–1464.
- (3) Zhao, S.; Yin, H.; Du, L.; He, L.; Zhao, K.; Chang, L.; Yin, G.; Zhao, H.; Liu, S.; Tang, Z. Carbonized nanoscale metal–organic frameworks as high performance electrocatalyst for oxygen reduction reaction. *ACS Nano* **2014**, *8*, 12660–12668.
- (4) Xia, B. Y.; Yan, Y.; Li, N.; Wu, H. B.; Lou, X. W.; Wang, X. A metal–organic framework-derived bifunctional oxygen electrocatalyst. *Nat. Energy* **2016**, *1*, 15006.
- (5) Zhao, R.; Liang, Z.; Gao, S.; Yang, C.; Zhu, B.; Zhao, J.; Qu, C.; Zou, R.; Xu, Q. Puffing up energetic metal–organic frameworks to large carbon networks with hierarchical porosity and atomically dispersed metal sites. *Angew. Chem., Int. Ed.* **2019**, *58*, 1975–1979.
- (6) Shinde, S. S.; Lee, C. H.; Jung, J.-Y.; Wagh, N. K.; Kim, S.-H.; Kim, D.-H.; Lin, C.; Lee, S. U.; Lee, J. H. Unveiling dual-linkage 3D hexaminobenzene metal–organic frameworks towards long-lasting advanced reversible Zn–air batteries. *Energy Environ. Sci.* **2019**, *12*, 727–738.
- (7) Miner, E. M.; Gul, S.; Ricke, N. D.; Pastor, E.; Yano, J.; Yachandra, V. K.; van Voorhis, T.; Dincă, M. Mechanistic evidence for ligand-centered electrocatalytic oxygen reduction with the conductive MOF Ni₃(hexaminotriphenylene)₂. *ACS Catal.* **2017**, *7*, 7726–7731.
- (8) Guo, D.; Shibuya, R.; Akiba, C.; Saji, S.; Kondo, T.; Nakamura, J. Active sites of nitrogen-doped carbon materials for oxygen reduction reaction clarified using model catalysts. *Science* **2016**, *351*, 361–365.
- (9) Kabir, S.; Artyushkova, K.; Serov, A.; Atanassov, P. Role of nitrogen moieties in N-doped 3D-graphene nanosheets for oxygen electroreduction in acidic and alkaline media. *ACS Appl. Mater. Interfaces* **2018**, *10*, 11623–11632.
- (10) Sarapu, A.; Kibena-Pöldsepp, E.; Borghei, M.; Tammeveski, K. Electrocatalysis of oxygen reduction on heteroatom-doped nanocarbons and transition metal–nitrogen–carbon catalysts for alkaline membrane fuel cells. *J. Mater. Chem. A* **2018**, *6*, 776–804.
- (11) Shao, M.; Chang, Q.; Dodelet, J.-P.; Chenitz, R. Recent advances in electrocatalysts for oxygen reduction reaction. *Chem. Rev.* **2016**, *116*, 3594–3657.
- (12) Jasinski, R. A new fuel cell cathode catalyst. *Nature* **1964**, *201*, 1212–1213.
- (13) Jiang, R.; Li, L.; Sheng, T.; Hu, G.; Chen, Y.; Wang, L. Edge-site engineering of atomically dispersed Fe–N₄ by selective C–N bond cleavage for enhanced oxygen reduction reaction activities. *J. Am. Chem. Soc.* **2018**, *140*, 11594–11598.
- (14) Zhong, H.; Ly, K. H.; Wang, M.; Krupskaya, Y.; Han, X.; Zhang, J.; Zhang, J.; Kataev, V.; Büchner, B.; Weidinger, I. M.; Kaskel, S.; Liu, P.; Chen, M.; Dong, R.; Feng, X. A phthalocyanine based layered two-dimensional conjugated metal–organic framework as a highly efficient electrocatalyst for the oxygen reduction reaction. *Angew. Chem., Int. Ed.* **2019**, *58*, 10677–10682.
- (15) Zhang, W.; Lai, W.; Cao, R. Energy-related small molecule activation reactions: oxygen reduction and hydrogen and oxygen evolution reactions catalyzed by porphyrin- and corrole-based systems. *Chem. Rev.* **2017**, *117*, 3717–3797.
- (16) Lefèvre, M.; Proietti, E.; Jaouen, F.; Dodelet, J.-P. Iron-based catalysts with improved oxygen reduction activity in polymer electrolyte fuel cells. *Science* **2009**, *324*, 71–74.
- (17) Strickland, K.; Miner, E.; Jia, Q.; Tylus, U.; Ramaswamy, N.; Liang, W.; Sougrati, M.; Jaouen, F.; Mukerjee, S. Highly active oxygen

reduction non-platinum group metal electrocatalyst without direct metal-nitrogen coordination. *Nat. Commun.* **2015**, *6*, 7343.

(18) Ratso, S.; Ranjbar Sahraie, N.; Sougrati, M. T.; Käärik, M.; Kook, M.; Saar, R.; Paiste, P.; Jia, Q.; Leis, J.; Mukerjee, S.; Jaouen, F.; Tammeveski, K. Synthesis of highly-active Fe–N–C catalysts for PEMFC with carbide-derived carbons. *J. Mater. Chem. A* **2018**, *6*, 14663–14674.

(19) Hu, Y.; Jensen, J. O.; Zhang, W.; Cleemann, L. N.; Xing, W.; Bjerrum, N. J.; Li, Q. Hollow spheres of iron carbide nanoparticles encased in graphitic layers as oxygen reduction catalysts. *Angew. Chem., Int. Ed.* **2014**, *53* (2014), 3675–3679.

(20) Miner, E. M.; Wang, L.; Dincă, M. Modular O₂ electro-reduction activity in triphenylene-based metal–organic frameworks. *Chem. Sci.* **2018**, *9*, 6289–6291.

(21) Liu, X.-H.; Hu, W.-L.; Jiang, W.-J.; Yang, Y.-W.; Niu, S.; Sun, B.; Wu, J.; Hu, J.-S. Well-defined metal–O₆ in metal–catecholates as a novel active site for oxygen electroreduction. *ACS Appl. Mater. Interfaces* **2017**, *9*, 28473–28477.

(22) Kong, D.; Gao, Y.; Xiao, Z.; Xu, X.; Li, X.; Zhi, L. Rational design of carbon-rich materials for energy storage and conversion. *Adv. Mater.* **2019**, *31*, 1804973.

(23) Huang, Z.-F.; Wang, J.; Peng, Y.; Jung, C.-Y.; Fisher, A.; Wang, X. Design of efficient bifunctional oxygen reduction/evolution electrocatalyst: recent advances and perspectives. *Adv. Energy Mater.* **2017**, *7*, 1700544.

(24) Yang, W.; Liu, X.; Yue, X.; Jia, J.; Guo, S. Bamboo-like carbon nanotube/Fe₃C nanoparticle hybrids and their highly efficient catalysis for oxygen reduction. *J. Am. Chem. Soc.* **2015**, *137*, 1436–1439.

(25) Kim, J. H.; Sa, Y. J.; Jeong, H. Y.; Joo, S. H. Roles of Fe–N_x and Fe–Fe₃C@C species in Fe–N/C electrocatalysts for oxygen reduction reaction. *ACS Appl. Mater. Interfaces* **2017**, *9*, 9567–9575.

(26) Sun, T.; Jiang, Y.; Wu, Q.; Du, L.; Zhang, Z.; Yang, L.; Wang, X.; Hu, Z. Is iron nitride or carbide highly active for oxygen reduction reaction in acidic medium? *Catal. Sci. Technol.* **2017**, *7*, 51–55.

(27) Hu, E.; Yu, X.-Y.; Chen, F.; Wu, Y.; Hu, Y.; Lou, X. W. Graphene layers-wrapped Fe/Fe₃C₂ nanoparticles supported on N-doped graphene nanosheets for highly efficient oxygen reduction. *Adv. Energy Mater.* **2018**, *8*, 1702476.

(28) Yang, S.; Jiang, J.-T.; Xu, C.-Y.; Wang, Y.; Xu, Y.-Y.; Cao, L.; Zhen, L. Synthesis of Zn(II)-doped magnetite leaf-like nanorings for efficient electromagnetic wave absorption. *Sci. Rep.* **2017**, *7*, 45480.

(29) Filippidi, E.; Cristiani, T. R.; Eisenbach, C. D.; Waite, J. H.; Israelachvili, J. N.; Ahn, B. K.; Valentine, M. T. Toughening elastomers using mussel-inspired iron-catechol complexes. *Science* **2017**, *358*, 502–505.

(30) Côté, A. P.; Benin, A. I.; Ockwig, N. W.; O’Keeffe, M.; Matzger, A. J.; Yaghi, O. M. Porous, crystalline, covalent organic frameworks. *Science* **2005**, *310*, 1166–1170.

Publication II

Ping, K.; Alam, M.; Käärik, M.; Leis, J.; Kongi, N.; Järving, I.; Starkov, P.

Surveying iron–organic framework TAL–1-derived materials in ligandless heterogeneous oxidative catalytic transformations of alkylarenes.

Synlett **2019**, 30, 1536–1540.

DOI:10.1055/s-0037-1611877

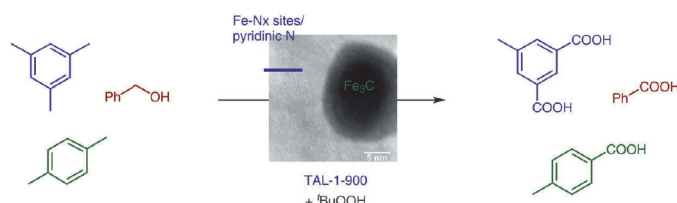
Surveying Iron–Organic Framework TAL-1-Derived Materials in Ligandless Heterogeneous Oxidative Catalytic Transformations of Alkylarenes

Kefeng Ping^aMahboob Alam^aMaike Käärik^bJaan Leis^bNadežda Kongi^bIvar Järving^aPavel Starkov^{*a} 

^a Department of Chemistry and Biotechnology, Tallinn University of Technology, 15 Akadeemia Rd, Tallinn, 12618, Estonia
pavel.starkov@taltech.ee

^b Institute of Chemistry, University of Tartu, 14a Ravila St, Tartu, 50411, Estonia

Published as part of the Special Section 10th EuCheMS Organic Division Young Investigator Workshop



Received: 09.04.2019

Accepted after revision: 07.06.2019

Published online: 03.07.2019

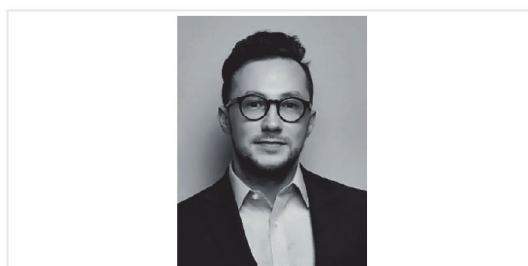
DOI: 10.1055/s-0037-1611877; Art ID: st-2019-v0201-I

Abstract The use of carbonized materials derived from metal–organic frameworks (MOFs) in catalytic organic transformations is less well explored than is the use of MOFs. Here, we survey the oxidative performance of heterogeneous catalyst materials derived from the polycrystalline iron–organic framework TAL-1.

Key words iron catalysis, oxidation, sustainable chemistry, metal–organic framework, alkyl arenes, carboxylic acids

Besides their many other noteworthy applications,^{1–3} metal–organic frameworks (MOFs) are an established platform for chemocatalysis.^{2–5} However, much less is known about the chemical performance of the carbonized materials derived from the corresponding MOFs containing metal–ligand and/or purely N-based sites.^{6–8} We recently showed that, by altering the structure of the underlying fused hybrid carbon-rich organic linkers,⁹ one can achieve substantial gains in the electrochemical performance of single-precursor-derived MOF-based electrocatalyst materials in oxygen reduction reactions (ORRs) and oxygen evolution reactions (OERs).^{10,11} Here, we assess the best-performing electrocatalyst from the ORR/OER series, TAL-1-900, and its precursor TAL-1 (Scheme 1) in various catalytic oxidative transformations.¹²

In 1964, Jasinski reported¹³ cobalt phthalocyanine as the first ORR electrocatalyst material not based on a platinum-group metal.^{14–16} Its performance was originally assessed (along with the Fe, Ni and Cu-based systems) in oxidative organic transformations.¹³ In the present work, we



Pavel Starkov was born in Tallinn, Estonia. He obtained his BSc *cum laude* in natural sciences from the University of Tartu, Estonia; his MRes in biomolecular science from Imperial College, London (research project with Professor Alan Armstrong and Dr David Mann); and, in 2011, his Ph.D. in chemistry from University College London, under the guidance of Professor Tom Sheppard. Before completing his Ph.D., he joined Professor Ulrike Eggert at Harvard Medical School and later relocated to Israel for a research stay with Professor Rafal Klajn at the Weizmann Institute of Science and Professor Ilan Marek at Technion–Israel Institute of Technology. Pavel joined Tallinn University of Technology as a senior research scientist (independent PI) in 2016.

intended to take a reciprocal approach by examining the performance of the recently developed electrocatalyst TAL-1-900 and its direct precursor in oxidative reactions.¹¹

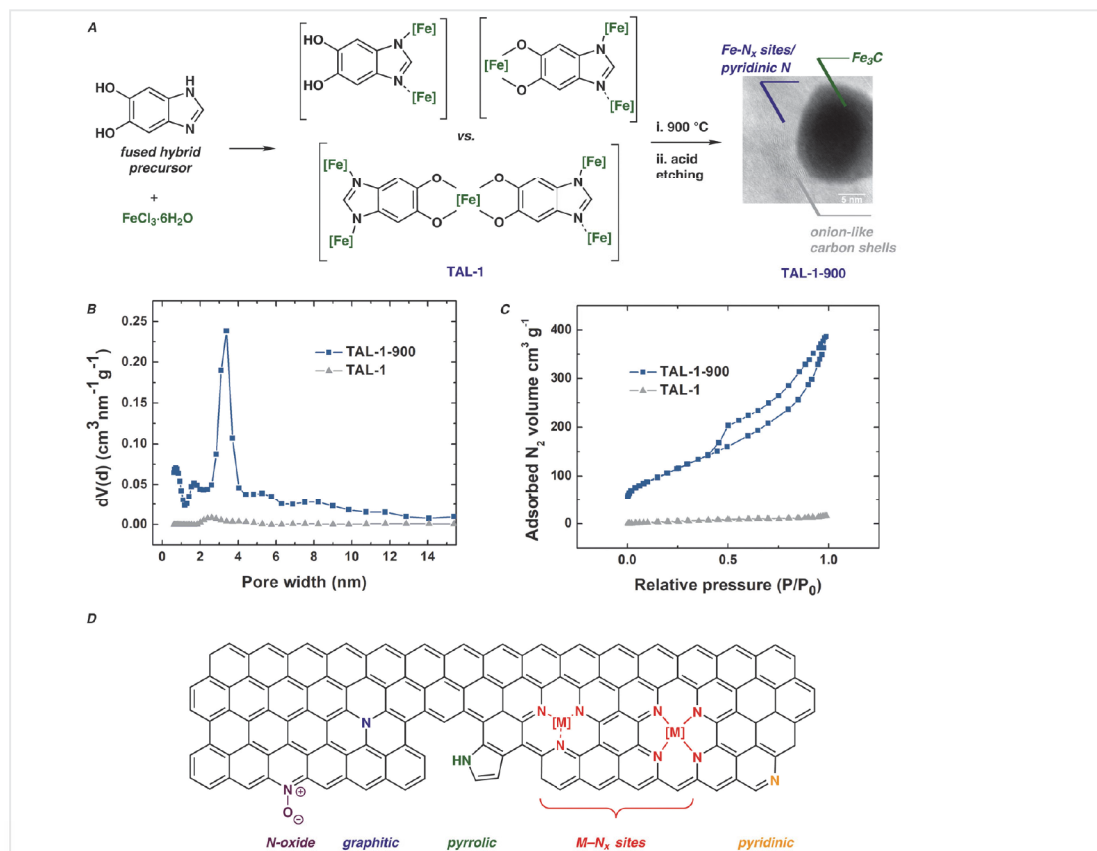
Whereas TAL-1 is a nonporous polycrystalline MOF, TAL-1-900 is a porous material (Scheme 1b and 1c) obtained from TAL-1 by carbonization at 900 °C and subsequent acid leaching. The latter procedure removes iron oxides from the surface of the material and decreases the amount of α -Fe in the carbon onion-shell-embedded α -Fe/Fe₃C nanocrystals. This results in a final catalyst material, TAL-1-900, that has a significantly higher porosity than

TAL-1. Moreover, TAL-1-900 can be utilized in metal-catalyzed transformations in a ligand-free manner, as the Fe–N_x and other sites with potential catalytic activity (e.g., pyridinic, pyrrolic, or graphitic nitrogens) are preassembled during the carbonization step (Scheme 1d) and subsequently made accessible by acid etching.¹¹ For instance, the presence and precise distribution of these active sites is known to be essential for the overall performance of the bifunctional electrocatalyst materials in electrochemical OER/ORR reactions.^{15–18}

One challenge that we wished to address by using our newly developed materials was the practical, laboratory-bench conversion of alkylarenes¹⁹ into the corresponding arylcarboxylic acids or ketones. To this end, the classical approach relies on the stoichiometric use of a strong oxidant, typically, KMnO₄.²⁰ In 2007, Nakanishi and Bolm introduced an iron chloride-catalyzed oxidation conducted in pyridine with *tert*-butyl hydroperoxide (TBHP) as the terminal oxi-

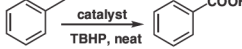
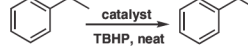
dant.²¹ Given the fact that our bifunctional ORR/OER electrocatalyst TAL-1-900 and its MOF precursor TAL-1 incorporated ligated iron centers,¹¹ we wished to investigate their performance in similar transformations.

We have screened the iron-based TAL-1 and TAL-1-900 systems in two classical transformations in order to determine which of the two is the more robust catalyst (Table 1).²² We used a 70% aqueous solution of TBHP as the terminal oxidant. In our hands, TAL-1 caused rapid decomposition of TBHP and **should be handled with extreme care**. With regard to the oxidation of toluene, TAL-1 showed low activity (up to a 14% isolated yield of benzoic acid), whereas TAL-1 exhibited much greater activity in the oxidation of ethylbenzene to acetophenone. Gratifyingly, TAL-1-900 showed a more-consistent performance in converting toluene into benzoic acid (Reaction A) and ethylbenzene into acetophenone (Reaction B) (entries 4–7).



Scheme 1 (a) Preparation of TAL-1 and TAL-1-900. (b) Pore sizes in TAL-1 and TAL-1-900 catalysts. (c) Dinitrogen adsorption/desorption by TAL-1 and TAL-1-900. (d) Diversity of the potential nitrogen (N) catalytic sites in carbonized TAL-1-900 catalyst, in addition to the matrix-embedded metal carbide nanocrystals.

Table 1 Optimization of the Reaction Conditions for the Oxidation of Toluene (Reaction A) and Ethylbenzene (Reaction B)^a

Reaction A		Reaction B		
				
Entry	Catalyst ^b	TBHP (equiv)	Isolated yield (%)	
			Reaction A	Reaction B
1	TAL-1	3	11	9
2	TAL-1	6	11	34
3	TAL-1	10	14	50
4	TAL-1-900	3	28	24
5	TAL-1-900	6	34	44
6	TAL-1-900 ^c	6	34	67
7	TAL-1-900	10	35	45

^a Reaction conditions: 70% aq. TBHP, neat, 80 °C, 16 h.^b Catalyst loading: 5 mg/mmol of substrate, except entry 6.^c Catalyst loading: 10 mg/mmol of substrate.

The robust performance of TAL-1-900 was enhanced by its stability and by its potential to serve as a recoverable and recyclable catalyst. The surface of porous TAL-1-900 is covered with catalytically active Fe–N_x sites (pyridinic, pyrrolic, and graphitic nitrogen), as shown by X-ray photoelectron spectroscopy.¹¹ The use of highly organized materials as catalysts can often reduce the need for complimentary ligands and bases, and can ensure that low levels of metal leaching occur, potentially rendering the heterogeneous catalyst material recyclable.

Next, we wished to investigate the catalytic performance of TAL-1-900 in converting various alkylarenes into the corresponding carboxylic acids or ketones (Table 2).^{19,22} Toluene, benzyl alcohol, and phenylacetic acid were converted into benzoic acid (entries 1–3). It is likely that phenylacetic acid is initially oxidized to phenylglyoxylic acid, which then undergoes decarboxylation by the TBHP radical.^{23,24} In the case of polymethylated arenes, the major isolated products are shown in Table 2 (entries 4–6). *m*-Xylene gave isophthalic acid (entry 4), *p*-xylene gave *p*-toluic acid (entry 5), and mesitylene was converted into 5-methylisophthalic acid in 38% yield (entry 6). Ethylbenzene (entries 8 and 9) and diphenylmethane (entries 10 and 11)

Table 2 TAL-1-900-Catalyzed Oxidations^a

Entry	Substrate	Major product	TBHP (equiv)	Isolated yield (%)
1	toluene	benzoic acid	6	37
2	BnOH	benzoic acid	3	84
3	PhCH ₂ CO ₂ H	benzoic acid	3	49
4			6	70
5	<i>m</i> -xylene	isophthalic acid	12	32
6	<i>p</i> -xylene	4-MeC ₆ H ₄ CO ₂ H	12	34
7	mesitylene	uritic acid	18	38
8	PhEt	PhCOMe	3	50
9			6	54
10	Ph ₂ CH ₂	Ph ₂ CO	3	47
11			6	94

^a Reaction conditions: TAL-1-900 (5 mg/mmol of substrate), 70% aq TBHP, neat, 80 °C, 24 h.

were converted into the corresponding ketones; increasing the number of equivalents of TBHP from three to six increased the isolated yield of benzophenone (entry 11).

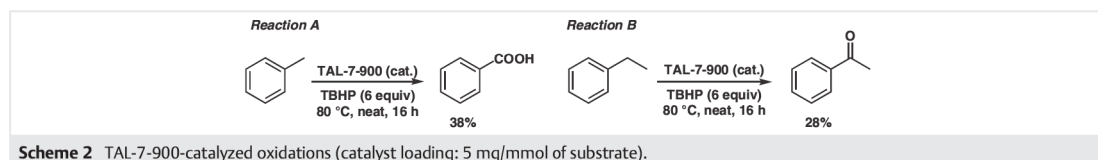
Finally, we showed that the TAL-1-900 catalyst could be reused several times (Table 3).

Table 3 Recycling Experiments^a

Reaction A		Reaction B	
Cycle		Yield ^b (%)	
		Reaction A	Reaction B
1		35	89
2		35	90
3		40	91

^a Reaction conditions: 70% aq. TBHP, neat, 80 °C, 16 h; catalyst loading: 5 mg/mmol of substrate.^b Determined by NMR with 1,3,5-trimethoxybenzene as internal standard.

We then tested a related catalyst material obtained from TAL-7. This was prepared from 5,6-dimethoxy-1*H*-benzo[d]imidazole, a methyl-protected version of the TAL-1 organic precursor 1*H*-benzo[d]imidazole-5,6-diol.¹⁰ Interest-



ingly, catalyst TAL-7-900 performed similarly to TAL-1-900 in the oxidation of toluene (Scheme 2; isolated yield 38% vs. 34%); however, the yield from the oxidation of ethylbenzene was significantly less (28% vs. 44%).

We have previously shown by microwave plasma atomic-emission spectroscopy that the total amount of iron in TAL-1-900 (0.896 ± 0.006 wt%) differs from that in TAL-7-900 (3.603 ± 0.035 wt%).¹¹ Despite the fact that TAL-7-900 contains about four times as much iron as TAL-1-900, we found that TAL-1-900 performed as well as or slightly better than TAL-7-900 in oxidative transformations (Reactions A and B; Table 1 and Scheme 2). Notably, whereas the two benzimidazole-based organic linkers used to prepare TAL-1- and TAL-7-derived catalysts both contain electron-donating groups (OH and OMe, respectively), only the unprotected catechol had the propensity to form bis- and triscatecholato complexes with iron.²⁵ Hence, the precise nature of the iron complexes formed at the surface of the catalyst material following carbonization might contribute to the overall catalytic performance of our heterogeneous catalysts. In practice, one would seek to employ additional porous carbon supports,²⁶ which might increase the accessible specific surface area of the final catalyst material.

In summary, we have shown that iron-based TAL-1-900 is a reliable catalyst for the oxidation of alkylarenes to the corresponding carboxylic acids or ketones. Because the total iron content in this heterogeneous catalyst is very low ($\leq 1\%$), its performance as a catalyst is promising. The long-term advantages of using metal-doped carbonized materials as catalysts for organic transformations include their recyclability, low metal leaching, and no requirement for additional ligands.

Funding Information

Funding Information: Tallinna Tehnikaülikool, (Grant/Award Number: B62) Eesti Teadusagentuur, (Grant/Award Number: IUT19-9, IUT34-14, PSG250, and PUT1290).

Acknowledgment

This research was funded by Estonian Research Council Grant PUT1290 and TalTech Young Investigator Grant B62 (both to P.S.). K.P. acknowledges the Estonian Smart Specialization Ph.D. Fellowship. The BET measurements were funded by Institutional Research Grant IUT34-14. The HRMS facilities are funded by Institutional Research Funding IUT19-9. N.K. is funded by Estonian Research Council Grant PSG250.

Supporting Information

Supporting information for this article is available online at <https://doi.org/10.1055/s-0037-1611877>.

References and Notes

- Yuan, S.; Feng, L.; Wang, K.; Pang, J.; Bosch, M.; Lollar, C.; Sun, Y.; Qin, J.; Yang, X.; Zhang, P.; Wang, Q.; Zou, L.; Zhang, Y.; Zhang, L.; Fang, Y.; Li, J.; Zhou, H.-C. *Adv. Mater.* **2018**, *30*, 1704303.
- Kirchon, A.; Feng, L.; Drake, H. F.; Joseph, E. A.; Zhou, H.-C. *Chem. Soc. Rev.* **2018**, *47*, 8611.
- Jiao, L.; Seow, J. Y. R.; Skinner, W. S.; Wang, Z. U.; Jiang, H.-L. *Mater. Today*; DOI: 10.1016/j.mattod.2018.10.038
- Dhakshinamoorthy, A.; Li, Z.; Garcia, H. *Chem. Soc. Rev.* **2018**, *47*, 8134.
- Yang, D.; Gates, B. C. *ACS Catal.* **2019**, *9*, 1779.
- Oar-Arteta, L.; Wezendonk, T.; Sun, X.; Kapteijn, F.; Gascon, J. *Mater. Chem. Front.* **2017**, *1*, 1709.
- Chen, Y.-Z.; Zhang, R.; Jiao, L.; Jiang, H.-L. *Coord. Chem. Rev.* **2018**, *362*, 1.
- Liu, L.; Corma, A. *Chem. Rev.* **2018**, *118*, 4981.
- Kong, D.; Gao, Y.; Xiao, Z.; Xu, X.; Li, X.; Zhi, L. *Adv. Mater.*; DOI: 10.1002/adma.201804973
- For leading references on the use of MOF-derived carbonized materials in ORR/OER, see: (a) Zhao, S.; Yin, H.; Du, L.; He, L.; Zhao, K.; Chang, L.; Yin, G.; Zhao, H.; Liu, S.; Tang, Z. *ACS Nano* **2014**, *8*, 12660. (b) Xia, B. Y.; Yan, Y.; Li, N.; Wu, H. B.; Lou, X. W.; Wang, X. *Nat. Energy* **2016**, *1*, 15006. (c) Li, J.; Chen, M.; Cullen, D. A.; Hwang, S.; Wang, M.; Li, B.; Liu, K.; Karakalos, S.; Lucero, M.; Zhang, H.; Lei, C.; Xu, H.; Sterbinsky, G. E.; Feng, Z.; Su, D.; More, K. L.; Wang, G.; Wang, Z.; Wu, G. *Nat. Catal.* **2018**, *1*, 935. (d) Wang, R.; Yan, T.; Han, L.; Chen, G.; Li, H.; Zhang, J.; Shia, L.; Zhang, D. *J. Mater. Chem. A* **2018**, *6*, 5752.
- Ping, K.; Braschinsky, A.; Alam, M.; Bhadoria, R.; Mikhli, V.; Mere, A.; Aruväli, J.; Paiste, P.; Vlassov, S.; Kook, M.; Rähn, M.; Sammelselg, V.; Tammeveski, K.; Kongi, N.; Starkov, P. *ChemRxiv* **2019**; preprint; DOI: 10.26434/chemrxiv.7687358
- For recent references on the use of MOF-derived carbonized materials in organic transformations, see: (a) Jagadeesh, R. V.; Murugesan, K.; Alshammari, A. S.; Neumann, H.; Pohl, M.-M.; Radnik, J.; Beller, M. *Science* **2017**, *358*, 326–332. (b) Murugesan, K.; Beller, M.; Jagadeesh, R. V. *Angew. Chem. Int. Ed.* **2019**, *58*, 5064–5068. (c) Gong, W.; Lin, Y.; Chen, C.; Al-Mamun, M.; Lu, H.-S.; Wang, G.; Zhang, H.; Zhao, H. *Adv. Mater.* **2019**, *31*, 1808341. (d) Xie, F.; Lu, G.-P.; Xie, R.; Chen, Q.-H.; Jiang, H.-F.; Zhang, M. *ACS Catal.* **2019**, *9*, 2718. (e) Wu, Y.; Chen, Z.; Cheong, W.-C.; Zhang, C.; Zheng, L.; Yan, W.; Yu, R.; Chen, C.; Li, Y. *Chem. Sci.* **2019**, *10*, 5345.
- Jasinski, R. *Nature* **1964**, *201*, 1212.
- Xia, W.; Mahmood, A.; Liang, L.; Zou, R.; Guo, S. *Angew. Chem. Int. Ed.* **2016**, *55*, 2650.
- Masa, J.; Xia, W.; Muhler, M.; Schuhmann, W. *Angew. Chem. Int. Ed.* **2015**, *54*, 10102.
- Shao, M.; Chang, Q.; Dodelet, J.-P.; Chenitz, R. *Chem. Rev.* **2016**, *116*, 3594.
- Yang, H. B.; Miao, J.; Hung, S.-F.; Chen, J.; Tao, H. B.; Wang, X.; Zhang, L.; Chen, R.; Gao, J.; Chen, H. M.; Dai, L.; Liu, B. *Sci. Adv.* **2016**, *2*, e1501122.
- Zhang, L.; Xiao, J.; Wang, H.; Shao, M. *ACS Catal.* **2017**, *7*, 7855.
- Vanjari, R.; Singh, K. N. *Chem. Soc. Rev.* **2015**, *44*, 8062.
- Hudlicky, H. *Oxidations in Organic Chemistry*, ACS Monograph No. 186; American Chemical Society: Washington, **1990**.
- Nakanishi, M.; Bolm, C. *Adv. Synth. Catal.* **2007**, *349*, 861.
- 5-Methylisophthalic Acid (Table 2, Entry 7): Typical Procedure**
A mixture of mesitylene (100 mg, 0.832 mmol, 1.0 equiv), 70% aq TBHP (2.05 mL, 14.98 mmol, 18.0 equiv), and TAL-1-900 (4.2

mg) was stirred at 80 °C for 24 h. It was then filtered through a Celite pad with MeOH. The resulting solution was concentrated under reduced pressure then purified by flash chromatography [silica gel, EtOAc-PE (1:20 to 1:10)] to give a colorless solid; yield: 57.2 mg (0.317 mmol, 38%); mp 296–297 °C.

^1H NMR (400 MHz, DMSO- d_6): δ = 13.18 (s, 2 H), 8.28 (s, 1 H),

7.98 (s, 2 H), 2.43 (s, 3 H). ^{13}C NMR (100 MHz, DMSO- d_6): δ = 166.7, 138.8, 133.9, 131.2, 127.3, 20.6. HRMS (ESI): m/z [$\text{M} + \text{H}$] $^+$ calcd. for $\text{C}_9\text{H}_9\text{O}_4$: 181.0495; found: 181.0496.

(23) Zhang, S.; Guo, L.-N.; Wang, H.; Duan, X.-H. *Org. Biomol. Chem.* **2013**, *11*, 4308.

(24) Barton, D. H. R.; Le Gloahec, V. N. *Tetrahedron* **1998**, *54*, 15457.

(25) Xu, Z. *Sci. Rep.* **2013**, *3*, 2914.

(26) Qi, J.; Zhang, W.; Cao, R. *ChemCatChem* **2018**, *10*, 1206.

Publication III

Ping, K.; Alam, M.; Kahnert, S. R.; Bhadoria, R.; Mere, A.; Mikli, V.; Käär, M.; Aruväli, J.; Paiste, P.; Kikas, A.; Kisand, V.; Järving, I.; Leis, J.; Tammeveski, K.; Kongi, N.; Starkov, P.

Multi-purpose chemo- and electrocatalyst material from an amorphous cobalt metal–organic framework.

Manuscript submitted.

Multi-Purpose Heterogeneous Catalyst Material from an Amorphous Cobalt Metal–Organic Framework†

Kefeng Ping,^{‡a} Mahboob Alam,^{‡a} Sean Ray Kahnert,^{§a} Rohit Bhadoria,^a Arvo Mere,^c Valdek Mikli,^c Maike Käärrik,^b Jaan Aruväli,^d Päärn Paiste,^d Arvo Kikas,^e Vambola Kisand,^e Ivar Järving,^a Jaan Leis,^b Nadežda Kongi^{*b} and Pavel Starkov^{*a}

Sustainable technologies rely on the development of universal catalyst materials. While a lot of the attention has been given to improving the performance of one single catalyst material for one specific application, there is still a need to find ways to develop catalysts that can simultaneously be utilized for several chemo- and electrocatalytic processes. In this work, we have surveyed a series of novel, cobalt-based catalyst materials derived from an amorphous MOF in an array of diverged applications. Specifically, we have focused on organic transformations such as oxidative of alkylarenes and benzylic homocoupling reactions as well as several electrocatalytic processes, which directly relate to energy conversion and storage devices, such as oxygen reduction (ORR), oxygen evolution (OER) and hydrogen evolution (HER) reactions. We have observed that only one material, TAL–2–900, delivered the optimal solution. The stability and recyclability of this unique multifunctional material has been examined.

1. Introduction

The notion of M–N–C catalysts, where M is typically Fe, Co, Mn or Ni, is often reserved for the catalysts developed for applications in energy conversion and storage devices.^{1–3} However, recent reports have also emphasized the role of this type of materials in facilitating heterogeneous organic transformations.^{4–6}

There is an accountable divergence in the ways that the M–N–C materials are prepared, and they depend on the ultimate application prerogative.^{1–10} When used in the electrochemical settings, the underlying materials are typically acid-etched to make sure that the additional influence of related nanoparticles (metal and/or that of metal oxides, carbides, nitrides, sulfides and phosphides) deposited directly at the surface of the catalyst is eliminated. In heterogeneous catalysis applications, however, the contribution of these species to the overall chemical reactivity – while being well acknowledged and often relied upon – is not readily distinguished from the instances of single-atom catalysis^{9,10} and the role that nanocrystals protected by graphitic carbon layers might play.

Metal–organic frameworks (MOF) are one of the most attractive building blocks for the formation of active M–N–C materials.¹¹ Whereas only a handful of crystalline MOFs can directly be used as electrocatalysts,^{12–14} the vast majority of

MOFs still require an additional step of carbonization to allow for increased stability and conductivity as well as to introduce a variety of catalytically active species (M–N_x).¹¹ During this process, additional doping with heteroatoms and metals^{7,8} or the use of alternative supports^{15,16} is often advantageous.

While crystalline MOFs are widely used for carbonization,^{7,8} their innate crystallinity may not always be a critical factor to achieve high catalytic activities (aside from contributing to the topology of the composite). During pyrolysis, MOFs undergo drastic molecular rearrangements, while structural features of obtained materials do pertain the shape and dimensions of the original MOFs. Hence, amorphous MOFs can be used as the precursors.^{17,18} To this end, we have assessed iron-based catalysts derived from polycrystalline metal–organic framework (MOF) precursors,^{19,20} which were based on carbon-rich²¹ organic linkers. Even the slightest variations around the benzimidazole core have led to alterations in the performance of the materials as bifunctional oxygen electrocatalysts¹⁹ and in heterogeneous catalysis.²⁰ Herein, we report a unique cobalt-based single precursor-derived multifunctional material,^{22,23} which acts as an efficient trifunctional electrocatalyst and as a robust heterogeneous catalyst.

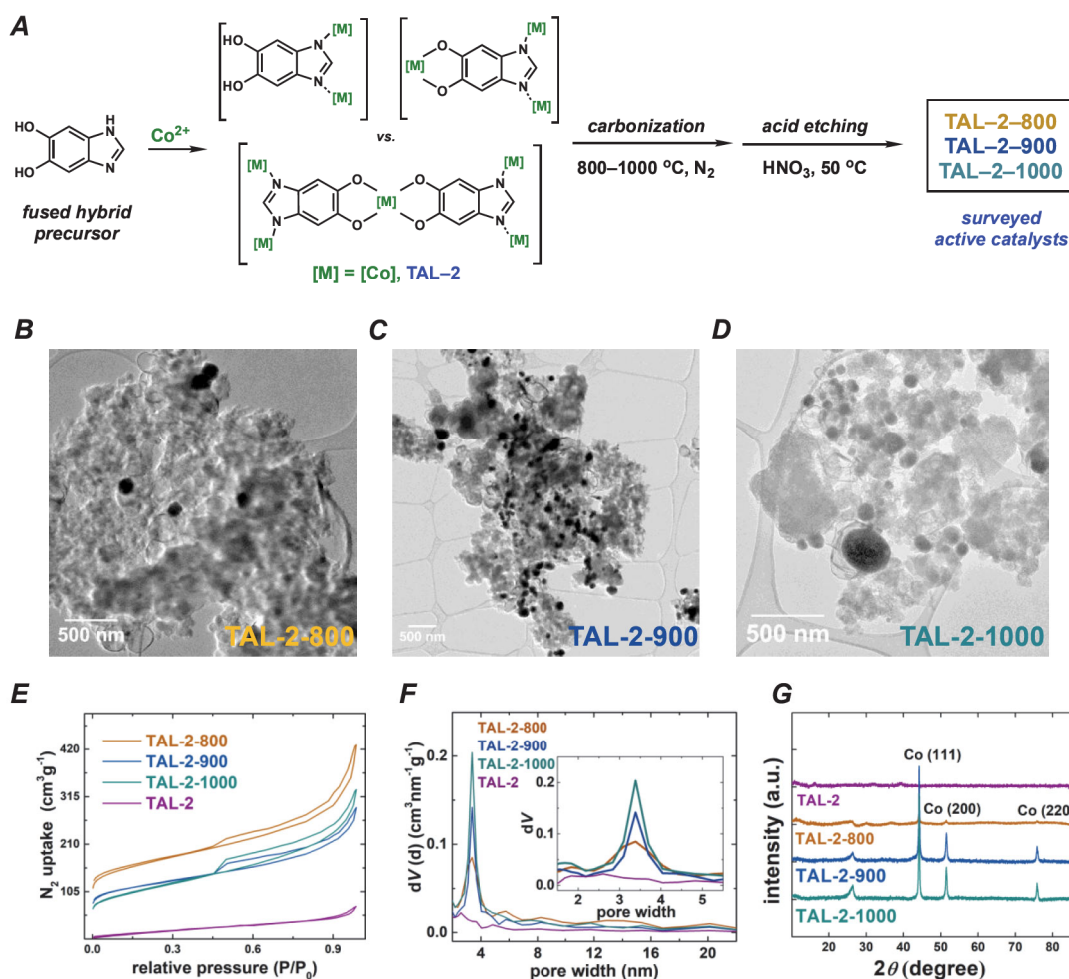


Fig. 1 (A) Preparation of TAL-2 derived catalysts materials. HRTEM micrographs of (B) TAL-2-800, (C) TAL-2-900 and (D) TAL-2-1000 catalysts. Physical characterization of the materials by (E) N_2 uptake, and (F) pore size distribution and (G) PXRD patterns.

2. Results and discussion

2.1 Morphological and physical characterizations

We prepared a series of catalysts from an amorphous metal-organic framework precursor TAL-2 by carbonizing it at different temperatures (Fig. 1). Importantly, we have treated these carbonized materials with 0.5 M HNO_3 to remove the traces of cobalt(0) and cobalt oxides from the surface of the materials. Regardless of this treatment, the final porous M-N-C materials still contained cobalt(0) nanoparticles, which were protected by the graphitic layers as is evident from the high resolution transmission electron microscopy (HRTEM; Fig. 1B-1D, S1 and S2) micrographs. Increasing the temperature of

carbonization did not lead to a substantial change in the N_2 adsorption/desorption isotherms or the distribution of pore sizes, which effectively remained in the 3–4 nm range (Fig. 1E and 1F). However, as is seen in the powder X-ray diffraction (PXRD; Fig. 1G) patterns and the microwave plasma-atomic emission spectroscopy (MP-AES; Table S1) datasets, the graphitic carbon and cobalt(0) content was significantly higher in the samples that have been treated at 900 and 1000 °C. The X-ray photoelectron spectroscopy (XPS) data indicated that carbonization at higher temperatures both lowered the nitrogen content and altered the distribution of nitrogen species at the surface (Fig. S3; Tables S1–S5).

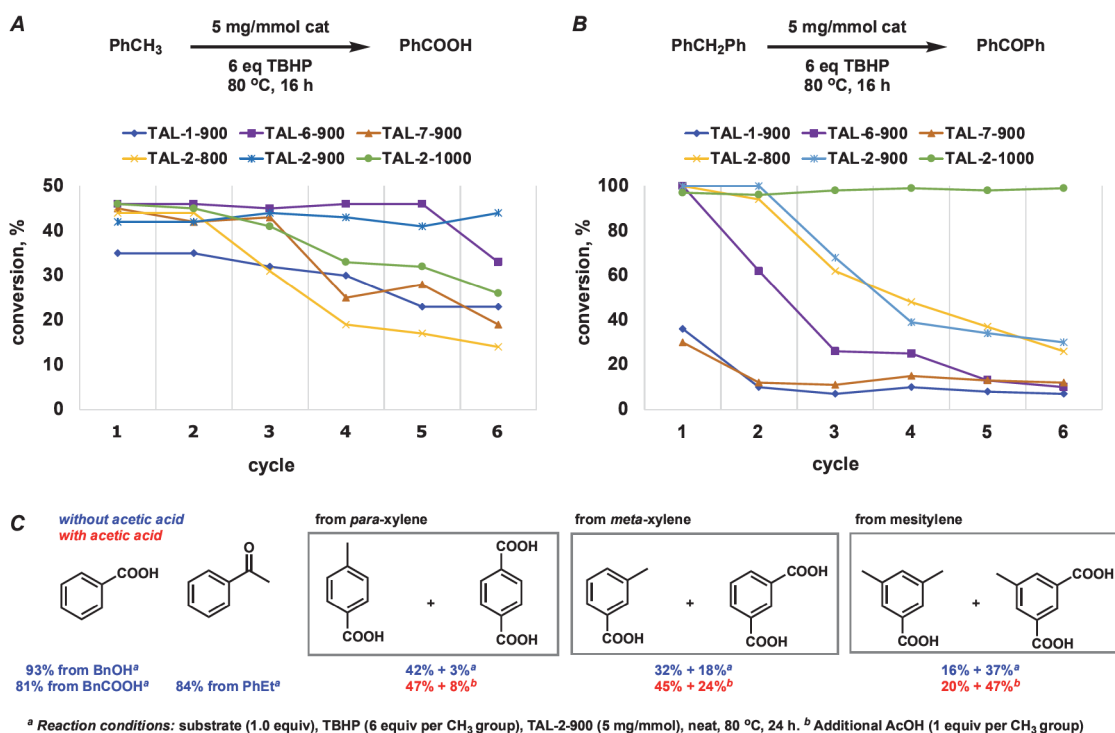


Fig. 2. Use of TAL-derived catalysts in oxidative transformations. (A) Catalyst recyclability during oxidation of toluene into benzoic acid. (B) Catalyst recyclability during oxidation of diphenylmethane into benzophenone (conversion were determined by NMR using 1,3,5-trimethoxybenzene as internal standard). (C) Substrate scope for TAL-2-900-catalyzed oxidations (isolated yields).

2.2 Oxidative organic transformations

The *de novo* Co–N–C catalysts were screened against oxidative transformations with *tert*-butyl peroxide (TBHP) as terminal oxidant at a considerably low catalyst loadings, namely, that of 5 mg/mmol. While TBHP-driven oxidations of arylmethanes have been reported to be catalyzed by Fe–N–C materials effectively,^{20, 24–26} the cobalt corresponding Co–N–C catalysts were not.²⁷ Typically, Co–N–C catalysts are used for reduction reactions (nitroarenes,^{28,29} *N*-heterocycles,³⁰ and hydrocarbons³¹), reductive aminations³² and alkylations,^{33,34} while the oxidative esterification of benzyl alcohols were done under dioxygen.^{35–37}

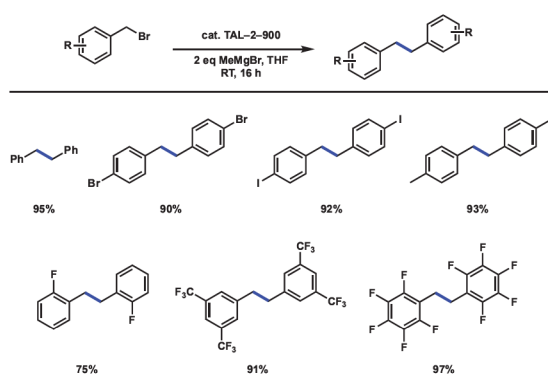
Overall, the cobalt materials outperformed the three previously reported related Fe–N–C systems (TAL-1-900, TAL-6-900, TAL-7-900),^{19,20} and importantly, they sustained their activity over a larger number of cycles (Fig. 2A and 2B; Tables S6 and S7). TAL-2-900 and TAL-2-1000 were more active because they contained metallic Co nanoparticles, which were protected by graphitic carbon layers, as confirmed by PXRD and HRTEM.

Interestingly, TAL-2-900 was a more robust catalyst for converting toluene to benzoic acid, while TAL-2-1000 was better at oxidizing diphenylmethane to benzophenone. This

indicates that small differences in the active sites (e.g. the total content of pyridinic nitrogen) at the surface of the catalyst play an important role in catalyst stability. A further set of substrates was subjected to oxidation (Fig. 2C). Addition of acetic acid slightly improved the yields in the cases where polymethylated arenes were converted to the corresponding carboxylic acids.

2.3 Benzylic homocoupling

Knowing that radical pathways were involved in oxidative transformation reactions, has encouraged us to extend the use of TAL-2-900 as a heterogeneous catalyst for carbon–carbon bond forming reactions via activation at the benzylic positions. While M–N–C materials are widely explored in oxidative and reductive processes,^{4–6} there is only a handful of examples of their use in other organic transformations. For instance, Zhang *et al.* developed an oxidative coupling between primary and secondary alcohols.³⁸ This reaction was shown to proceed via formation of intermediary aldehydes and ketones, respectively, which undergo aldol condensation. A reductive C–H alkylation of quinolines by aldehydes using cobalt-based catalysts was also demonstrated.^{39,40}



^a Reaction conditions: substrate (1.0 equiv), MeMgBr (2.0 equiv), TAL-2-900 (5 mg/mmol), THF, RT, 16 h

Scheme 1. TAL-2-900 catalyzed C(sp³)-C(sp³) homocoupling reactions.^a

We were interested to see whether the M-N-C catalysts could be compatible with organometallic reagents; hence, we explored C(sp³)-C(sp³) homocoupling reaction of benzyl bromides in the presence of a Grignard reagent. This reaction traditionally requires stoichiometric metallic lithium,⁴¹ magnesium,⁴² copper⁴³ or nickel.⁴⁴ Recently, a rhodium-catalyzed version employing dimethylzinc was demonstrated,⁴⁵ and several photocatalyzed conditions were developed.^{46,47} Gratifyingly, we observed the desired homocoupling products with cobalt based catalyst TAL-2-900 but not the iron version (TAL-1-900) (Scheme 1). The reactions were carried out using methylmagnesium bromide at ambient temperature to give corresponding bibenzyls in good to excellent yields, while aryl iodides and bromides were also well tolerated. After standard aqueous workup, the spent catalyst had a significantly reduced activity. Specifically, on the next cycle, the isolated yield of homocoupled product has dropped from 93% to 38%. Alternatively, the THF solution containing the product was removed by syringe under anhydrous conditions and the reaction vessel was recharged with THF, benzyl bromide and MeMgBr. This modification gave the desired product with an improved yield on the second run (93%).

2.4 Electrocatalytic transformations

After having identified the most promising catalyst for the organic transformations, we wished to screen the TAL-2 catalyst series as *trifunctional* electrocatalyst materials across oxygen reduction (ORR), oxygen evolution (OER) and hydrogen evolution (HER) reactions (Fig. 3). Potentially, these datasets should give insights into whether there is a link between the performance of the individual catalysts across electrocatalytic and chemocatalytic interconversions.^{48,49} Out of the three catalysts, TAL-2-900, once again, showed a superior activity profiles in all of the electrocatalytic reactions.

To learn the effect of different carbonization temperatures on electrocatalytic ORR performance, TAL-2 based catalysts were tested by rotating disc electrode (RDE) and rotating ring-disc electrode (RRDE) techniques in 0.1 M KOH electrolyte. Oxygen reduction polarization curves (Fig. 3A) confirmed that

TAL-2 based catalyst carbonized at 900 °C had the highest ORR electrocatalytic activity with an onset potential (E_{on}) of 1.00 V, a half-wave potential ($E_{1/2}$) of 0.85 V and a diffusion-limiting current density of -5.78 mA cm^{-2} . The kinetic parameters of TAL-2-900 were on par with the ones obtained for commercial Pt/C catalyst ($E_{on} = 1.01 \text{ V}$; $E_{1/2} = 0.86$; $j_d = -6.16 \text{ mA cm}^{-2}$) and other promising non-noble metal ORR catalysts (Table S9). Despite the fact that BET surface area of TAL-2-900 ($421 \text{ m}^2 \text{ g}^{-1}$) is lower than that obtained for TAL-2-800 ($589 \text{ m}^2 \text{ g}^{-1}$) (Table S11), the superior ORR performance of TAL-2-900 indicates higher density of electrochemically accessible active sites for ORR.

To shed light on the enhancement of the ORR activity, electrochemically active surface area (ECSA) of TAL-2 derived catalysts was estimated by collecting the electrochemical double-layer capacitance (C_{dl}) from CV curves (Table S10). The ECSA values have decreased for the samples that were obtained by increasing the carbonization temperatures. Hence, the superior electrocatalytic activity of the TAL-2-900 sample may be explained by a higher amount of ORR active sites, specifically in the form of cobalt(0) nanoparticles.

The Koutecky-Levich (K-L) plots were constructed using data derived from RDE (Fig. S4) and the calculated number of electrons transferred per oxygen molecule n was in all the cases approximately four. RRDE studies confirmed that oxygen reduction proceeds via a two-step $2 \times 2 \text{ H}_2\text{O}_2$ mechanism (Fig. S5B and S5C). The Tafel plot analysis demonstrated that the TAL-2-900 material had the highest slope value ($-76 \text{ mV decade}^{-1}$) against all the other samples that were surveyed in this study (Fig. 3B). Similarly to Pt/C, this means that the rate determining step for ORR is the first electron transfer step, whereby $\text{O}_{2(\text{ads})}$ is reduced to $\text{O}_2^{\cdot-}(\text{ads})$. A continuous potential cycling in the range between 0.6 and 1.0 V was used to assess the long-term stability of TAL-2-900, with $E_{1/2}$ shifting only by 20 mV after 5,000 cycles (Fig. 3C). The RDE studies have confirmed that TAL-2-900 was a highly stable active ORR electrocatalyst in 0.1 M KOH.

The electrocatalytic activity towards ORR of the TAL-2-900 material has also been tested under acidic conditions (0.5 M H_2SO_4 ; Fig. S7). As in the case of alkaline media, TAL-2-900 has shown higher onset and half-wave potentials (0.82 V and 0.73 V vs. RHE) than those for TAL-2-800 and TAL-2-1000. Notably, TAL-2-900 remained stable after 5,000 cycles with $E_{1/2}$ having decreased only by 20 mV (Fig. S7D).

The OER performance of the TAL-2 derived catalysts was assessed and iR -corrected OER polarization curves are shown in Fig. 3D. The benchmark current density of 10 mA cm^{-2} was achieved at 1.60 V for TAL-2-900 material, which is superior to that of ruthenium oxide (1.69 V). The Tafel slopes obtained for the OER electrocatalytic activity among the series, confirm that TAL-2-900 functions similarly to the RuO_2 systems. Under the long-term OER operation, this catalyst material is stable (Fig. 3F). The overall oxygen bifunctional electroactivity (ΔE) value for TAL-2-900 is 0.75 V, which makes it much lower than the rest of the M-N-C samples, whilst haven been screened at the similar loadings (Table S10).

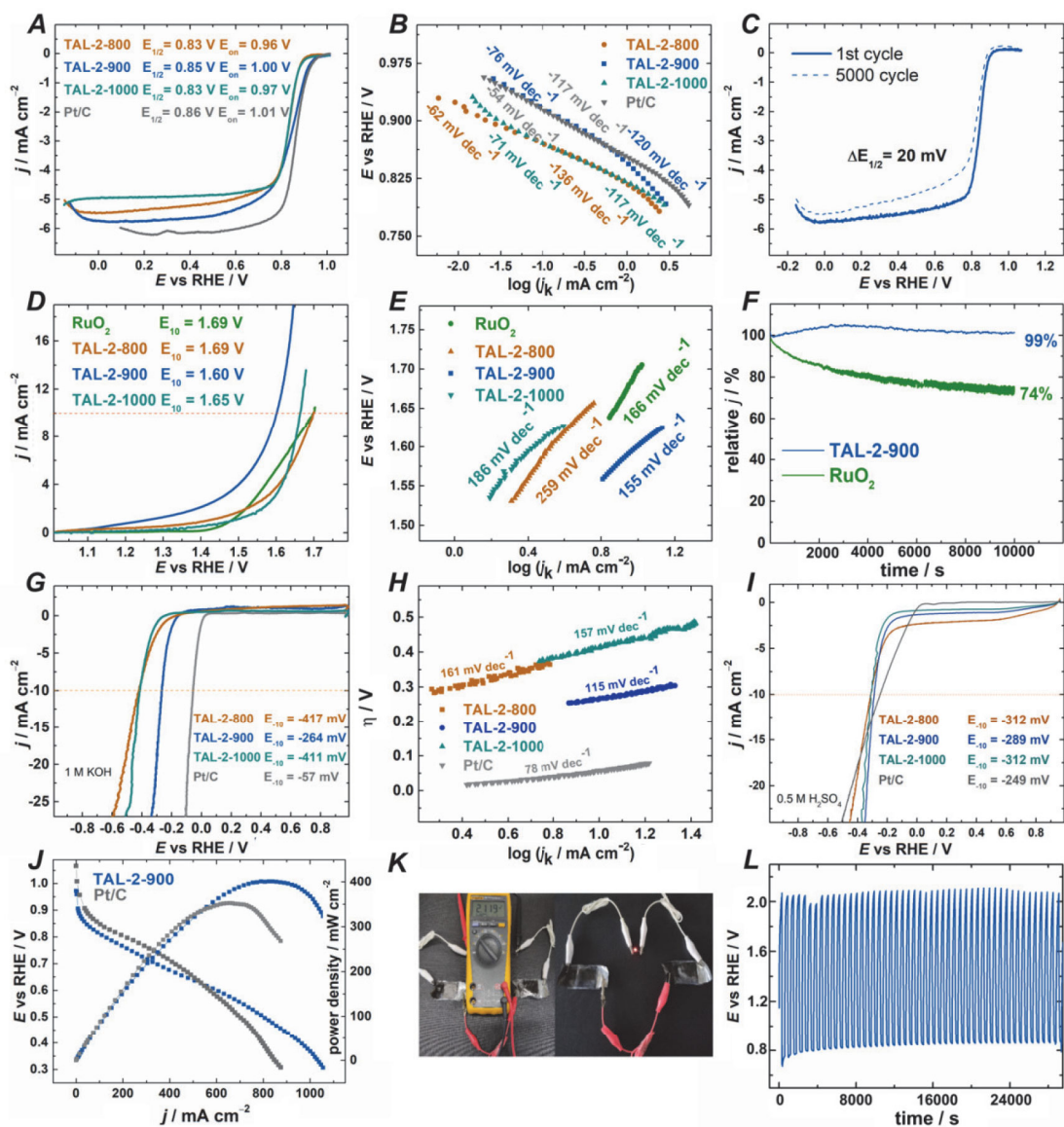


Fig. 3. Electrochemical characterization of TAL-2 derived catalyst materials. (A) ORR polarization curves for TAL and Pt/C-modified GC electrodes at 1600 rpm; $\nu = 10$ mV s⁻¹. (B) Tafel plots for ORR on TAL and Pt/C catalysts. (C) Electrochemical ORR stability test for TAL-2-900 (mid-range: 0.6–1.0 V). (D) OER polarization curves (under argon); $\nu = 10$ mV s⁻¹. (E) OER Tafel plots. (F) OER chronoamperometric stability of TAL-2-900 and RuO₂ in 0.1 M KOH over 10,000 seconds (1.6 V). (G) HER polarization curves for TAL and Pt/C electrocatalysts in 1 M KOH; $\nu = 10$ mV s⁻¹. (H) HER Tafel plots for TAL and Pt/C electrocatalysts in 1 M KOH. (I) HER polarization curves for TAL and Pt/C electrocatalysts in 0.5 M H₂SO₄; $\nu = 10$ mV s⁻¹. (J) Alkaline single fuel cell test of TAL-2-900 and Pt/C. (K) Zinc-air battery testing with TAL-2-900, shows the voltage produced by two batteries, LED light using the same batteries, and (L) galvanostatic cycling of one battery for 8 h.

The electrocatalytic HER activity of the best performing catalyst was compared with the commercial Pt/C in 1 M KOH (Fig. 3G and 3H) at the current density of -10 mA cm^{-2} . Under these conditions, the overpotential with TAL-2-900 as a catalyst was achieved at -264 mV vs. RHE with a low Tafel slope value of 115 mV dec^{-1} . The HER overpotential values η for TAL-2-800 and TAL-2-1000 were 417 and 411 mV, respectively, indicating that the carbonization step at 900°C was the optimal path to improve the electroactivity toward HER. In acidic media, the overpotential (η) was the smallest for TAL-2-900, while its overpotential was comparable to the values obtained for other Pt-free HER catalysts (Fig. 3I, Table S9).

Finally, the performance of TAL-2-900 as catalyst material was evaluated in alkaline electrolyte membrane fuel cell and zinc-air battery. Alkaline membrane fuel cell test yielded current density up to 1100 mA cm^{-2} (Fig. 3J). Loading of the catalyst was kept at 2 mg cm^{-2} on GDL membrane modified with direct suspension pipetting. HMT-PMBI (hydroxide conducting membrane) was used as polymer electrolyte in both tests for Pt/C and TAL-2-900. Under similar conditions, TAL-2-900 showed 20% better activity than Pt/C. The value of power density for TAL-2-900 is $> 400 \text{ mW cm}^{-2}$ leaving behind Pt/C 350 mW cm^{-2} . Similar results were recently reported using the same anion exchange membrane and an alternative Co-N-C material as a cathode catalyst.⁵⁰ Durability tests of poly(vinyl alcohol)-based solid-state zinc-air battery assembled using TAL-2-900 as an electrode material were performed by cycling at constant current density of 5.0 mA cm^{-2} (Fig. 3K). As expected from the ORR/OER data, TAL-2-900 catalyst-driven Zn-air battery delivered long cycle life over 8 h (Fig. 3L).

3. Conclusions

In conclusion, by using a combination of cobalt and dihydroxybenzimidazole as a carbonaceous linker, we have prepared an amorphous metal-organic framework. Upon carbonization, it delivered a unique Co-N-C material, which simultaneously served as a heterogeneous catalyst for several organic transformations (incl. oxidation and homocoupling reactions) as well as an electrocatalyst material for ORR, OER and HER processes. This is the first example of an M-N-C catalyst being used for $\text{C}(sp^3)\text{-C}(sp^3)$ carbon-carbon bond formation, and it was carried out in the presence of an organometallic reagent.

Author Contributions

Kefeng Ping, Mahboob Alam: investigation, methodology, formal analysis, validation, writing - original draft; writing - review & editing; **Sean Ray Kahnert, Rohit Bhadoria, Arvo Mere, Valdek Mikli, Maike Käärik, Jaan Aruväli, Päärn Paiste, Arvo Kikas, Vambola Kisand, Ivar Järving, Jaan Leis:** investigation, methodology, formal analysis, writing - review & editing; **Nadežda Kongi, Pavel Starkov:** conceptualization, supervision, writing - original draft, writing - review & editing, funding acquisition.

Conflicts of interest

K.P., N.K. and P.S. are inventors on the PCT Appl. filed by the University of Tartu and Tallinn University of Technology.

Acknowledgements

This research was supported by Estonian Research Council (PSG250 and PUT1290) and TalTech Young Investigator Grant B62. We thank Prof. Steven Holdcroft (Simon Fraser University) for providing the HMT-PMBI membrane. The measurement facilities were supported by Institutional Research Grants IUT34-14 and TK141 (Advanced materials and high-technology devices for energy recuperation systems). K.P. acknowledges Estonian Smart Specialization PhD Fellowship. P.S. thanks COST Action CA18224 members (<https://greenering.eu>) for fruitful discussions.

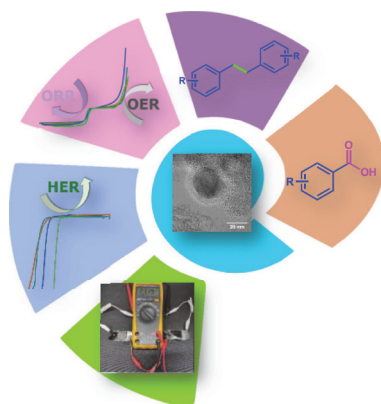
Notes and references

- Z. W. Seh, J. Kibsgaard, C. F. Dickens, I. Chorkendorff, J. K. Nørskov and T. F. Jaramillo, *Science*, 2017, **355**, eaad4998.
- J. Masa, C. Andronesco and W. Schuhmann, *Angew. Chem. Int. Ed.*, 2020, **59**, 15298–15312.
- A. Sarapuu, E. Kibena-Pöldsepp, M. Borghei and K. Tammeveski, *J. Mater. Chem. A*, 2018, **6**, 776–804.
- L. He, F. Weniger, H. Neumann and M. Beller, *Angew. Chem. Int. Ed.*, 2016, **55**, 12582–12594.
- L. Liu and A. Corma, *Chem. Rev.*, 2018, **118**, 4981–5079.
- M. B. Gawande, P. Fornasiero and R. Zbořil, *ACS Catal.*, 2020, **10**, 2231–2259.
- H. B. Wu and X. W. Lou, *Sci. Adv.*, 2017, **3**, eaap9252.
- P.-Q. Liao, J.-Q. Shen and J.-P. Zhang, *Coord. Chem. Rev.*, 2018, **373**, 22–48.
- H. Yan, C. Su and J. He, *J. Mater. Chem. A*, 2018, **6**, 8793–8814.
- S. Mitchell, E. Vorobyeva and J. Pérez-Ramírez, *Angew. Chem. Int. Ed.*, 2018, **57**, 15316–15329.
- X. F. Lu, B. Y. Xia, S.-Q. Zang and X. W. Lou, *Angew. Chem. Int. Ed.*, 2020, **59**, 4634–4650.
- E. M. Miner, L. Wang and M. Dincă, *Chem. Sci.*, 2018, **9**, 6286–6291.
- H. Zhong, K. H. Ly, M. Wang, Y. Krupskaya, X. Han, J. Zhang, J. Zhang, V. Kataev, B. Büchner, I. M. Weidinger, S. Kaskel, P. Liu, M. Chen, R. Dong and X. Feng, *Angew. Chem. Int. Ed.*, 2019, **58**, 10677–10682.
- S. S. Shinde, C. H. Lee, J.-Y. Jung, N. K. Wagh, S.-H. Kim, D.-H. Kim, C. Lin, S. U. Lee and J.-H. Lee, *Energy Environ. Sci.*, 2019, **12**, 727–738.
- M. Aygün, T. W. Chamberlain, M. C. Gimenez-Lopez and A. N. Khlobystov, *Adv. Funct. Mater.*, 2018, **28**, 1802869.
- X.-J. Bai, X.-Y. Lu, R. Ju, H. Chen, L. Shao, X. Zhai, Y.-N. Li, F.-Q. Fan, Y. Fu and W. Qi, *Angew. Chem. Int. Ed.*, 2021, **60**, 701–705.
- T. D. Bennett and A. K. Cheetham, *Acc. Chem. Res.*, 2014, **47**, 5, 1555–1562.
- T. D. Bennett and S. Horike, *Nat. Rev. Mater.*, 2018, **3**, 431–440.
- K. Ping, A. Braschinsky, M. Alam, R. Bhadoria, V. Mikli, A. Mere, J. Aruväli, P. Paiste, S. Vlassov, M. Kook, M. Rähn, V. Sammelselg, K. Tammeveski, N. Kongi and P. Starkov, *ACS Appl. Energy Mater.*, 2020, **3**, 152–157.
- K. Ping, M. Alam, M. Käärik, J. Leis, N. Kongi, I. Järving and P. Starkov, *Synlett*, 2019, **30**, 1536–1540.

- 21 D. Kong, Y. Gao, Z. Xiao, X. Xu, X. Li and L. Zhi, *Adv. Mater.*, 2019, **31**, 201804973.
- 22 S. Li, X. Hao, A. Abudula and G. Guan, *J. Mater. Chem. A*, 2019, **7**, 18674–18707.
- 23 W. Zhang, L. Cui and J. Liu, *J. Alloys Compd.*, 2020, **821**, 153542.
- 24 W. Liu, L. Zhang, X. Liu, X. Liu, X. Yang, S. Miao, W. Wang, A. Wang and T. Zhang, *J. Am. Chem. Soc.*, 2017, **139**, 10790–10798.
- 25 T. Song, Z. Ma, Y. Yuan, J. Xiao, Y. Yang and P. Ren, *ACS Catal.*, 2020, **10**, 4617–4629.
- 26 M. Nakanishi and C. Bolm, *Adv. Synth. Catal.*, 2007, **349**, 861–864.
- 27 Y. Li, S. Jie, K. Li and Z. Liu, *New J. Chem.*, 2018, **42**, 12677–12683.
- 28 P. Zhou, L. Jiang, F. Wang, K. Deng, K. Lv and Z. Zhang, *Sci. Adv.*, 2017, **3**, e1601945.
- 29 S. Yang, L. Peng, D. T. Sun, E. Oveisi, S. Bulut and W. L. Queen, *ChemSusChem*, 2018, **11**, 3131–3138.
- 30 F. Chen, A. Surkus, L. He, M. Pohl, J. Radnik, C. Topf, K. Junge and M. Beller, *J. Am. Chem. Soc.*, 2015, **137**, 11718–11724.
- 31 F. Chen, C. Kreyenschulte, J. Radnik, H. Lund, A. Surkus, K. Junge and M. Beller, *ACS Catal.*, 2017, **7**, 1526–1532.
- 32 R. V. Jagadeesh, K. Murugesan, A. S. Alshammari, H. Neumann, M. M. Pohl, J. Radnik and M. Beller, *Science*, 2017, **358**, 326–332.
- 33 R. Xie, F. Xie, C. J. Zhou, H. F. Jiang and M. Zhang, *J. Catal.*, 2019, **377**, 449–454.
- 34 F. Xie, R. Xie, J. X. Zhang, H. F. Jiang, L. Du and M. Zhang, *ACS Catal.*, 2017, **7**, 4780–4785.
- 35 H. Luo, L. Wang, S. Shang, G. Li, Y. Lv, S. Gao and W. Dai, *Angew. Chem. Int. Ed.*, 2020, **59**, 19268–19274.
- 36 Y. Zhou, Y. Chen, L. Cao, J. Lu and H. Jiang, *Chem. Commun.*, 2015, **151**, 8292–8295.
- 37 W. Zhong, H. Liu, C. Bai, S. Liao and Y. Li, *ACS Catal.*, 2015, **5**, 1850–1856.
- 38 L. Zhang, A. Wang, W. Wang, Y. Huang, X. Liu, S. Miao, J. Liu and T. Zhang, *ACS Catal.*, 2015, **5**, 6563–6572.
- 39 F. Xie, R. Xie, J. X. Zhang, H. F. Jiang, L. Du and M. Zhang, *ACS Catal.*, 2017, **7**, 4780–4785.
- 40 R. Xie, F. Xie, C. J. Zhou, H. F. Jiang and M. Zhang, *J. Catal.*, 2019, **377**, 449–454.
- 41 H. Gilman and R. G. Gorsich, *J. Am. Chem. Soc.*, 1955, **77**, 3134–3135.
- 42 R. A. Aitken, P. K. G. Hodgson, J. J. Morrison and A. O. J. Oyewale, *Chem. Soc. Perkin Trans. 1*, 2002, **3**, 402–415.
- 43 F. O. Ginah, T. A. Donovan Jr., S. D. Suchan, D. R. Pfennig and G. W. Ebert, *J. Org. Chem.*, 1990, **55**, 584–589.
- 44 S.-i. Inaba, H. Matsumoto and R. D. Rieke, *Tetrahedron Lett.*, 1982, **23**, 4215–4216.
- 45 K. Sato, Y. Inoue, T. Mori, A. Sakaue, A. Tarui, M. Omote, I. Kumadaki and A. Ando, *Org. Lett.*, 2014, **16**, 3756–3759.
- 46 V. V. Levin, D. P. Agababyan, M. I. Struchkova and A. D. Dilman, *Synthesis*, 2018, **50**, 2930–2935.
- 47 G. Park, S. Y. Yi, J. Jung, E. J. Cho and Y. You, *Chem. Eur. J.*, 2016, **22**, 17790–17799.
- 48 R. Paul, F. Du, L. Dai, Y. Ding, Z. L. Wang, F. Wei and A. Roy, *Adv. Mater.*, 2019, **31**, 1805598.
- 49 S. Ghosh and R. N. Basu, *Nanoscale* 2018, **10**, 11241–11280.
- 50 J. Lilloja, E. Kibena-Pöldsepp, A. Sarapuu, M. Kodali, Y. Chen, T. Asset, M. Käärrik, M. Merisalu, P. Paiste, J. Aruväli, A. Treshchalov, M. Rähn, J. Leis, V. Sammelselg, S. Holdcroft, P. Atanassov and K. Tammeveski, *ACS Appl. Energy Mater.*, 2020, **3**, 5375–5384.

ToC Entry

We describe a unique amorphous cobalt metal–organic framework derived material that acts both as a recyclable heterogeneous catalyst for organic transformations and as a trifunctional electrocatalyst.



Publication IV

Kongi, N.; Tammeveski, K.; Starkov, P.; **Ping, K.**

Novel Catalyst Materials.

PCT Appl. PCT/EP2019/072050

(51) International Patent Classification:

H01M 4/90 (2006.01) B01J 23/70 (2006.01)
H01M 4/96 (2006.01) B01J 21/18 (2006.01)
B01J 37/08 (2006.01)

(21) International Application Number:

PCT/EP2019/072650

(22) International Filing Date:

16 August 2019 (16.08.2019)

(25) Filing Language:

English

(26) Publication Language:

English

(30) Priority Data:

1813439.5 17 August 2018 (17.08.2018) GB

(71) Applicants: UNIVERSITY OF TARTU [EE/EE];
Ülikooli 18, 50090 Tartu (EE). TALLINN UNIVERSITY OF TECHNOLOGY [EE/EE]; Ehitajate tee 5, 19086 Tallinn (EE).

(72) Inventors: KONGI, Nadežda; c/o University of Tartu, Ülikooli 18, 50090 Tartu (EE). TAMMEVESKI, Kaido; c/o University of Tartu, Ülikooli 18, 50090 Tartu (EE). STARKOV, Pavel; c/o Tallinn University of Technology, Ehitajate tee 5, 19086 Tallinn (EE). PING, Kefeng; c/o Tallinn University of Technology, Ehitajate tee 5, 19086 Tallinn (EE).

(74) Agent: GOODALL, Scott et al.; Sagittarius IP, Marlow International, Parkway, Marlow Buckinghamshire SL7 1YL (GB).

(81) Designated States (unless otherwise indicated, for every kind of national protection available): AE, AG, AL, AM, AO, AT, AU, AZ, BA, BB, BG, BH, BN, BR, BW, BY, BZ, CA, CH, CL, CN, CO, CR, CU, CZ, DE, DJ, DK, DM, DO,

DZ, EC, EE, EG, ES, FI, GB, GD, GE, GH, GM, GT, HN, HR, HU, ID, IL, IN, IR, IS, JO, JP, KE, KG, KH, KN, KP, KR, KW, KZ, LA, LC, LK, LR, LS, LU, LY, MA, MD, ME, MG, MK, MN, MW, MX, MY, MZ, NA, NG, NI, NO, NZ, OM, PA, PE, PG, PH, PL, PT, QA, RO, RS, RU, RW, SA, SC, SD, SE, SG, SK, SL, SM, ST, SV, SY, TH, TJ, TM, TN, TR, TT, TZ, UA, UG, US, UZ, VC, VN, ZA, ZM, ZW.

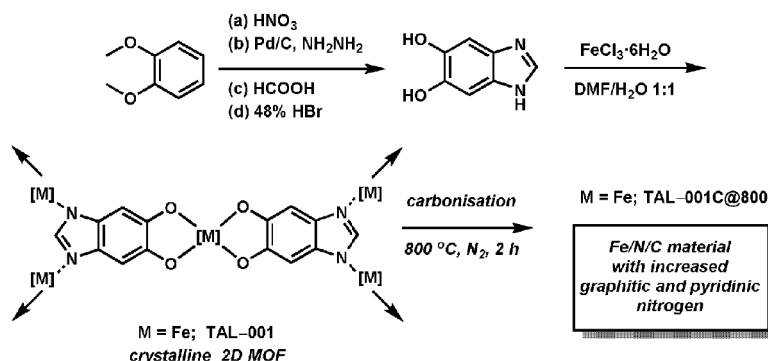
(84) Designated States (unless otherwise indicated, for every kind of regional protection available): ARIPO (BW, GH, GM, KE, LR, LS, MW, MZ, NA, RW, SD, SL, ST, SZ, TZ, UG, ZM, ZW), Eurasian (AM, AZ, BY, KG, KZ, RU, TJ, TM), European (AL, AT, BE, BG, CH, CY, CZ, DE, DK, EE, ES, FI, FR, GB, GR, HR, HU, IE, IS, IT, LT, LU, LV, MC, MK, MT, NL, NO, PL, PT, RO, RS, SE, SI, SK, SM, TR), OAPI (BF, BJ, CF, CG, CI, CM, GA, GN, GQ, GW, KM, ML, MR, NE, SN, TD, TG).

Published:

- with international search report (Art. 21(3))
- before the expiration of the time limit for amending the claims and to be republished in the event of receipt of amendments (Rule 48.2(h))

(54) Title: NOVEL CATALYTIC MATERIALS

Figure 1



(57) Abstract: The present invention relates to novel catalysts, methods of making said catalysts, associated chemical intermediates and uses of said catalysts.

Publication V

Kazimova, N.; **Ping, K.**; Danilson, M.; Merisalu, M.; Aruväli, J.; Käärik, M.; Mikli, V.; Leis, J.; Tammeveski, K.; Starkov, P.; Kongi, N.

Shungite-derived graphene as a carbon support for bifunctional oxygen electrocatalysts.

J. Catal. **2021**, *395*, 178–187.

DOI:10.1016/j.jcat.2021.01.004



Shungite-derived graphene as a carbon support for bifunctional oxygen electrocatalysts

Nargiz Kazimova^a, Kefeng Ping^b, Mahboob Alam^b, Mati Danilson^c, Maido Merisalu^d, Jaan Aruväli^e, Päärn Paiste^e, Maike Käärrik^a, Valdek Mikli^c, Jaan Leis^a, Kaido Tammeveski^a, Pavel Starkov^{b,*}, Nadezda Kongi^{a,*}

^a Institute of Chemistry, University of Tartu, 50411 Tartu, Estonia

^b Department of Chemistry and Biotechnology, Tallinn University of Technology, 12618 Tallinn, Estonia

^c Department of Materials and Environmental Technology, Tallinn University of Technology, 19086 Tallinn, Estonia

^d Institute of Physics, University of Tartu, 50411 Tartu, Estonia

^e Institute of Ecology and Earth Sciences, University of Tartu, 50411 Tartu, Estonia

ARTICLE INFO

Article history:

Received 29 August 2020

Revised 20 December 2020

Accepted 4 January 2021

Available online 12 January 2021

Keywords:

Shungite

Carbon support

Bifunctional electrocatalyst

Nitrogen doping

Renewable energy

ORR

OER

ABSTRACT

Metal–air batteries (MABs) and regenerative fuel cells (RFCs) technologies rely on a combination of efficient electrochemical oxygen evolution and oxygen reduction reactions (OER and ORR, respectively). However, such bifunctional oxygen electrocatalysts also rely on the use of readily accessible carbon supports. Herein, we show that shungite, a natural mineral, can serve as an efficient support for development of bifunctional electrocatalysts. Namely, we purify the mineral to remove additional metals and screen various combinations of cobalt, iron and nitrogen sources to identify electrochemically most suitable system to serve as an active bifunctional oxygen electrocatalyst material.

© 2021 Elsevier Inc. All rights reserved.

1. Introduction

Rechargeable metal–air batteries (MABs), fuel cells (FCs), and electrolyzers are the next-generation clean power devices. These technologies are essential for sustainable energy production, storage and conversion and they rely on the oxygen reduction reaction (ORR) and oxygen evolution reaction (OER) [1–3]. To overcome their sluggish kinetics, platinum-group metal catalysts with high mass loadings are required, but due to the scarcity and the cost, noble-metal-based catalysts are less attractive [4–6]. Carbon-based materials, often co-doped with transition metals and heteroatoms, typically, nitrogen, (the M–N–C catalysts) are the most promising alternatives [7,8]. The design of advanced bifunctional oxygen electrocatalysts requires installment of electrochemically active sites that catalyze several processes. Additionally, by varying physicochemical parameters of the catalyst material in hand, for instance, its morphology, chemical composition, surface area and

conductivity, one can potentially increase the density of or alter the chemical nature of electrocatalytically active sites; hence, the materials' electrocatalytic activity [9–12]. In this domain, various carbon materials are used as the general frameworks that get modified with heteroatoms (nitrogen-, sulfur-, boron- or phosphorus-doping) [13]. The majority of these materials are based on electroconductive carbon. While graphene and reduced graphene oxide are typically used as carbon support, there are many other potential sources of carbon. Recent examples include the use of carbides [14], metal–organic frameworks [10,15], MXenes [16], carbon nanotubes [17], graphitic carbon nitrides (g-C₃N₄) [18] and other naturally derived materials (primarily, from food, wood and cotton) [19–21]. Often, they serve as hosts for a variety of metal species, including metal nanoparticles (reduced metals, metal nitrides, oxides, sulfides and phosphides), bimetallic species and ligated metal complexes (M–N_x sites), referred to as single active species [22]. The combination thereof boosts the overall electrochemical properties of the underlying materials [23,24].

Shungite is a natural carbon-rich and inexpensive mineraloid deposited mainly in the Karelia region (Russia) and its total reserve is estimated to be more than 250 gigatons [25,26]. The graphene-

* Corresponding authors.

E-mail addresses: pavel.starkov@taltech.ee (P. Starkov), nadezda.kongi@ut.ee (N. Kongi), nadezda.kongi@ut.ee (N. Kongi).

like structure of shungite makes it a good alternative to the synthetic graphene. Shungite has a heterogeneous structure, in which carbon exists in irregularly distributed nanosized globules made of curved graphene layers [27,28]. Shungite has high electrical conductivity and a relatively high specific surface area [29–31]. In addition to carbonaceous material, the raw shungite also contains pyrite, quartz, mica, carbonates, zirconium, and other minerals [32,33]. Application wise, Gusmão *et al.* tested the electrocatalytic activity of raw shungite powder toward OER and ORR in 1.0 M KOH solution [28]. Due to different impurities present in their particular sample of shungite, it outperformed other tested carbon materials such as carbon black, carbon nanotubes, C₆₀ fullerene, and glassy carbon. Chou *et al.* recently introduced shungite as a carbon-rich electrode material for the lithium-ion batteries [25].

Herein, we developed a series of shungite-derived carbon materials by doping shungite with nitrogen, cobalt, and iron. Their performance was tested in 0.1 M KOH solution toward oxygen reduction and oxygen evolution reactions, and chronoamperometry was used to assess the stability of the prepared electrocatalysts.

2. Experimental section

2.1. Preparation of shungite-based catalysts

Raw shungite powder (Sh-raw) was etched (acid-treated) with a mixture of concentrated hydrofluoric and nitric acids (HF/HNO₃ 1:1) for 12 h at room temperature, filtered and washed with water and isopropanol to give acid-etched shungite (Sh) [30]. It was doped with nitrogen, cobalt, iron or a combination thereof. Melamine (mel) and dicyandiamide (DCDA) were used as nitrogen sources. For doping, 100 mg of shungite powder, 2 g of nitrogen source and a certain amount of metal precursors (4 mg of Fe (OAc)₂ or 10 mg of CoCl₂·6H₂O) were suspended in isopropanol and 10 mg of polyvinylpyrrolidone (PVP) was added to each suspension as dispersing agent. They were sonicated for 2 h at room temperature and dried overnight at 60 °C. After solvent evaporation, the materials were transferred into ceramic boats and pyrolyzed in a quartz tube furnace at 800 °C for 2 h under N₂ gas flow. Six shungite-based catalysts were prepared and were labeled according to the compounds they were doped with: Sh-DCDA-Co, Sh-DCDA-Fe, Sh-DCDA-CoFe, Sh-mel-Co, Sh-mel-Fe, Sh-mel-CoFe.

2.2. Materials characterization

The morphologies and microstructure were investigated by high-resolution transmission electron microscopy (HR-TEM, JEOL 2200FS FEG at 80 kV) and scanning electron microscopy (HeliosTM NanoLab 600, FEI) equipped with an energy-dispersive X-ray spectroscope (INCA Energy 350, Oxford Instruments). Low-temperature nitrogen adsorption was measured at 77 K by using the NOVA-touch LX2 (Quantachrome Instruments). Specific surface area (S_{BET}) of carbon samples was calculated according to the Brunauer-Emmett-Teller theory in the P/P_0 interval of 0.02–0.2, and the total pore volume (V_{tot}) was calculated at P/P_0 of 0.97. The calculations of pore size distribution (PSD), specific surface area (S_{dRt}) and volume of micropores (V_{m}) were done by using a quenched solid density functional theory (QSDFT) equilibria model for slit type pores. Prior to measurements, all samples were degassed for 12 h at 300 °C. Crystallinity and phase purity of the samples was examined by powder X-ray diffraction (XRD) analysis (SmartLab, Rigaku). Raman spectra were recorded on Horiba's LabRam HR800 spectrometer with a laser line of 532 nm, which was focused on the sample with a spot size of 5 μm . The surface composition of samples was studied using X-ray photoelectron spectroscopy (XPS) in a Kratos Analytical AXIS ULTRA DLD spectrometer equipped with a

monochromatic Al K α X-rays source and an achromatic Mg K α / Al K α dual anode X-ray source. Microwave plasma atomic emission spectroscopy (MP-AES) was used to determine content of cobalt and iron metals in prepared samples. 10 mg of Sh-based sample material was dissolved with Anton Paar Multiwave PRO microwave digestion device in NXF100 vessels (PTFE/TFM liner), where a mixture of 4 mL of HNO₃ and 2 mL of H₂O₂ was used. All samples were digested one by one at temperature of 230 °C and pressures between 45 and 50 bar. Diluted samples were then mixed with 2% HNO₃ solution in order to obtain transition metal concentrations of around 5 mg/L. Agilent4210 MP-AES at analytical wavelengths of Fe 371.993 nm and Co 350.228 nm were used for analysis.

2.3. Electrochemical measurements

The rotating-disk electrode (RDE) method was used to investigate the performance of prepared electrocatalysts toward ORR/OER. Major performance indicators of reaction kinetics were recorded using cyclic voltammetry (CV) by loading electrocatalyst onto the working electrode (Teflon-embedded glassy carbon (GC) disc with a geometric area of 0.126 cm²). The RDE measurements were performed by EDI101 rotating disk electrode system and CTV101 speed control unit (Radiometer) in a typical electrochemical 3-electrode cell connected to an electrochemical workstation Autolab potentiostat/galvanostat PGSTAT30 (Eco Chemie B.V.). The counter electrode was GC rod and all potentials were measured against a reversible hydrogen electrode (RHE) connected to the cell via a Luggin capillary.

Prior to modification, GC disks of the working electrodes were polished to a mirror finish with 1 and 0.3 μm alumina slurries (Buehler) and sonicated in isopropanol and Milli-Q water for 5 min to remove polishing residues. The catalyst ink was prepared by dispersing the mixture of 5 mg of catalyst in 1 mL of 0.05 wt% Nafion solution in isopropanol with the aid of sonication. 4 μL of the catalyst suspension was pipetted onto the GC electrode and the catalyst loading was 153 $\mu\text{g cm}^{-2}$. Comparison experiments were performed with commercial 20 wt% Pt/C (loading 23 $\mu\text{g}_{\text{Pt}} \text{cm}^{-2}$ or $\sim 120 \mu\text{g}_{\text{Pt/C}} \text{cm}^{-2}$) and 99.9% RuO₂ (loading 120 $\mu\text{g cm}^{-2}$).

The main kinetic parameters of ORR, such as onset potential (E_{onset}), half-wave potential ($E_{1/2}$), diffusion-limiting current density (j_d), the number of transferred electrons (n), kinetic-limiting current density (j_k) and Tafel slopes were extracted from the measured polarization curves. The electrocatalytic properties of the prepared materials were evaluated using the Koutecky-Levich (K-L) equation [34]. All the OER polarization curves in this work were iR corrected during experiment by eliminating iR drop with respect to the ohmic resistance of the solution.

The chronoamperometry measurements were conducted by holding the rotating electrodes at a constant potential of 0.75 (for ORR) and 1.6 V vs. RHE (for OER) and lasted for 10,000 s in total. All electrochemical experiments were performed at room temperature (23 ± 1 °C) in 0.1 M KOH. The overall oxygen electrode bifunctional activity was evaluated by the potential difference (ΔE) at an ORR current density of -3 mA cm^{-2} ($E_{1/2}$) and an OER current density of 10 mA cm^{-2} (E_{10}): $\Delta E = E_{10} - E_{1/2}$.

3. Results and discussion

3.1. Acid-etching of shungite

Due to its geological nature, unprocessed shungite powder (Sh-raw) typically contains different phases including amorphous carbon, silica, iron pyrite, and other minerals. Impurities, specifically, transition metals, even if found in trace amounts, can have a strong

effect on the electrocatalytic activity of the carbon material [23,24,35]. Therefore, in order to evaluate the electrocatalytic behavior of the shungite-derived carbon as a support material it was necessary to purify it. Shungite powder was etched with a 1:1 mixture of concentrated HF/HNO_3 so as to remove trace elements.

Surface morphology of the commercial (Sh-raw) and acid-etched (Sh) shungite samples was analyzed by scanning electron microscopy. Both shungite samples compose of microclusters, which contain multilayered structures (Fig. 1a, d). All the samples exhibited hierarchical porous structure with a high amount of interconnected graphene-like sheets. The Sh-raw sample exhibited high inhomogeneity due to the presence of a high amount of different phases.

TEM micrographs of shungite before and after purification (Fig. 1b, e) show that pristine shungite material forms an amorphous structure with the presence of additional phases. As confirmed by TEM-EDX analysis (Fig. 1c) non-processed shungite contained a high amount of amorphous carbon, silica, iron, alumina, and sulfur impurities. After acid-treatment, an ordered stacking of graphitic layers has remained (Fig. 1e) and the majority of the metal impurities was removed (Fig. 1f), yielding graphene-like sheets with higher purity. By XPS, we observed that we also removed aluminum and decreased the silicon content at surface of the material (Table 1). The BET surface area (S_{BET}) of raw shungite powder was $101 \text{ m}^2 \text{ g}^{-1}$ and it slightly decreased upon purification ($94 \text{ m}^2 \text{ g}^{-1}$) (Table 2). Both materials had similar pore diameter distribution with a typical pore size of 3–5 nm (Fig. 1h). Raman spectra demonstrate that $I_{\text{D}}/I_{\text{G}}$ ratio remain in the same region (2.24 for Sh-raw vs 2.37 for Sh), meaning that

the general structure of carbon has not been altered during the acid-etching process (Fig. 1g). In all, we obtained the purified carbon support without changing its structure and morphology.

3.2. Characterization of Sh-based catalysts

With the purified shungite in hand, we prepared and assessed a series of electrocatalysts. We used two different nitrogen sources – melamine (mel) and dicyandiamide (DCDA) – and two different metals (cobalt and iron) [36–40]. In addition to monometallic combinations, we also have prepared the bimetallic catalyst materials. Six shungite-based catalysts were prepared and were labeled according to the compounds they were doped with: Sh-DCDA-Co, Sh-DCDA-Fe, Sh-DCDA-CoFe, Sh-mel-Co, Sh-mel-Fe, Sh-mel-CoFe.

The elemental composition of the catalyst surface was examined by XPS analysis (Table 1 and 2). The metal(s) and nitrogen were effectively incorporated. The carbon content was increased alongside a slight reduction in the oxygen and silicon content. The highest amount of nitrogen was observed in Sh-mel-Co and Sh-mel-CoFe. The amount of cobalt in the bimetallic catalysts was lower than in the only-cobalt samples, while the amount of iron remained at the same level. The relative concentration of pyridinic nitrogen, often associated with highly active materials [3], was comparable in all the catalysts (43–53%).

Since XPS method allows to study the elemental composition of the catalyst surface, the bulk cobalt and iron content was determined by MP-AES. The MP-AES analysis revealed that after acid etching, there is still tiny amount of transition metals remained in shungite powder (0.02 wt% Co and 0.07 wt% Fe). If metallic iron and cobalt and their oxides are expected to be dissolved after acid

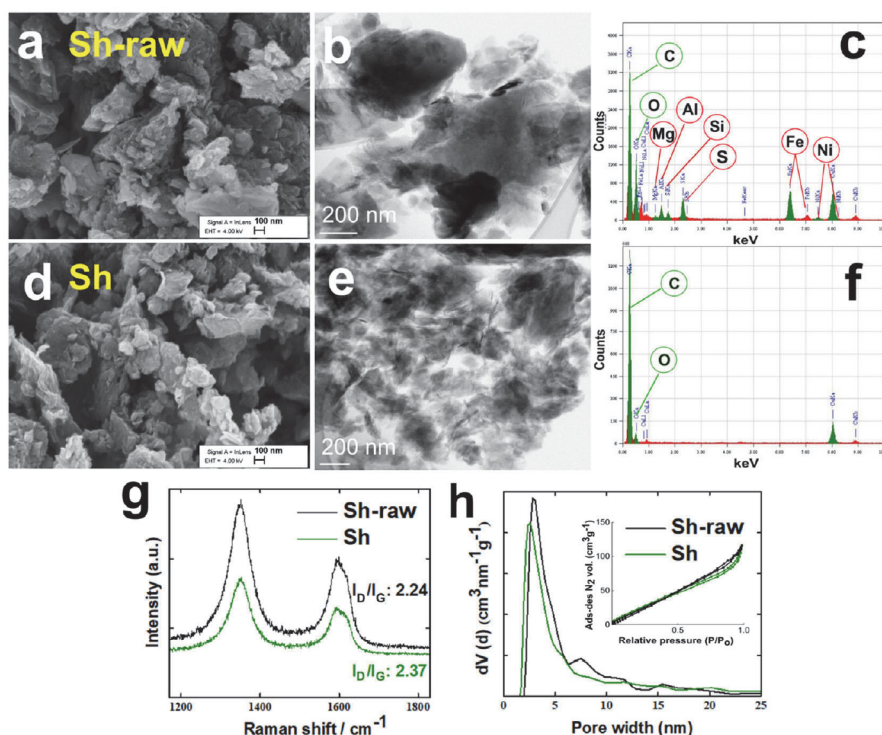


Fig. 1. SEM, TEM micrographs and EDX spectra of as-received Sh-raw (a,b,c) and processed Sh (d,e,f) samples. Raman spectra (g) and pore size distributions (h) of Sh-raw and Sh.

Table 1

Surface elemental composition data of Sh-based catalysts obtained from XPS analysis (at.%) and bulk composition of transition metals determined by MP-AES (wt.%).

Catalyst	Surface elemental composition (at.%)							Bulk metal composition (wt.%)	
	Co	Fe	O	N	C	Si	Al	Fe	Co
Sh-raw	–	–	25.45	–	65.34	7.06	2.16	–	–
Sh	–	–	16.33	–	78.2	5.49	–	–	–
Sh-DCDA-Fe	–	0.35	13.68	2.01	79.45	4.24	–	1.081 ± 0.007	0.026 ± 0.001
Sh-mel-Fe	–	0.41	13.79	2.47	78.21	4.94	–	0.753 ± 0.004	0.025 ± 0.001
Sh-DCDA-Co	2.1	–	9.84	3.85	79.61	4.48	–	0.074 ± 0.002	2.479 ± 0.012
Sh-mel-Co	3.44	–	7.91	7.95	77.63	3.07	–	0.078 ± 0.002	3.299 ± 0.019
Sh-DCDA-CoFe	0.71	0.52	9.99	2.67	81.87	4.11	–	1.085 ± 0.004	2.72 ± 0.012
Sh-mel-CoFe	1.15	0.63	7.75	6.43	81.34	2.65	–	0.921 ± 0.014	3.388 ± 0.01

Table 2

Total nitrogen content and relative concentration of nitrogen species in doped catalyst materials.

Catalyst	N total (at%)	N-oxide (%)	N-graphitic (%)	N-pyrrolic (%)	N-pyridinic (%)
Sh-DCDA-Fe	2.01	12.4	22.9	20.9	43.8
Sh-mel-Fe	2.47	8.91	22.7	21.5	47.0
Sh-DCDA-Co	3.85	4.16	20.3	22.6	53.0
Sh-mel-Co	7.95	3.52	19.4	26.2	50.9
Sh-DCDA-CoFe	2.67	9.74	19.1	26.2	44.9
Sh-mel-CoFe	6.43	6.69	21.7	26.9	44.8

treatment, the remaining part should be in the form of atomically dispersed metal centers within the carbon structure. According to MP-AES results, the iron content was from 0.8 to 1.1 wt% in all Fe-doped samples and bulk Co content was in the range of 2.5–3.4 wt % in all Co-doped catalysts. The average transition metal content at the surface determined by XPS is very close to bulk content obtained by MP-AES.

Throughout the series, the shungite-supported catalyst materials have maintained similar porosity (Table 3), with the pore sizes between three and five nm (Fig. 1h, S5), and the I_D/I_G ratios (in the range of 2.23–2.73, slightly higher for the melamine-derived samples, Fig. S6). The shape of the N_2 adsorption–desorption isotherms corresponds to type III according to IUPAC [44], which indicates non-microporous materials.

After doping of shungite with only iron or cobalt, some unevenly distributed metal particles of iron carbide, and cobalt (0) respectively, were observed by HRTEM (Fig. S7). In contrast, the bimetallic iron/cobalt systems exhibited more homogeneous distribution of nanoparticles with a mean diameter of 29 ± 9 nm (Fig. 2a). HRTEM micrographs of Sh-DCDA-CoFe show typical particles present in the structure of the catalyst (Fig. 2d,e). It is also visible that the catalyst particles are surrounded by several graphitic carbon layers. The EDX elemental mapping of Sh-DCDA-CoFe indicates a homogeneous distribution of carbon and nitrogen, while iron and cobalt colocalize in the nanoparticles (see Fig. 2c). Elemental mapping indicated that iron atoms were also present within nitrogen-doped carbon support as Fe–N_x sites. Cobalt is pre-

sent in the form of metal nanoparticles with diameters ranging from 10 to 50 nm. According to EDX spectrum, the cobalt/iron ratio in these carbon-protected CoFe nanoparticles [41–43] is 80:20 at%. Catalyst materials consisting of multiple elements generally exhibit synergistic effects, with some centers being active toward ORR, while the others are more beneficial for OER; hence, lowering the overall overpotential.

3.3. Electrochemical comparisons of doped shungite materials

All the catalysts were measured in oxygen reduction and evolution reactions to identify the optimal doping strategy. The main kinetic parameters obtained in this study are summarized in Table 4.

The electrochemical behavior of all materials in this work was first examined by cyclic voltammetry (CV) measurements in argon-saturated 0.1 M KOH solution. CV curves were recorded for as-received and purified shungite (Fig. 3a) and compared to the CV curves obtained for doped shungite samples (Fig. 3b). Raw shungite had a surface oxidation peak at about 0.3 V vs RHE, while after the acid-treatment, no obvious redox peaks are observed.

RDE measurements in O₂-saturated electrolyte solution were further used to investigate the ORR kinetics of the prepared shungite-based catalysts. The background current was measured in O₂-free electrolyte at identical scan rate and was subtracted from the RDE data. The ORR polarization curves recorded at a single rotation rate of 1600 rpm are compared in Fig. 3c. Each catalyst

Table 3Specific surface area and pore volumes of shungite-based materials determined from dinitrogen physisorption analysis (S_{BET} is specific surface area calculated from the isotherms by applying Brunauer, Emmett and Teller equation, S_{DFT} is specific surface area calculated by using the density functional theory model, V_{tot} and V_{μ} are total and microporous volume determined using the DFT calculation).

Catalyst	S_{BET} (m ² g ^{−1})	S_{DFT} (m ² g ^{−1})	V_{tot} (cm ³ g ^{−1})	V_{μ} (cm ³ g ^{−1})
Sh-raw	101	70	0.17	0
Sh	94	70	0.15	0
Sh-DCDA-Fe	52	32	0.06	0.01
Sh-mel-Fe	127	84	0.18	0.01
Sh-DCDA-Co	47	25	0.08	0
Sh-mel-Co	69	44	0.11	0.01
Sh-DCDA-CoFe	97	66	0.13	0.02
Sh-mel-CoFe	83	55	0.13	0.01

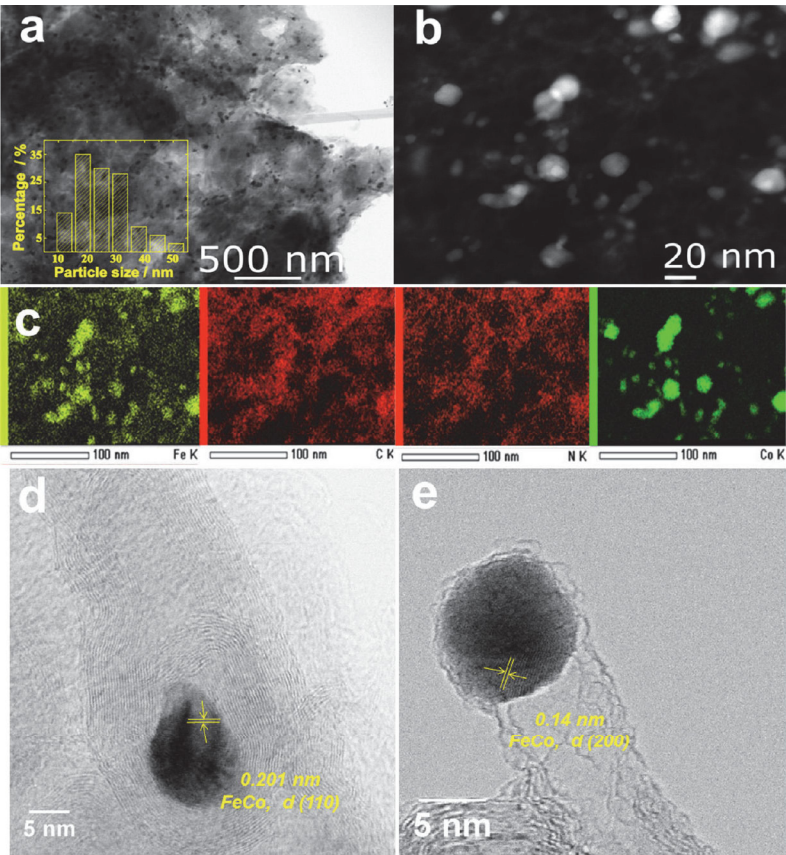


Fig. 2. (a) TEM micrographs of Sh-DCDA-CoFe catalyst material; (b) STEM micrographs and (c) the corresponding element mappings. (d and e) Representative TEM micrographs of the FeCo nanoparticles.

Table 4

Summary of the electrocatalytic performance of shungite-based catalysts (catalyst loading: $153 \mu\text{g cm}^{-2}$; $E_{1/2}$ is the potential at ORR current density of -3 mA cm^{-2} , E_{onset} is the ORR onset potential, n is the number of electrons transferred per O_2 molecule, E_{10} is the potential at OER current density of 10 mA cm^{-2} , η is OER overpotential ($\eta = E_{10} - E_{\text{eq}}$, where E_{eq} is OER thermodynamic potential of 1.23 V vs. RHE), ΔE is the potential gap between $E_{1/2}$ and E_{10}).

Catalyst	$E_{1/2}$ (V)	E_{onset} (V)	n	ECSA ($\text{m}^2 \text{ g}^{-1}$)	E_{10} (V)	η (V)	ΔE (V)
Sh-raw	–	0.77 ± 0.00	3.2 ± 0.1	–	–	–	–
Sh	–	0.78 ± 0.03	2.5 ± 0.1	–	–	–	–
Sh-DCDA-Fe	0.60 ± 0.03	0.87 ± 0.04	4.0 ± 0.0	83	–	–	–
Sh-mel-Fe	0.62 ± 0.02	0.87 ± 0.02	4.2 ± 0.1	69	–	–	–
Sh-DCDA-Co	0.76 ± 0.01	0.87 ± 0.02	3.6 ± 0.2	90	–	–	–
Sh-mel-Co	0.80 ± 0.02	0.93 ± 0.01	4.0 ± 0.0	100	1.69 ± 0.01	0.46	0.89
Sh-DCDA-CoFe	0.78 ± 0.01	0.92 ± 0.01	3.8 ± 0.1	106	1.62 ± 0.00	0.39	0.84
Sh-mel-CoFe	0.80 ± 0.02	0.95 ± 0.01	4.0 ± 0.1	131	1.65 ± 0.01	0.42	0.85
Pt/C	0.86 ± 0.01	1.02 ± 0.02	3.9 ± 0.1	–	–	–	–
RuO_2	–	–	–	–	1.68 ± 0.02	0.45	–

was tested at least three times to warrant good reproducibility. The ORR activity of raw and treated shungite alone is also presented. The obtained diffusion-limiting current density for Sh-mel-CoFe was higher than that obtained for commercial Pt/C (-6.34 vs. -6.17 mA cm^{-2}). The highest onset potential (E_{onset}) of 0.95 V and half-wave potential ($E_{1/2}$) of 0.80 V were also observed for Sh-mel-CoFe, which was very close to the commercial Pt/C (1.00 and 0.85 V vs. RHE, respectively). These results suggest that oxygen is

more easily reduced on the Sh-mel-CoFe catalyst. The detailed RDE characterizations of all the samples are presented in [Supplementary material](#) (Fig. S1, S2, S3, S4). Due to its unique hierarchically porous structure, shungite acts not only as a support but also as a facilitator of ORR promoting the transport of O_2 molecules to the catalytic sites [28].

The average number of electrons transferred per O_2 molecule (n) during the ORR was calculated using the Koutecky–Levich (K–

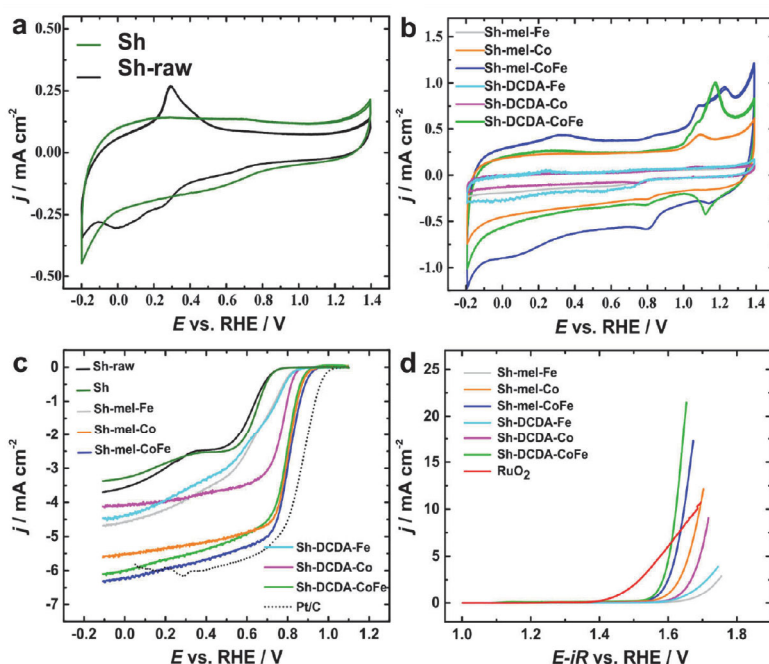


Fig. 3. Cyclic voltammetry curves for (a) undoped shungite and (b) all the doped shungite-based powders modified GC electrodes in Ar-saturated 0.1 M KOH, scan rate 50 mV s^{-1} . (c) Comparison of ORR polarization curves at 1600 rpm, scan rate $v = 10 \text{ mV s}^{-1}$. (d) iR-corrected OER polarization curves in argon-saturated 0.1 M KOH at 10 mV s^{-1} .

L) equation in the potential range between 0.1 and 0.6 V vs. RHE (insets in Fig. S1, S2, S3, S4). Obtained values were close to 4 for almost all the doped shungite materials (Table 4). The lowest n value of 3.6 and 3.8 were found for Sh-DCDA-Co and Sh-DCDA-CoFe, respectively. These values indicate that shungite-supported catalysts are favorable for a 4-electron ORR pathway and the n values are very similar to those obtained for the commercial Pt/C catalyst. The formation of hydrogen peroxide during the 2-electron ORR process is detrimental to the catalyst materials and the 4-electron pathway is desired in fuel cell applications. The linear K-L plots indicated the first-order reaction kinetics toward oxygen.

The electrochemically active surface area (ECSA) of all Sh-based catalysts was determined using a CV method by calculating the double-layer capacitance (C_{dl}) values based on the scan rate dependence of CV curves. Linear slope was observed after plotting the current density difference between anodic and cathodic sweeps at a fixed potential against the scan rate (Figure S9). The fitting slope is twice of the C_{dl} , which is linearly proportional to the ECSA, as follows:

$$ECSA = C_{dl}/C_s$$

where C_s is double layer capacitance of glassy carbon (0.040 mF cm^{-2}). The ECSA values derived from the CV curves are summarized in Table 4.

As can be seen from the trend in Table 2, total N content is higher for samples prepared using melamine. Bimetallic catalysts have similar distribution of nitrogen species, but as can be seen from Table 2 and survey spectra in Figure S11, doping with melamine results in higher total content of nitrogen at the catalyst surface, increasing number of electroactive species at the surface of Sh-mel-CoFe. In addition to the high contents of pyridinic-N in Sh-mel-CoFe catalyst, we found that the surface elemental compo-

sition of Co/Fe is slightly higher than that of Sh-DCDA-CoFe (Table 1), which leads to the higher concentration of Co- N_x /Fe- N_x active sites in comparison with other catalysts. Therefore, higher content of Co- N_x /Fe- N_x active sites ensures the improved ORR electrocatalytic performance. Differences in specific surface areas of the same bimetallic electrocatalytic system might arise from slightly different thermal decomposition behavior of melamine and DCDA in the presence of shungite and transition metals. Apparently, this should lead to different nitrogen doping amount and the M- N_x moieties.

The performance of shungite-based catalysts was also examined toward OER in the Ar-saturated 0.1 M KOH electrolyte. To obtain OER data, the RDE polarization curves were measured from 1.0 to 1.8 V vs. RHE at a scan rate of 10 mV s^{-1} . The electrode was rotated at 1600 rpm in order to avoid the detachment of the catalyst evolved by O_2 adhesion. Apart from the exceptional ORR activity, the bimetallic shungite-based catalysts also exhibited very good OER activity (Fig. 3d). Clearly, the bimetallic Sh-mel-CoFe and Sh-DCDA-CoFe catalysts exhibited much lower overpotential and a higher current density in the specified potential range compared to the commercial RuO_2 benchmark. The overpotential values for Sh-DCDA-CoFe, Sh-mel-CoFe, and commercial RuO_2 at a current density of 10 mA cm^{-2} were 0.39, 0.42, and 0.45 V, respectively (Table 4). The overpotential values obtained for bimetallic catalyst materials are outperforming the state-of-the-art RuO_2 catalyst ($120 \mu\text{g cm}^{-2}$). These results indicate that shungite-based bimetallic systems possess superior OER electrocatalytic activity. Both single-metal Fe-based catalysts showed poor OER response, indicating that Fe alone is not able to work as an active catalytic site for the OER. These results are in agreement with previous studies in the field of iron-based OER electrocatalysts [45]. It is well established that under OER conditions, the surface of the most

Fe-based catalysts is altered by generation of a hydrous iron oxide (HOF) layer which increases the conductivity of electrocatalyst. Compared to cobalt, monometallic iron-based catalysts have significantly lower catalytic activity, however, deliberate co-doping of Fe into Co-based catalysts dramatically enhances the OER electroactivity. Earlier studies by incorporating X-ray absorption near-edge structure (XANES) and extended X-ray absorption fine structure (EXAFS) [46,47] spectroscopy techniques indicate that in these Co-Fe-containing bimetallic catalysts iron is the main active center.

The Tafel slopes derived from the ORR and OER polarization curves at 1600 rpm at a scan rate of 10 mV s^{-1} are shown in Fig. 4a,b. The Tafel plots for OER on Sh-DCDA-CoFe exhibit a slope of 53 mV dec^{-1} , lower than that of the Sh-mel-CoFe (71 mV dec^{-1}), Sh-DCDA-Fe (82 mV dec^{-1}), and RuO_2 (108 mV dec^{-1}) catalysts. Sh-DCDA-CoFe had the lowest Tafel slope value, which makes this material as most active OER electrocatalyst in this study.

The contribution of each metal in multimetallic catalysts to the OER and ORR activity and their synergistic effects are as of yet unclear. Although, it is generally accepted that the OER catalytic activity is largely influenced by the OOH^* adsorption energy [48]. Fe- N_x sites adsorb the OER intermediates too strong resulting in a high activation barrier for the formation of O_2 and thus a comparatively higher overpotential of the OER [49]. The metallic bonding between Fe and Co can redistribute the charge on bimetallic active sites that results in a weaker interaction between the adsorbates and Fe-Co- N_x sites accelerating the OER process [50].

In the XPS survey spectrum of the bimetallic samples, the presence of Co, Fe and O peaks gave solid information that the particles in the catalyst constituted by metal oxide (Figure S11). To study the valence state of Fe and Co, the corresponding Fe2p and Co2p core-level spectra were acquired (Figure S12). The Co2p spectrum (Figure S13a and c) has two main peaks at 779.2 eV and 795.1 eV , both with a satellite at 795.1 eV and 779.2 eV , which correspond to

$\text{Co}2\text{p}_{1/2}$ and $\text{Co}2\text{p}_{3/2}$, respectively, and indicate the presence of the Co^{2+} valence state [51]. In deconvoluted Fe2p spectra (Figure S13b and d), the peaks at 710.2 eV and 724.2 eV indicate the presence of iron valence state of Fe^{3+} [52]. The existence of both CoO and Fe_3O_4 species in the bimetallic samples influences each other. As can be seen from Fig. 3d, iron-based catalyst materials do not have remarkable OER electrocatalytic activity, therefore, Fe-based species present in bimetallic samples serve as a synergist [52]. OER results indicate, that Sh-DCDA-CoFe has a better Fe/Co ratio and thus the best OER performance. The synergistic effect between Fe and Co species induces enhanced OER catalytic activity. On the other hand, XPS shows only surface valence state of metal species. According to HRTEM results, metallic species are present in the form of CoFe alloy. STEM elemental mapping also showed Fe/Co particles or species were colocalized/merged together (experimental proof of the synergy between Fe and Co), which enhances oxygen electroreduction reaction.

The bifunctional oxygen electroactivity of prepared bimetallic Sh-based catalysts could be ascribed to several factors, which were evidenced by spectroscopic and morphological investigations. First, high ORR activity can be attributed to the presence of high amount of pyridinic nitrogen and Fe- N_x sites as confirmed by XPS and HRTEM techniques, respectively. Furthermore, the presence of high amount of defects and disorder in the graphitic sp^2 carbon structure, as confirmed by Raman spectroscopy, has strongly positive effect on ORR electroactivity. Second, enhanced OER electroactivity is mainly attributed to synergistic effect between Co and Fe centers. Additionally, bimetallic Sh-based composites prepared in this work had slightly higher BET surface area values, which also results in higher amount of electrochemically active sites and enhanced overall oxygen electroactivity.

Results obtained in this manuscript show that the use of mixed metals contributes to synergetic effects of iron and cobalt centers that improve the performance of electrocatalysts toward both

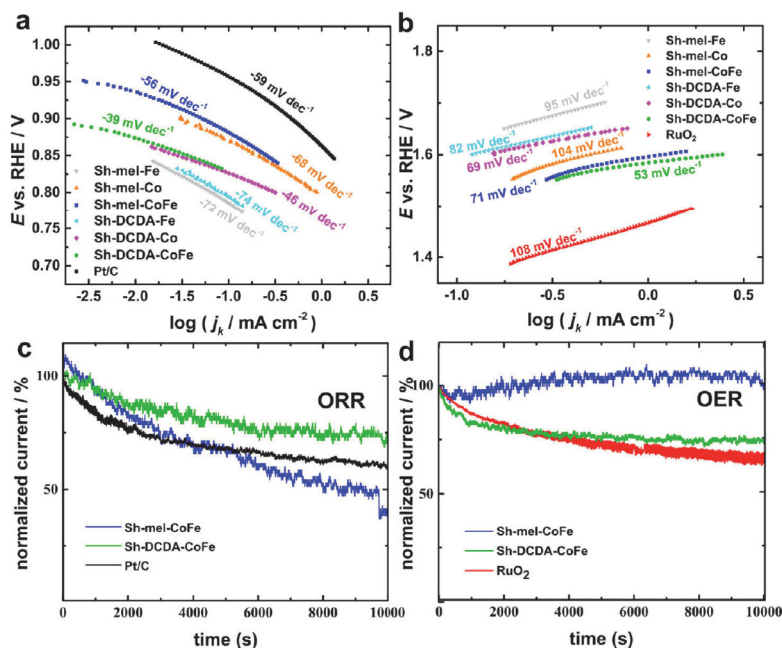


Fig. 4. (a,b) ORR and OER Tafel plots of the catalysts. Current-time chronoamperometry response for (c) ORR at 0.75 V and (d) OER at 1.60 V vs. RHE.

OER and ORR. This synergistic interaction may occur between the Fe and Co phases within metal nanoparticles and exhibit exceptional catalytic activity in comparison to single-metal Sh-based catalysts. Similar synergetic effect between Co and Fe was reported recently by Yuvakkumar and co-workers, where the unique structure of Co and Fe containing catalyst provided a large surface area and ample interlinked channels for O₂ release and mass transport [53]. Moreover, Zhang et al. introduced a CoFeP multi-void nanocages, where both Co and Fe acted as active sites in the catalyst, and the synergy induced between them improved the electronic structure and reduced charge transfer distance [54]. DFT studies revealed that addition of iron to Co-based structure provides a metallic identity with Co(OH)₂, assisting in electron transfer [55]. Zhou et al. reported that Fe-doped Co(OH)₂ nanosheets had substantial grain boundaries, rougher surface, better hydrophilicity, and enhanced electronic properties [56]. Enhanced electrocatalytic activity for ORR of bimetallic iron- and cobalt-based catalysts can be also attributed to the synergistic effect of nitrogen-coordinated metal (M–N_x) centers as active sites [57].

The stability of Sh-DCDA-CoFe and Sh-mel-CoFe as bifunctional catalysts were examined using the chronoamperometric method (Fig. 4c, 4d). The stability measurement for OER and ORR was conducted in Ar-saturated and O₂-saturated 0.1 M KOH solution, respectively. For ORR stability, the electrode was held at 0.75 V vs. RHE, while for OER stability, the potential was held at 1.6 V vs RHE during 10,000 s. As a result, Sh-DCDA-CoFe showed better electrocatalytic stability during both the ORR and OER than commercial Pt/C and RuO₂ catalysts after 10,000 s.

Chronoamperometry curve obtained for Sh-mel-CoFe, has increase in current density during the initial period and later it is slightly depleted, nevertheless negligible drop in current density was observed during 10000 s. In case of Sh-mel-CoFe, a small enhancement in the current density was observed during first 2 h of OER, implying an increase in electrocatalytic activity of the Sh-mel-CoFe material during long-term stability testing. Such behavior has been previously observed for Co-containing catalysts and it can be associated with the formation of cobalt hydroxide, which is considered to be active for the OER [58,59]. A high amount of Co²⁺ in Sh-mel-CoFe facilitates the formation of Co(OH)₂ on the catalyst surface during the OER in alkaline electrolyte, resulting in an increased number of active sites [60]. Morphology of both spent Sh-based bimetallic catalysts was investigated by HRTEM (Figure S10). No obvious structural changes were detected after the durability studies, most likely, due to the presence of protective carbon layers wrapped around metal nanoparticles [61].

4. Conclusions

In this work, low-cost, highly active shungite-based oxygen electrocatalyst materials were developed. The synergistic integration of cobalt and iron along with nitrogen doping gave rise to shungite-based materials with superior bifunctional electrocatalytic performance. Purification of shungite was done with HF/HNO₃ acid mixture. Specifically, Sh-mel-CoFe and Sh-DCDA-CoFe demonstrated highest electrochemical performance as bifunctional catalysts toward OER and ORR.

Declaration of Competing Interest

The authors declare that they have no known competing financial interests or personal relationships that could have appeared to influence the work reported in this paper.

Acknowledgements

This work was supported by the Estonian Research Council grant (PSG250 and PUT1290), institutional research funding (IUT34-14) of the Estonian Ministry of Education and Research, and Tallinn University of Technology (B62). This research was also supported by the EU through the European Regional Development Fund (TK141, “Advanced materials and high-technology devices for energy recuperation systems”). K.P. acknowledges Estonian Smart Specialization PhD Fellowship.

Appendix A. Supplementary material

Supplementary data to this article can be found online at <https://doi.org/10.1016/j.jcat.2021.01.004>.

References

- [1] P.P. Patel, M.K. Datta, O.I. Velikokhatnyi, R. Kuruba, K. Damodaran, P. Jampani, B. Gattu, P.M. Shanthi, S.S. Damle, P.N. Kumta, Noble metal-free bifunctional oxygen evolution and oxygen reduction acidic media electrocatalysts, *Sci. Rep.* 6 (2016) 28367, <https://doi.org/10.1038/srep28367>.
- [2] Z.P. Wu, X.F. Lu, S.Q. Zang, X.W. Lou, Non-noble-metal-based electrocatalysts toward the oxygen evolution reaction, *Adv. Funct. Mater.* 30 (2020) 1910274, <https://doi.org/10.1002/adfm.201910274>.
- [3] R. Ma, G. Lin, Y. Zhou, Q. Liu, T. Zhang, G. Shan, M. Yang, J. Wang, A review of oxygen reduction mechanisms for metal-free carbon-based electrocatalysts, *Npj Comp. Mater.* 5 (1) (2019) 1–15, <https://doi.org/10.1038/s41524-019-0210-3>.
- [4] Z. Chen, D. Higgins, A. Yu, L. Zhang, J. Zhang, A review on non-precious metal electrocatalysts for PEM fuel cells, *Energy Environ. Sci.* 4 (9) (2011) 3167–3192, <https://doi.org/10.1039/C0EE00558D>.
- [5] D. Liu, L. Tao, D. Yan, Y. Zou, S. Wang, Recent advances on non-precious metal porous carbon-based electrocatalysts for oxygen reduction reaction, *ChemElectroChem* 5 (14) (2018) 1775–1785, <https://doi.org/10.1002/celec.201800086>.
- [6] S. Dou, X. Wang, S. Wang, Rational design of transition metal-based materials for highly efficient electrocatalysis, *Small Meth.* 3 (1) (2019) 1800211, <https://doi.org/10.1002/smt.201800211>.
- [7] A. Sarapuu, E. Kibena-Pöldsepp, M. Borghei, K. Tammeveski, Electrocatalysis of oxygen reduction on heteroatom-doped nanocarbons and transition metal–nitrogen–carbon catalysts for alkaline membrane fuel cells, *J. Mater. Chem. A* 6 (3) (2018) 776–804, <https://doi.org/10.1039/C7TA08690C>.
- [8] A. Aijaz, J. Masa, C. Rösler, W. Xia, P. Weide, A.J.R. Botz, R.A. Fischer, W. Schuhmann, M. Muhler, Co@Co₃O₄, encapsulated in carbon nanotube-grafted nitrogen-doped carbon polyhedra as an advanced bifunctional oxygen electrode, *Angew. Chem. Int. Ed.* 55 (12) (2016) 4087–4091, <https://doi.org/10.1002/anie.201509382>.
- [9] E.S.F. Cardoso, G.V. Fortunato, I. Palm, E. Kibena-Pöldsepp, A.S. Greco, J.L.R. Júnior, A. Kikas, M. Merisalu, V. Kisan, V. Sammel, K. Tammeveski, G. Maia, Effects of N and O groups for oxygen reduction reaction on one- and two-dimensional carbonaceous materials, *Electrochim. Acta* 344 (2020), <https://doi.org/10.1016/j.jelelectacta.2020.136052>.
- [10] K. Ping, A. Braschinsky, M. Alam, R. Bhadoria, V. Mikli, A. Mere, J. Aruvaili, P. Paiste, S. Vlassov, M. Kook, M. Rähn, V. Sammel, K. Tammeveski, N. Kongi, P. Starkov, Fused hybrid linkers for metal–organic framework-derived bifunctional oxygen electrocatalysts, *ACS Appl. Energy Mater.* 3 (1) (2019) 152–157, <https://doi.org/10.1021/acsami.9b02039>.
- [11] R. Zhao, Z. Liang, S. Gao, C. Yang, B. Zhu, J. Zhao, C. Qu, R. Zou, Q. Xu, Puffing up energetic metal–organic frameworks to large carbon networks with hierarchical porosity and atomically dispersed metal sites, *Angew. Chem. Int. Ed.* 131 (7) (2019) 1997–2001, <https://doi.org/10.1002/ange.201811126>.
- [12] Y. Pan, K. Sun, S. Liu, X. Cao, K. Wu, W. Cheong, Z. Chen, Y. Wang, Y. Li, Y. Liu, D. Wang, Q. Peng, C. Chen, Y. Li, Core-shell ZIF-8@ ZIF-67-derived CoP nanoparticle-embedded N-doped carbon nanotube hollow polyhedron for efficient overall water splitting, *J. Am. Chem. Soc.* 140 (7) (2018) 2610–2618, <https://doi.org/10.1021/jacs.7b12420>.
- [13] K.N. Wood, R. O’Hayre, S. Pylypenko, Recent progress on nitrogen/carbon structures designed for use in energy and sustainability applications, *Energy Environ. Sci.* 7 (4) (2014) 1212–1249, <https://doi.org/10.1039/C3EE44078H>.
- [14] S. Ratso, I. Kruusenberg, M. Käär, M. Kook, R. Saar, M. Pärs, J. Leis, K. Tammeveski, Highly efficient nitrogen-doped carbide-derived carbon materials for oxygen reduction reaction in alkaline media, *Carbon* 113 (2017) 159–169, <https://doi.org/10.1016/j.carbon.2016.11.037>.
- [15] X.F. Lu, B.Y. Xia, S.Q. Zang, X.W. Lou, Metal-organic frameworks based electrocatalysts for the oxygen reduction reaction, *Angew. Chem. Int. Ed.* 59 (12) (2020) 4634–4650, <https://doi.org/10.1002/anie.201910309>.
- [16] A. Liu, X. Liang, X. Ren, W. Guan, M. Gao, Y. Yang, Q. Yang, L. Gao, Y. Li, T. Ma, Recent progress in MXene-based materials: Potential high-performance

- electrocatalysts, *Adv. Funct. Mater.* (2020) 2003437, <https://doi.org/10.1002/adfm.202003437>.
- [17] S. Shubhadeep, M. Sahoo, V.T. Veetil, K.K. Tadi, A. Ghosh, P. Satyam, R.K. Biroju, P.M. Ajayan, S.K. Nayak, T.N. Narayanan, Covalently connected carbon nanotubes as electrocatalysts for hydrogen evolution reaction through band engineering, *ACS Catal.* 7 (4) (2017) 2676–2684, <https://doi.org/10.1021/acscatal.7b00032>.
 - [18] W. Niu, Y. Yang, Graphitic carbon nitride for electrochemical energy conversion and storage, *ACS Energy Lett.* 3 (11) (2018) 2796–2815, <https://doi.org/10.1021/acseenergylett.8b01594>.
 - [19] J.C. Li, P.-X. Hou, S.Y. Zhao, C. Liu, D.M. Tang, M. Cheng, F. Zhang, H.-M. Cheng, A 3D bi-functional porous N-doped carbon microtube sponge electrocatalyst for oxygen reduction and oxygen evolution reactions, *Energy Environ. Sci.* 9 (10) (2016) 3079–3084, <https://doi.org/10.1039/C6EE02169G>.
 - [20] L. Wang, Z. Sofer, M. Pumaera, Will any crap we put into graphene increase its electrocatalytic effect? *ACS Nano*, (14) (1) 2020, 21–25, <https://doi.org/10.1021/acsnano.9b00184>.
 - [21] I.L. Alonso-Lemus, M.Z. Figueroa-Torres, D. Lardizabal-Gutiérrez, P. Bartolo-Pérez, J.C. Carrillo-Rodríguez, F.J. Rodríguez-Varela, Converting chicken manure into highly active N-P co-doped metal-free biocarbon electrocatalysts: Effect of chemical treatment on their catalytic activity for the ORR, *Sustain. Energy Fuels* 3 (5) (2019) 1307–1316, <https://doi.org/10.1039/C9SE00583D>.
 - [22] C. Wang, Y.V. Kaneti, Y. Bando, J. Lin, C. Liu, J. Li, Y. Yamauchi, Metal-organic framework-derived one-dimensional porous or hollow carbon-based nanofibers for energy storage and conversion, *Mater. Horiz.* 5 (3) (2018) 394–407, <https://doi.org/10.1039/C8MH00133B>.
 - [23] M. Pumaera, Materials electrochemists' never-ending quest for efficient electrocatalysts: The devil is in the impurities, *ACS Catal.*, (10) (13) 2020, 7087–7092, <https://doi.org/10.1021/acscatal.0c02020>.
 - [24] W. Kiciński, S. Dyjak, Transition metal impurities in carbon-based materials: Pitfalls, artifacts and deleterious effects, *Carbon* 168 (2020) 748–845, <https://doi.org/10.1016/j.carbon.2020.06.004>.
 - [25] N.H. Chou, N. Pierce, Y. Lei, N. Perea-López, K. Fujisawa, S. Subramanian, J.A. Robinson, G. Chen, K. Omichi, S.S. Rozhkov, N.N. Rozhkova, M. Terrones, A.R. Harutyunyan, Carbon-rich shungite as a natural resource for efficient Li-ion battery electrodes, *Carbon* 130 (2018) 105–111, <https://doi.org/10.1016/j.carbon.2017.12.109>.
 - [26] I.B. Volkova, M.V. Bogdanova, Petrology and genesis of Karelian shungite—high rank coal, *Int. J. Coal Geol.* 6 (4) (1986) 369–379, [https://doi.org/10.1016/0166-5162\(86\)90011-X](https://doi.org/10.1016/0166-5162(86)90011-X).
 - [27] S.K. Tiwari, V. Kumar, A. Huczko, R. Oraon, A.D. Adhikari, G.C. Nayak, Magical allotropes of carbon: Prospects and applications, *Crit. Rev. Solid State Mater. Sci.* 41 (4) (2016) 257–317, <https://doi.org/10.1080/10408436.2015.1127206>.
 - [28] R. Gusmão, Z. Sofer, D. Bouša, M. Pumaera, Synergistic metals on carbocatalyst shungite, *Chem. Eur. J.* 23 (72) (2017) 18232–18238, <https://doi.org/10.1002/chem.201703974>.
 - [29] P. Buseck, D. Geology and Chemistry A, L.P. Galdobina, Shungites: The C-rich rocks of Karelia, Russia, *Canad. Mineral.*, 35 (6) (1997), pp.1363–1378.
 - [30] E. Tamburri, R. Carcione, S. Politi, M. Angiellari, L. Lazzarini, L.E. Vanzetti, S. Macis, G. Pepponi, M.L. Terranova, Shungite carbon as unexpected natural source of few-layer graphene platelets in a low oxidation state, *Inorg. Chem.* 57 (14) (2018) 8487–8498, <https://doi.org/10.1021/acs.inorgchem.8b01164>.
 - [31] S.V. Krasnovy, A.A. Konchits, B.D. Shanina, M.Y. Valakh, I.B. Yanchuk, V.O. Yuhymchuk, A.V. Yefanov, M.A. Skoryk, Local structure and paramagnetic properties of the nanostructured carbonaceous material shungite, *Nanoscale Res. Lett.* 10 (1) (2015) 78, <https://doi.org/10.1186/s11671-015-0767-9>.
 - [32] S.Y. Chazhengina, V.V. Kovalevskii, Structural characteristics of shungite carbon subjected to contact metamorphism overprinted by greenschist-facies regional metamorphism, *Eur. J. Mineral.* 25 (5) (2013) 835–843, <https://doi.org/10.1127/0935-1221/2013/0025-2327>.
 - [33] V.A. Melezhiuk, M.M. Filippov, A.E. Romashkin, A giant Palaeoproterozoic deposit of shungite in NW Russia: Genesis and practical applications, *Ore Geol. Rev.* 24 (1–2) (2004) 135–154, <https://doi.org/10.1016/j.oregeorev.2003.08.003>.
 - [34] A.J. Bard, L.R. Faulkner, *Electrochemical methods: Fundamentals and applications*, 2nd ed., Wiley, New York, 2001.
 - [35] I. Kruusenberg, N. Alexeyeva, K. Tammeveski, The pH-dependence of oxygen reduction on multi-walled carbon nanotube modified glassy carbon electrodes, *Carbon* 47 (3) (2009) 651–658, <https://doi.org/10.1016/j.carbon.2008.10.032>.
 - [36] S. Ratso, I. Kruusenberg, A. Sarapuu, P. Rauwel, R. Saar, J. Uust, J. Aruväli, P. Kanninen, T. Kallio, K. Tammeveski, Enhanced oxygen reduction reaction activity of iron-containing nitrogen-doped carbon nanotubes for alkaline direct methanol fuel cell application, *J. Power Sources* 332 (2016) 129–138, <https://doi.org/10.1016/j.jpowsour.2016.09.069>.
 - [37] S. Ratso, I. Kruusenberg, A. Sarapuu, M. Kook, P. Rauwel, R. Saar, J. Aruväli, K. Tammeveski, Electrocatalysis of oxygen reduction on iron- and cobalt-containing nitrogen-doped carbon nanotubes in acid media, *Electrochim. Acta* 218 (2016) 303–310, <https://doi.org/10.1016/j.electacta.2016.09.119>.
 - [38] S. Ratso, I. Kruusenberg, M. Käärik, M. Kook, R. Saar, P. Kanninen, T. Kallio, J. Leis, K. Tammeveski, Transition metal-nitrogen co-doped carbide-derived carbon catalysts for oxygen reduction reaction in alkaline direct methanol fuel cell, *Appl. Catal. B Environ.* 219 (2017) 276–286, <https://doi.org/10.1016/j.apcatb.2017.07.036>.
 - [39] S. Ratso, I. Kruusenberg, M. Käärik, M. Kook, L. Puust, R. Saar, J. Leis, K. Tammeveski, Highly efficient transition metal and nitrogen co-doped carbide-derived carbon electrocatalysts for anion exchange membrane fuel cells, *J. Power Sources* 375 (2018) 233–243, <https://doi.org/10.1016/j.jpowsour.2017.08.046>.
 - [40] J. Lilloja, E. Kibena-Pöldsepp, A. Sarapuu, M. Kodali, Y. Chen, T. Asset, M. Käärik, M. Merisalu, P. Paiste, J. Aruväli, A. Treshchalov, M. Rähn, J. Leis, V. Sammelselg, S. Holdcroft, P. Atanassov, K. Tammeveski, Cathode catalysts based on cobalt- and nitrogen-doped nanocarbon composites for anion exchange membrane fuel cells, *ACS Appl. Energy Mater.* 3 (2020) 5375–5384, <https://doi.org/10.1021/acsaem.0c00381>.
 - [41] X. Xiao, X. Li, G. Yu, J. Wang, G. Yan, Z. Wang, H. Guo, FeCo₂ alloy nanoparticles encapsulated in three-dimensionally N-doped porous carbon/multiwalled carbon nanotubes composites as bifunctional electrocatalyst for zinc-air battery, *J. Power Sources* 438 (2019), <https://doi.org/10.1016/j.jpowsour.2019.227019>.
 - [42] S.H. Noh, S. Hyo, M.H. Seo, J. Kang, T. Okajima, B. Han, T. Ohsaka, Towards a comprehensive understanding of FeCo coated with N-doped carbon as a stable bi-functional catalyst in acidic media, *NPG Asia Mater.* 8 (9) (2016), <https://doi.org/10.1038/am.2016.142> e312.
 - [43] J. Liu, T. He, Q. Wang, Z. Zhou, Y. Zhang, H. Wu, Q. Li, J. Zheng, Z. Sun, Y. Lei, J. Ma, Y. Zhang, Confining ultrasmall bimetallic alloys in porous N-carbon for use as scalable and sustainable electrocatalysts for rechargeable Zn-air batteries, *J. Mater. Chem. A* 7 (20) (2019) 12451–12456, <https://doi.org/10.1039/C9TA02264C>.
 - [44] M. Thommes, K. Kaneko, A.V. Neimark, J.P. Olivier, F. Rodríguez-Reinoso, J. Rouquerol, K.W. Sing, Physisorption of gases, with special reference to the evaluation of surface area and pore size distribution (IUPAC Technical Report), *Pure Appl. Chem.* 87 (9–10) (2015) 1051–1069, <https://doi.org/10.1515/pac-2014-1117>.
 - [45] H. Bandal, K.K. Reddy, A. Chaugule, H. Kim, Iron-based heterogeneous catalysts for oxygen evolution reaction; change in perspective from activity promoter to active catalyst, *J. Power Sources* 395 (2018) 106–127, <https://doi.org/10.1016/j.jpowsour.2018.05.047>.
 - [46] L. Gong, X.Y.E. Chng, Y. Du, S. Xi, B.S. Yeo, Enhanced Catalysis of the Electrochemical Oxygen Evolution Reaction by Iron(III) Ions Adsorbed on Amorphous Cobalt Oxide, *ACS Catal.* 8 (2) (2018) 807–814, <https://doi.org/10.1021/acscatal.7b03509>.
 - [47] L. Bai, C.-S. Hsu, D.T.L. Alexander, H.M. Chen, X. Hu, Cobalt-Iron Double-Atom Catalyst for the Oxygen Evolution Reaction, *J. Am. Chem. Soc.* 141 (36) (2019) 14190–14199, <https://doi.org/10.1021/jacs.9b05268>.
 - [48] J.-X. Feng, H. Xu, Y.-T. Dong, S.-H. Ye, Y.-X. Tong, G.-R. Li, FeOOH/Co/FeOOH Hybrid Nanotube Arrays as High-Performance Electrocatalysts for the Oxygen Evolution Reaction, *Angew. Chem. Int. Ed.* 55 (2016) 3694–3698, <https://doi.org/10.1002/anie.201511447>.
 - [49] H. Xu, D. Cheng, D. Cao, A universal principle for a rational design of single-atom electrocatalysts, *Nat. Catal.* 1 (2018) 339–348, <https://doi.org/10.1038/s41929-018-0063-z>.
 - [50] X. Zheng, X. Cao, Z. Sun, K. Zeng, J. Yan, P. Strasser, X. Chen, S. Sun, R. Yang, Indiscrete metal/metal-N-C synergic active sites for efficient and durable oxygen electrocatalysis toward advanced Zn-air batteries, *Appl. Catal. B Environ.* 272 (2020), <https://doi.org/10.1016/j.apcatb.2020.118967> 118967.
 - [51] N.V. Long, Y. Yang, T. Teranishi, C.M. Thi, Y. Cao, M. Nogami, Related magnetic properties of CoFe₂O₄ cobalt ferrite particles synthesised by the polyol method with NaBH₄ and heat treatment: new micro and nanoscale structures, *RSC Adv.* 5 (2015) 56560–56569, <https://doi.org/10.1039/C5RA10015A>.
 - [52] J. Yang, G. Zhu, Y. Liu, J. Xia, Z. Ji, X. Shen, S. Wu, Fe₃O₄-Decorated Co₉S₈ Nanoparticles In Situ Grown on Reduced Graphene Oxide: A New and Efficient Electrocatalyst for Oxygen Evolution Reaction, *Adv. Funct. Mater.* 26 (2016) 4712–4721, <https://doi.org/10.1002/adfm.201600674>.
 - [53] T. Priyadarshini, B. Saravanakumar, G. Ravi, A. Sakunthala, R. Yuvakkumar, Hexamine role on pseudocapacitive behaviour of cobalt oxide (Co₃O₄) nanopowders, *J. Nanosci. Nanotechnol.* 18 (6) (2018) 4093–4099, <https://doi.org/10.1166/jnn.2018.15011>.
 - [54] X. Zhang, Y. Wu, Y. Sun, Q. Liu, L. Tang, J. Guo, CoFeP hollow cube as advanced electrocatalyst for water oxidation, *Inorg. Chem. Front.* 6 (2019) 604–611, <https://doi.org/10.1039/c8qi01227j>.
 - [55] H. Yuan, Y. Wang, C. Yang, Z. Liang, M. Chen, W. Zhang, H. Zheng, R. Cao, Ultrathin Co–Fe layered double hydroxide hollow nanocubes for efficient electrocatalytic water oxidation, *ChemPhysChem* 20 (22) (2019) 2964–2967, <https://doi.org/10.1002/cphc.201900524>.
 - [56] Q. Zhou, Y. Chen, G. Zhao, Y. Lin, Z. Yu, X. Xu, X. Wang, H.K. Liu, W. Sun, S.X. Dou, Active-site-enriched iron-doped nickel/cobalt hydroxide nanosheets for enhanced oxygen evolution reaction, *ACS Catal.* 8 (6) (2018) 5382–5390, <https://doi.org/10.1021/acscatal.8b01332>.
 - [57] K. Kisan, A. Sarapuu, D. Danilani, A. Kikas, V. Kisan, M. Rähn, A. Treshchalov, M. Käärik, M. Merisalu, P. Paiste, J. Aruväli, J. Leis, V. Sammelselg, S. Holdcroft, K. Tammeveski, Transition metal-containing nitrogen-doped nanocarbon catalysts derived from 5-methylfresorcinol for anion exchange membrane fuel cell application, *J. Colloid Interface Sci.* 584 (2021) 263–274, <https://doi.org/10.1016/j.jcis.2020.09.114>.
 - [58] K.R. Park, J.-E. Jeon, G. Ali, Y.-H. Ko, J. Lee, H. Han, S. Mhin, Oxygen Evolution Reaction of Co-Mn-O Electrocatalyst Prepared by Solution Combustion Synthesis, *Catalysts* 9 (2019) 564, <https://doi.org/10.3390/catal9060564>.
 - [59] J.A. Koz, C.M. Hull, Y.-C. Liu, J.A. Switzer, Deposition of p-Co(OH)₂ Films by Electrochemical Reduction of Tris(ethylene diamine)cobalt(III) in Alkaline Solution, *Chem. Mater.* 25 (9) (2013) 1922–1926, <https://doi.org/10.1021/cm400579k>.

- [60] S.V.S. Mers, V. Maruthapandian, V. Ganesh, Highly Efficient Bifunctional Electrocatalyst Using Structurally Architected N-doped Cobalt Oxide, *ChemistrySelect* 3 (2018) 8752–8762, <https://doi.org/10.1002/slct.201802126>.
- [61] Y. She, J. Liu, H. Wang, L. Li, J. Zhou, M.K.H. Leung, Bubble-like Fe-encapsulated N S-codoped carbon nanofibers as efficient bifunctional oxygen electrocatalysts for robust Zn-air batteries, *Nano Res.* 13 (2020) 2175–2182, <https://doi.org/10.1007/s12274-020-2828-3>.

Curriculum vitae

Personal data

Name	Kefeng Ping
Date of birth	March 19, 1993
Place of birth	Hubei, China
Citizenship	Chinese

Contact data

E-mail	kefengping1993@gmail.com
--------	--------------------------

Education

2017–2021	PhD in Chemistry Tallinn University of Technology Dept of Chemistry and Biotech
2015–2017	MSc in Toxicology and Chemistry NUI Galway School of Medicine and Chemistry
2011–2015	BSc in Applied Chemistry Wuhan Institute of Technology

Languages and Skills

English (Intermediate), Chinese (Native); synthetic chemistry (NMR, UV–Vis, FTIR); materials science (PXRD, SEM, TEM, XPS, Raman), chemical biology (cell culture, cell imaging); TopSpin, MestReNova, ImageJ/Fiji, LAS X, AxioVision, ChemDraw, Origin, EndNote, MS Office.

Publications

Ping, K.; Alam, M.; Kahnert, S. R.; Bhadoria, R.; Mere, A.; Mikli, V.; Käärrik, M.; Aruväli, J.; Paiste, P.; Kikas, A.; Kisand, V.; Järving, I.; Leis, J.; Tammeveski, K.; Kongi, N.; Starkov, P. Multi-purpose chemo- and electrocatalyst material from an amorphous cobalt metal–organic framework. *Manuscript submitted*.

Kazimova, N.; **Ping, K.;** Danilson, M.; Merisalu, M.; Aruväli, J.; Käärrik, M.; Mikli, V.; Leis, J.; Tammeveski, K.; Starkov, P.; Kongi, N. Shungite-derived graphene as a carbon support for bifunctional oxygen electrocatalysts. *J. Catal.* **2021**, 395, 178–187.
[DOI:10.1016/j.jcat.2021.01.004](https://doi.org/10.1016/j.jcat.2021.01.004)

Ping, K.; Brashinsky, A.; Alam, M.; Bhadoria, R.; Mihkli, V.; Mere, A.; Vlassov, S.; Kook, M.; Rähn, M.; Sammelselg, V.; Aruväli, J.; Tammeveski, K.; Kongi, N.; Starkov, P. Fused hybrid linkers for metal–organic framework-derived bifunctional oxygen electrocatalysts. *ACS Appl. Energy Mater.* **2020**, 3, 152–157.
[DOI:10.1021/acsaem.9b02039](https://doi.org/10.1021/acsaem.9b02039)

Bhadoria, R.; **Ping, K.**; Lohk, C.; Järving, I.; Starkov, P. A phenotypic approach to probing cellular uptake using heterobivalent constructs. *Chem. Commun.* **2020**, *56*, 4216–4219.
[DOI:10.1039/c9cc09595k](https://doi.org/10.1039/c9cc09595k)

Ping, K.; Alam, M.; Käärik, M.; Leis, J.; Kongi, N.; Järving, I.; Starkov, P. Surveying iron–organic framework TAL–1-derived materials in ligandless heterogeneous oxidative catalytic transformations of alkylarenes. *Synlett* **2019**, *30*, 1536–1540. [invited]
[DOI:10.1055/s-0037-1611877](https://doi.org/10.1055/s-0037-1611877)

Kongi, N.; Tammeveski, K.; Starkov, P.; **Ping, K.** Novel catalytic materials. PCT Appl. PCT/EP2019/072050

Zhong, P.; **Ping, K.**; Qiu, X.; Chen, F. Sorption of humic acid to layered double hydroxides prepared through ion thermal method. *Desalin. Water Treat.* **2017**, *93*, 109–119.
[DOI:10.5004/dwt.2017.21474](https://doi.org/10.5004/dwt.2017.21474)

Elulookirjeldus

Isikuandmed

Nimi	Kefeng Ping
Sünniaeg	March 19, 1993
Sünnikoht	Hubei, Hiina
Kodakondsus	Hiina

Kontaktandmed

E-mail	kefengping1993@gmail.com
--------	--------------------------

Hariduskäik

2017–2021	PhD (keemia) Tallinna Tehnikaülikool Keemia ja biotehnoloogia instituut
2015–2017	MSc (toksikoloogia ja keemia) NUI Galway School of Medicine and Chemistry
2011–2015	BSc (rakenduskeemia) Wuhan Institute of Technology

Keelte- ja muud oskused

Inglise (C1), hiina (emakeel); sünteetiline keemia (TMR, UV–Vis, FTIR); materjalitehnoloogia (PXRD, SEM, TEM, XPS, Raman); keemiline bioloogia (rakukultuur, mikroskoopia); TopSpin, MestReNova, ImageJ/Fiji, LAS X, AxioVision, ChemDraw, Origin, EndNote, MS Office.

Publikatsioonid

Ping, K.; Alam, M.; Kahnert, S. R.; Bhadoria, R.; Mere, A.; Mikli, V.; Käärrik, M.; Aruväli, J.; Paiste, P.; Kikas, A.; Kisand, V.; Järving, I.; Leis, J.; Tammeveski, K.; Kongi, N.; Starkov, P. Multi-purpose chemo- and electrocatalyst material from an amorphous cobalt metal–organic framework. *Manuscript submitted*.

Kazimova, N.; **Ping, K.**; Danilson, M.; Merisalu, M.; Aruväli, J.; Käärrik, M.; Mikli, V.; Leis, J.; Tammeveski, K.; Starkov, P.; Kongi, N. Shungite-derived graphene as a carbon support for bifunctional oxygen electrocatalysts. *J. Catal.* **2021**, 395, 178–187.

[DOI:10.1016/j.jcat.2021.01.004](https://doi.org/10.1016/j.jcat.2021.01.004)

Ping, K.; Brashinsky, A.; Alam, M.; Bhadoria, R.; Mihkli, V.; Mere, A.; Vlassov, S.; Kook, M.; Rähn, M.; Sammelselg, V.; Aruväli, J.; Tammeveski, K.; Kongi, N.; Starkov, P. Fused hybrid linkers for metal–organic framework-derived bifunctional oxygen electrocatalysts. *ACS Appl. Energy Mater.* **2020**, 3, 152–157.

[DOI:10.1021/acsaem.9b02039](https://doi.org/10.1021/acsaem.9b02039)

Bhadoria, R.; **Ping, K.**; Lohk, C.; Järving, I.; Starkov, P. A phenotypic approach to probing cellular uptake using heterobivalent constructs. *Chem. Commun.* **2020**, *56*, 4216–4219.
[DOI:10.1039/c9cc09595k](https://doi.org/10.1039/c9cc09595k)

Ping, K.; Alam, M.; Käärik, M.; Leis, J.; Kongi, N.; Järving, I.; Starkov, P. Surveying iron–organic framework TAL-1-derived materials in ligandless heterogeneous oxidative catalytic transformations of alkylarenes. *Synlett* **2019**, *30*, 1536–1540. [invited]
[DOI:10.1055/s-0037-1611877](https://doi.org/10.1055/s-0037-1611877)

Kongi, N.; Tammeveski, K.; Starkov, P.; **Ping, K.** Novel catalytic materials. PCT Appl. PCT/EP2019/072050

Zhong, P.; **Ping, K.**; Qiu, X.; Chen, F. Sorption of humic acid to layered double hydroxides prepared through ion thermal method. *Desalin. Water Treat.* **2017**, *93*, 109–119.
[DOI:10.5004/dwt.2017.21474](https://doi.org/10.5004/dwt.2017.21474)

ISSN 2585-6901 (PDF)
ISBN 978-9949-83-685-7 (PDF)